Georg-August University Göttingen
German Aerospace Center

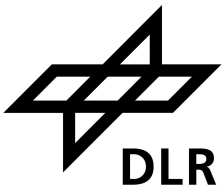

Master Thesis:

Linear Instability Analyses of Supersonic and Hypersonic Flows over Rotating Cones

prepared by

Jonas Penning

at the

Institute of Aerodynamics and Flow Technology

in the

Department of High Speed Configurations

First Referee:	Prof. Dr. Andreas Dillmann
Second Referee:	Apl. Prof. Dr. Martin Rein
First Supervisor:	Dr. Alexander Theiß
Second Supervisor:	Dr. Stefan Hein

Submission: January 24, 2024

Abstract

Rotating objects in super- and hypersonic flow fields are part of many real-world applications, for example, the entry of space debris or the reentry of launch-vehicle stages in the atmosphere. Investigating the physics and especially the transition process in boundary layers of such objects could help to understand and control their motion, as turbulent behaviour is disadvantageous due to the drag increase.
Therefore, in this work, the rotating cone is used as a generic configuration to examine the influence of rotation on the instabilities in the laminar boundary layer. The results of local (parallel) linear stability analysis are presented and a parameter study is performed in order to answer the following questions: How does the rotation intensity affect the boundary-layer instabilities and what influence have the half-opening angle and the oncoming flow velocity on the instabilities? Moreover, the influence of rotation terms in the stability equations are investigated as well as the influence of the metric terms to better understand the influence of the considered geometry on the boundary layer, as the flat plate and the cone in super- and hypersonic flow fields form similar instabilities.
The basic flow is calculated using the flow-field solver TAU. A grid convergence analysis is performed, in order to ensure sufficient resolution of the used grids. Also, it is ensured that the simulations converge in time.
The stability analysis focuses on a specific position on the cone. Four different instability types are investigated, namely the 1^{st}-Mode, the 2^{nd}-Mode, the Crossflow-Instability and the Centrifugal-Instability. The NOLOT extension for rotational coordinate systems presented in the work of Dechamps & Hein [8] is used as the solver for the stability equation and is corrected, as scale factors have falsely been included in the Coriolis and centrifugal terms of the extension (which does not invalidate the results presented in the work of Dechamps & Hein [8]).
The results of the investigation of the non-rotational setup is in accordance with previous works. Rotation has a general destabilising effect on the 1^{st}- and 2^{nd}-Mode. Further, the 1^{st}-Mode destabilises for waves travelling with and stabilises for waves travelling against the direction of the cone's rotation, whereas it is the other way around for the 2^{nd}-Mode. Rotation causes a cross-flow velocity component in the basic flow, which leads to the destabilisation of the Crossflow-Instability. With inclusion of rotation terms in the stability equation, the Centrifugal-Instability destabilises. With the inclusion of both the metric and rotation terms, two additional modes have been found to destabilise and are interpreted as Crossflow-Modes, while the question is discussed, whether they represent physically valid instabilities or not. The increase of the rotation intensity destabilises each considered mode further. With the increase of the oncoming flow velocity each mode also destabilises except for the 1^{st}-Mode, that stabilises instead. The increase of the half-opening angle leads to waves with higher circumferential wavenumbers to be unstable. The increase of the half-opening angle also has a destabilising effect on each mode but the Centrifugal-Instability and one of the newly found modes. Rotation terms destabilise and metric terms stabilise every considered mode.

Contents

List of Figures

List of Tables

Nomenclature

Sub- and Superscripts

Sub-/Supers.	Definition
*	Dimensional quantity (without *: non-dimensional)
$_e$	Boundary-layer edge quantity
$_{\text{ref}}$	Reference quantity
$_\infty$	Free-stream quantity

Cone (Geometry)

Dim. Variable	Definition	Unit
$\mathbf{X}^* = (X^*, Y^*, Z^*)$	Cartesian coordinate system	$(\text{m}, \text{m}, \text{m})$
$\mathbf{x}^* = (x^*, \theta, z^*)$	Cone's curvilinear coordinate system (streamwise, circumferential, wall-normal)	$(\text{m}, -, \text{m})$
L^*	Height of the cone	m
l^*	Lateral length of the cone	m
r_n	Radius of the cone's nose	m
ψ	Half-opening angle of the cone	$^\circ$
$\vec{\Omega}^*$	Rotation velocity	Hz
h_θ^*	Circumferential scale factor	m

Grid Development Process

Dim. Variable	Definition	Unit
ϵ_r	Rotation angle	$^\circ$

Dim. Variable	Definition	Unit
N_p	Number of base panels in θ-dir.	-
N_l	Number of points in near-wall layer in z-dir.	-
N_s	Number of points on cone surface in x-dir.	-
$\bar{\Omega}$	Rotation rate	-

Basic Flow

Dim. Variable	Definition	Unit
$\mathbf{U}^* = (U^*, V^*, W^*)$	Velocity vector in Cartesian coord. system	m/s
$\mathbf{u}^* = (u^*, v^*, w^*)$	Velocity vector in cone's coord. system	m/s
Re	Reynolds number	-
Re_l	Local Reynolds number	-
$\mathrm{Re}_{\mathrm{blasius}}$	Blasius Reynolds number	-
M	Mach number	-
Pr	Prandtl number	-
δ^*	in chapter 3: Wall-normal scale in chapter 5: Blasius length	m
p^*	Pressure	Pa
ρ^*	Density	$\mathrm{kg/m^3}$
T^*	Temperature	K
μ,ν	dynamic,kinematic viscosity	$\mathrm{sPa,m^2/s}$

Linear Stability Theory

Dim. Variable	Definition	Unit
α^*	Streamwise wavenumber	$\mathrm{m^{-1}}$
α_r^*	Real part of streamwise wavenumber	$\mathrm{m^{-1}}$
β^*	Circumferential wavenumber	$\mathrm{m^{-1}}$
σ^*	Disturbance amplification/growth rate	$\mathrm{m^{-1}}$
$n = \beta^*/h_\theta^*$	Wavefront count	-
$\omega^* = 2\pi f^*$	Angular Frequency	Hz
m_{ij}^*	diverg. and curvature along wave rays/fronts	$1/\mathrm{m^2}$

1. Introduction

1.1. Motivation

This work considers the rotating cone as generic configuration to study the effects of rotation on the boundary-layer instabilities that could lead to laminar-turbulent transition in the object's boundary layer.

The boundary layer defines the region near solid surfaces in flow fields, in which viscous effects must be taken into account and the velocity increases from zero at the wall (due to the no-slip condition [7]) up to the free-stream value [35, chap. 2]. Continuous fluid flows are generally divided into laminar or turbulent behaviour [35, chap. 1.4]. If a fluid flows laminar, the fluid particles move in an orderly fashion. Contrary, fluid particles in turbulent flows behave unordered and have momentum perpendicular to the net flow. As boundary layers can depict both types of fluid behaviour, laminar flow in boundary layers is reported to produce less friction drag than turbulent flow. This is important for many real-world applications because for example a vehicle with less friction drag is more efficient and therefore needs less energy for its motion.
In the boundary layer of objects in external flow fields, transition can occur between laminar and turbulent flow [35, chap. 15]. Figure 1.1 is a sketch, published in the work of Schlichting & Gersten [35], that visualises the laminar-turbulent transition for the flat plate with oncoming flow of speed u_∞: In the left part of Figure 1.1, the boundary layer depicts laminar flow. However, at a specific position indicated by the indifference Reynolds number Re_{ind}, the region of transition starts, as three-dimensional disturbances in the mean flow begin to grow along the flat plate. These disturbances are also referred to as instabilities, which either stabilise or destabilise with influential parameters such as the position on the plate. In Figure 1.1, the disturbances destabilise further downstream and lead to completely turbulent flow at the critical Reynolds number Re_{crit}.

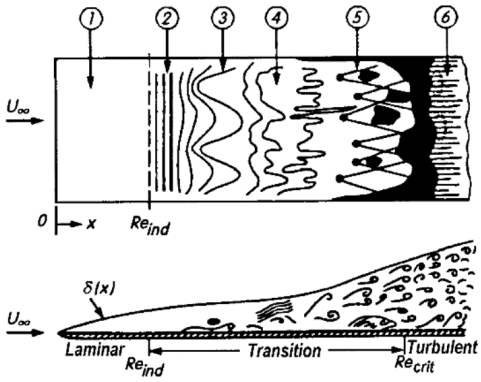

Fig. 15.5. Sketch of laminar–turbulent transition in the boundary layer on a flat plate at zero incidence, after F.M. White (1974)
(*1*) stable laminar flow
(*2*) unstable Tollmien–Schlichting waves
(*3*) three–dimensional waves and vortex formation (Λ-structures)
(*4*) vortex decay
(*5*) formation of turbulent spots
(*6*) fully turbulent flow

Figure 1.1.: Sketch of the laminar-turbulent transition in the boundary layer of a flat plate with oncoming flow u_∞ (taken from [35, Fig. 15.5]): Disturbances start to destabilise the laminar flow, which leads to turbulence further downstream.

The situation in the boundary layer of the (rotating) cone is similar to the flat plate in Figure 1.1. However, among other things, the rotation and the speed of the oncoming flow lead to different types of instabilities (cf. section 1.2).
Supersonic and hypersonic free-stream speeds are considered, which represents the conditions for aircraft flights such as jet planes or spacecraft capsules (cf. Ref. [43]). As mentioned, the cone provides a generic geometry, to study the influence of rotation on the instabilities in the boundary layer. This is also important for real-world applications, as rotation of objects in hypersonic flows is present in the re/entry of launch-vehicle stages or space debris in the atmosphere (cf. Ref. [37]).
To gain a more detailed insight into the transition mechanism of the rotating cone, local linear stability analysis is performed in this work to study the influence of different parameters on the instabilities in the boundary layer. For example, the cone's rotational velocity is varied to obtain a broader spectrum of rotational setups. The half-opening angles is also varied, as the cone's width could stabilise or destabilise the disturbances.
The basic flow is considered in the rotational frame of reference of the cone, which leads to additional rotation terms in the stability equations (cf. chapter 2). The influence of these rotation terms is also analysed, to obtain information about the growth mechanism of the instabilities.

This study starts with a presentation of the instabilities in the boundary layer of a (rotating) cone in super- and hypersonic axial oncoming flow in the next sec-

tion. The fundamental equations and an introduction to linear stability theory is given in chapter 2. As the stability equation solver, an extension of the NOLOT-code is used, originally presented in the work of Hein et al. [19] and adapted for rotational coordinate system in the work of Dechamps & Hein [8]. This NOLOT-extension is validated in chapter 3 by analysing the boundary layer of the rotating cone in still, isothermal, incompressible fluid approximated with the self-similarity approach. Chapters 4 and 5 focus on the rotating cone in super- and hypersonic axial flow. Chapter 4 describes the grid development process and the simulation of the flow field and presents basic-flow boundary layer. Chapter 5 presents the linear stability analysis results and studies the influence of the parameters rotation intensity, free-stream Mach number, half-opening angle and metric & rotation terms on the instabilities in the cone's boundary layer. Finally, chapter 6 gives a summary of the results and provides an outlook for future studies.

1.2. Current Status of Research

In this work, linear stability analysis is performed for the flow field in super- and hypersonic three-dimensional laminar boundary layers, which has been of general interest prior to this work. However, the influence of the cone's rotation and the corresponding cross-flow in compressible high speed setups has received little attention from the scientific community. This section reviews the research and knowledge on the topic to this date and introduces the boundary-layer instabilities considered in this work.

As described in section 1.1, boundary-layer instabilities are caused by disturbances in the mean flow and can be described mathematically using a wave ansatz with characteristic parameters: The wavenumbers α and β describe the spatial development, whereas the temporal behaviour of these disturbances is described by the wave's frequency. The combination of the wavenumbers and the frequency is referred to as the parameter space throughout this work. The mathematical description is discussed in more detail in section 2.3, but a brief introduction is provided here, to adequately present the findings of previous studies.

If a three-dimensional boundary layer is considered to be supersonic and therefore compressible, the underlying equation - in the work of Mack [29] referred to as the "3D compressible counterpart of the Rayleigh equation" - gives rise to an infinite

number of valid solutions satisfying the boundary conditions [29]. These solutions are intuitively named according to their order (i.e. 1st-Mode, 2nd-Mode,...) and extensive experimental and numerical studies have been performed not only for the flat plate but also for the non-rotating cone to analyse these instabilities.

As reported in Ref. [29], the Mach-number of the external flow was found to be an important parameter to determine which of the infinite solutions of modes presented above are unstable or not. For a flat plate, there exist mode-specific neutral Mach-numbers at which the respective modes become unstable [29]. For example, as the Mach-Number increases, the 1st-Mode stabilises while the 2nd-Mode destabilises and eventually becomes the dominant instability. For the non-rotating cone, this has been reproduced experimentally, for example in the work of Kimmel & Stetson [40] or Kendall [26], as well as numerically in numerous works. The linear stability analyses performed in the literature mostly focus on the 1st- and 2nd-Mode, which will also be of interest in this work. For instance, Gasperas [16], Mack [30] and Reed & Balakumar [2] analysed cones with different half-opening angles in hypersonic flows, each showing that both mentioned modes are unstable, with the 2nd-Mode being the dominant instability as expected. In the work of Chen [5], the 3rd-Mode was also analysed using a Mach number of $M_\infty = 15$ for the external flow.

It has been found that the modes occupy different domains in the parameter space, although they sometimes overlap. For example, the frequency of each mode's most unstable parameter set increases with the order of the mode, however, in the works of Mack [30] or Gasperas [16], the 1st-Mode continuously transits into the 2nd-Mode with the frequency increase. Spatially, the modes behave symmetrically in the circumferential direction of the non-rotating cone. However, in every above mentioned study the most unstable form of the 2nd-Mode is two-dimensional ($\beta = 0$).

The rotating cone has been briefly investigated by Reed & Balakumar [2]. The resulting cross-flow component of the mean flow was reported to cause an increase in the amplification rates and a shift of the most unstable waves towards the cross-flow direction. These findings were recently confirmed in the work of Song & Dong [39]. As both works focused only on the 1st-Mode in supersonic flow setups, the influence of rotation on the 2nd-Mode of a rotating cone's hypersonic laminar boundary layer has not been investigated to the author's knowledge. However, Liu [28] investigated the effect of the cross-flow velocity component on the 2nd-Mode of a flat-plate's boundary layer, as the mode is reported to behave similarly to the 1st-Mode, shifting towards positive wavenumbers in cross-flow direction in the parameter space.

Further, both Reed & Balakumar [2] and Song & Dong [39] have reported the existence of a Crossflow-Instability: In Ref. [2] it is only vaguely indicated, that this instability occupies a vast frequency domain including the stationary waves, however Song & Dong [39] were able to generally describe the Crossflow-Instability behaviour in the parameter space of the supersonic boundary layer.
The Crossflow-Instability was first introduced in the work of Gregory et al. [17] and generally arises due to pressure gradients on curved swept surfaces (cf. Reed et al. [34]) and due to cross-flow velocity components perpendicular to the streamline (cf. Liu [28] and Reed & Balakumar [2]), which both cause an inflection point in the cross-flow velocity component.
By studying the compressible Falkner-Skan-Cooke equations for the flat plate with the onset of cross-flow velocity due to different sweep angles and pressure gradients, Liu [28] reported similar results to the work of Song & Dong [39] for the cone. In both studies, the Crossflow-Instability is characterised as an extension of the 1^{st}-Mode in the cross-flow direction. In Ref. [28], there is a detailed discussion whether this extension should be denoted as a Crossflow-Mode or not. This question will also be revisited in this work.
Experimentally, the instability has been found to form co-rotating spiral vortices [34, 42].
Otherwise, the Crossflow-Instability in the boundary layer on rotating cones in supersonic oncoming flow has not been studied much. The research has mostly focused on subsonic setups, for which self-similarity approaches have been derived to approximate the basic flow in the boundary layers [12, 14, 15, 21, 36]. The studies show that, as for the supersonic cones, the Crossflow-Instability is unstable for circumferential wavenumbers in the direction of rotation and extends towards negative frequencies. This will be considered briefly, as the rotating cone in still fluid is of interest in chapter 3, to validate the stability equation solver used throughout this work.

With the rotation of the cone, the so-called Centrifugal-Instability has also been found to destabilise and to form counter-rotating spiral vortices in the cone's boundary layer [42]. Experimentally in the work of Kato et al. [25] as well as numerically using the self-similarity approach in the works of Hussain et al. [22, 23], the Centrifugal-Instability is reported to be the dominant transition mechanism in boundary layers of rotating cones without inflow and with an half-opening angle smaller than 40°. For half-opening angles greater than 40°, the Crossflow-Instability

dominates the transition mechanism. This is also confirmed for boundary layers of supersonic cones: Song & Dong [39] have reported that, for specific rotation rates, the Centrifugal-Instability occupies similar wavenumber and frequency domains as the Crossflow-Instability, but with much higher amplification rates.

This work considers supersonic (at $M_\infty = 3.214$) and hypersonic flows (at $M_\infty = 6.1$) around a rotating cone and analyses the instability characteristics of the 1^{st}- and 2^{nd}-Mode as well as the Crossflow- and Centrifugal-Instability. For each mode, the question is answered how rotation affects the instability. Special interest lies on the 2^{nd}-Mode, as the influence of rotation has not been studied much to the author's knowledge. It is also asked how metric and rotation terms affect the modes individually. Song & Dong [39] briefly examined this topic, but both metric and rotation terms were either included or excluded together. Further, the half-opening angle is varied to understand the influence of the cone's width. The results of this detailed parameter study are presented in chapter 5.

2. Introduction of Fundamental Concepts

In this study, linear stability analysis is performed for laminar boundary layers on rotating cones in super- and hypersonic inflow. Therefore, a general notation and an introduction of the underlying physical quantities is given first. Further, this chapter presents the Navier-Stokes Equation to describe the flow field in curvilinear coordinate systems. With the decomposition into the steady basic flow and unsteady disturbances, the stability equations are introduced, which describe the perturbation's spatial and temporal behaviour.

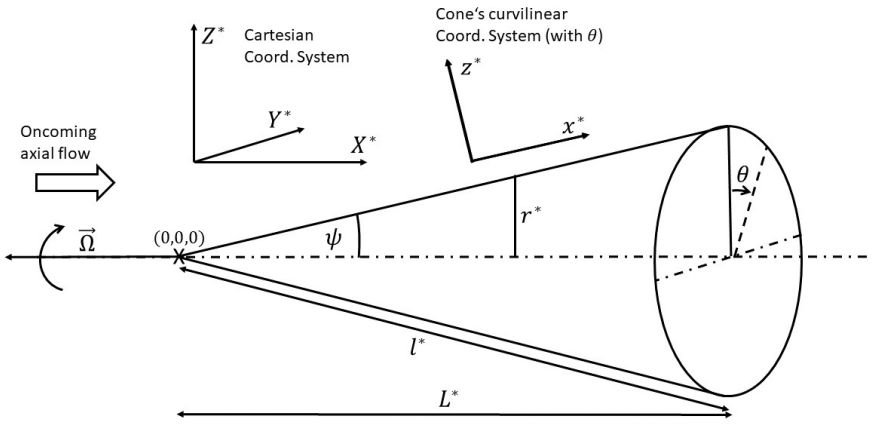

Figure 2.1.: Geometry of the cone (inspired by [20, Fig. 1]): The curvilinear coordinate system $\{x^*, \theta, z^*\}$ of the cone with half-angle ψ. The cone rotates according to the rotation vector $\mathbf{\Omega}^*$.

2.1. Geometry of the Cone

First, to introduce this work's notation, the subscripts $_{\mathrm{ref}}$, $_{e}$ and $_{\infty}$ generally denote reference, boundary-layer edge and free-stream values respectively, whereas the superscript * refers to a dimensional quantity. This notation allows, that the dimensional and non-dimensional version both refer to the same quantity: For example, $\mathbf{\Omega}^{*}$ and $\mathbf{\Omega}$ both represent the cone's rotational velocity (see below), only that $\mathbf{\Omega}$ is non-dimensionalised with a specific reference value.

The cone's geometry is visualised in Figure 2.1: Capital letters refer to the Cartesian coordinate system $\{X^{*}, Y^{*}, Z^{*}\}$, whereas lowercase letters describe quantities given in the cone's curvilinear coordinate system $\{x^{*}, \theta, z^{*}\}$. In the cone's coordinate system, θ stands for the circumferential direction, while z^{*} is the wall-normal coordinate and x^{*} defines the coordinate along the contour on the cone's surface with θ set constant (streamwise direction for non-rotating cone). The transformation between both coordinate systems is given by [20]

$$\begin{aligned} X^{*} &= x^{*}\cos(\psi) - z^{*}\sin(\psi)\ , \\ Y^{*} &= (x^{*}\sin(\psi) + z^{*}\cos(\psi))\cdot\sin(\theta) = h_{\theta}^{*}\cdot\sin(\theta)\ , \\ Z^{*} &= (x^{*}\sin(\psi) + z^{*}\cos(\psi))\cdot\cos(\theta) = h_{\theta}^{*}\cdot\cos(\theta)\ , \end{aligned} \tag{2.1}$$

in which ψ refers to the half-opening angle of the cone. The quantity h_{θ}^{*} describes the distance from any point inside the velocity field to the rotation axis and is examined in more details in section 2.2. The cone, restricted to lengths $l^{*} \approx 0.6\,\mathrm{m}$, rotates with an angular velocity of Ω^{*} around the rotation axis and thus, along the circumferential coordinate θ. Therefore, the vector $\mathbf{\Omega}^{*}$ points opposite to the Cartesian X^{*}-direction. In the curvilinear coordinate system of the cone, the velocity vector is given by $\mathbf{u}^{*} = (u^{*}, v^{*}, w^{*})$. Note that at $Y^{*} = 0$ ($\equiv \theta = 0$), the circumferential velocity v^{*} is identical to the velocity V^{*} in the Cartesian coordinate system.

Figure 2.2 shows a side view of the cone's upper half and describes the flow-scenario considered in my master thesis: The super- and hypersonic axial inflow applied to a rotating cone leads to the viscous boundary layer forming above the wall [35]. Further, a shock wave forms and detaches from the wall due to the cone's rounded apex. Hence, the shock wave's origin is located in front of the cone and the distance from the shock to the cone's surface increases in streamwise direction [9]. In order to perform flow-field simulations and stability analysis, both of these regions have to

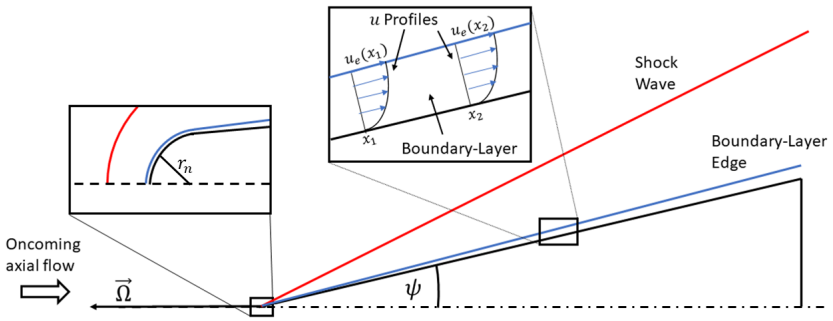

Figure 2.2.: Side-view of the cone's upper half: The boundary layer (blue) and shock wave (red) form with supersonic axial oncoming flow.

be resolved in great detail. The shock waves are examined in more detail in section 4.2.1 and the corresponding grid convergence study is given in section 4.2.2.
This work considers rounded cones with a nose radius of $r_n^* = 0.1\,\text{mm}$. Note that the introduced curvilinear coordinate system $\{x^*, \theta, z^*\}$ is not defined for the cone's nose. Therefore, the nose is excluded in the performed stability analysis.

2.2. Navier-Stokes Equations in Curvilinear Coordinate Systems

The Navier-Stokes equations are a set of partial differential equations to quantify the flow field of a Newtonian fluid. With the continuity equation 2.2.1, the momentum equation 2.2.2, the energy equation 2.2.3 and a state equation 2.2.4, this set describes the temporal and spatial behaviour of the respective fluid- and thermodynamical quantities.

Inertial (non-rotating) Coordinate Systems

The notation for the Navier-Stokes Equation follows the work of Aris [1], which also provides a more detailed derivation for transformations to general curvilinear coordinate systems with respect to the momentum equation. Note that only the notation for the derivatives differs, as in this work, it is given by e.g. $\partial_{x_i} T \equiv \frac{\partial T}{\partial x_i}$. For an alternative description of the notation (Einstein notation), see [32].

The Navier-Stokes equations for a compressible Newtonian fluid in a general non-rotating curvilinear coordinate system $\{x_1, x_2, x_3\}$ in non-dimensional contravariant form is given by [19]

$$0 = \partial_t \rho + \partial_{x_i} \left(\rho u^i\right) , \tag{2.2.1}$$

$$\begin{aligned} \rho \left(\partial_t u^i + u^j \partial_j u^i\right) = &-\partial_{x_j} p g^{ij} + \mathrm{Re}^{-1} \partial_{x_j} \left(\lambda \partial_{x_k} u^k g^{ij}\right) \\ &+ \mathrm{Re}^{-1} \mu \partial_{x_j} \left(g^{im} \partial_{x_m} u^j + g^{jn} \partial_{x_n} u^i\right) , \end{aligned} \tag{2.2.2}$$

$$\begin{aligned} \rho c_p (\partial_t T + u^i \partial_{x_i} T) - &(\gamma - 1) M^2 \left(\partial_t p + u_i \partial_{x_i} p\right) \\ = &\,\mathrm{Re}^{-1} \mathrm{Pr}^{-1} \partial_{x_i} \left(\kappa g^{ij} \partial_{x_j} T\right) \\ &+ \mathrm{Re}^{-1} (\gamma - 1) M^2 g_{ik} \left(\partial_{x_j} u^i\right) \cdot \\ &\left[\lambda \partial_m u^m g^{kj} + \mu \left(g^{km} \partial_{x_m} u^j + g^{jn} \partial_{x_n} u^k\right)\right] , \end{aligned} \tag{2.2.3}$$

$$\rho T = \gamma M^2 p \, . \tag{2.2.4}$$

For a cone's coordinate system, the coordinates and the velocity components are given by $x_i \in \{x, \theta, z\}$ and $u_i \in \{u, v, w\}$ as presented in section 2.1.
Further, T, p and ρ represent the thermodynamical quantities temperature, pressure and density respectively, whereas μ and λ are the dynamic and second viscosity. With ν as the kinematic viscosity, the dynamic viscosity is also defined as $\mu = \rho \cdot \nu$ and with the Stokes hypothesis, the second viscosity takes the form $\lambda = -\frac{2}{3}\mu$. Also, κ is the thermal conductivity and $\gamma = \frac{c_p}{c_v}$ stands for the heat capacity ratio, with the heat capacities c_p at constant pressure and c_V at constant volume.
The fluid- and thermodynamical quantities in Equations 2.2 are non-dimensionalised with specific reference values. The resulting dimensionless numbers in Equations 2.2 are the Reynolds, Prandtl and Mach numbers defined as [19]

$$\mathrm{Re} = \frac{l^*_{\mathrm{ref}} u^*_{\mathrm{ref}}}{\nu^*_{\mathrm{ref}}} \, , \; \mathrm{Pr} = \frac{\mu^*_{\mathrm{ref}} c^*_{p,\mathrm{ref}}}{\kappa^*_{\mathrm{ref}}} \, , \; M = \frac{u^*_{\mathrm{ref}}}{\sqrt{\gamma_{\mathrm{ref}} R^*_M T^*_{\mathrm{ref}}}} \, . \tag{2.3}$$

The state equation 2.2.4 describes the fluid as a perfect gas (see Appendix A). For isothermal and incompressible fluids, briefly introduced in chapter 3 for the rotating cone without inflow, the temperature, density and the viscosity are constant such that the energy equation is neglected and the continuity equation 2.2.1 takes the form $\partial^i_x u_i = 0$, which also simplifies the momentum equation 2.2.2. Additionally, the dimensional Navier-Stokes equations in the Cartesian coordinate system and a more detailed discussion of the non-dimensionalisation are listed in Appendix A.

In Equations 2.2, g_{ij} and g^{ij} are the components of the co- and contravariant metric tensor. For an orthogonal curvilinear coordinate system, only the diagonal elements are non-zero and the diagonals' square-roots are defined as the scale factors [1]

$$h_i = \sqrt{g_{ii}} \quad \text{with} \quad g_{ij} = \sum_{k=1}^{3} \frac{\partial X_i}{\partial x_k} \frac{\partial X_j}{\partial x_k} \,.$$

For the cone's coordinate system, the dimensionless scale factors take the form

$$h_1 \equiv h_x = 1 \,,\; h_2 \equiv h_\theta = x \sin(\psi) + z \cos(\psi) \;,\; h_3 \equiv h_z = 1 \,. \tag{2.4}$$

Hence, only the scale factor for the circumferential direction is unequal to one. At the wall, this scale factor also equals the local radius $r = x \sin(\psi)$, which therefore defines the minimal distance from the cone's wall to the rotation axis.
Together with the m_{ij}-terms defined as [19]

$$m_{ij} = (h_i h_j)^{-1} \frac{\partial h_i}{\partial x^j} \,,$$

the set of h_i and m_{ij} represent the metric terms, which are important for the stability analysis performed in chapters 3 and 5. As disturbances in the mean flow are described with a wave ansatz (cf. section 2.3.1), the m_{ij}-terms represent the divergence and curvature along the wave rays and fronts. For a cone, only m_{21} and m_{23} are non-zero due to the character of the scale factors and are given as

$$m_{21} = \sin(\psi)/h_\theta \quad \text{and} \quad m_{23} = \cos(\psi)/h_\theta \,. \tag{2.5}$$

Note that all m_{ij}-terms are equal to zero and all scale factors are equal to one, if a Cartesian coordinate system is considered. This is also the case for specific discussions in chapter 5, in which metric terms are excluded from the stability equations (cf. section 2.3.2).

Rotating Coordinate Systems

With the onset of rotation, two perspectives to describe the flow field are considered in this work. Either the flow field is interpreted in the non-rotating coordinate system, as described above, or the flow field is given in a coordinate system rotating along with the cone. Generally, the no-slip condition holds as no relative velocity

is present at the cone's wall. Whereas this leads to the circumferential velocity at the wall being equal to the wall's velocity in the non-rotating coordinate system, the circumferential velocity in the rotating coordinate system is zero at $z = 0$. In the rotating coordinate system, the acceleration in the non-dimensional momentum equation 2.2.2 is adjusted in order to include the change of the coordinate system's basis vectors with the rotation. These adjustments are the Coriolis and centrifugal acceleration and are defined as [24]

$$2\boldsymbol{\Omega} \times \mathbf{u} \quad \text{and} \quad \boldsymbol{\Omega} \times (\boldsymbol{\Omega} \times \mathbf{r}) \; . \tag{2.6}$$

The notation in Equations 2.6 is mostly common in the literature. However, in the notation of Equations 2.2, the Coriolis and centrifugal acceleration take the form

$$2\epsilon^{ijk}\Omega_j u_k \quad \text{and} \quad \epsilon^{ij}_{k}\epsilon^{kmn}\Omega_j\Omega_m r_n \, , \tag{2.7}$$

in which ϵ_{ijk} is the Levi-Civita symbol [32]. Both, Equations 2.6 and 2.7, are given in terms of the curvilinear coordinate system. It is apparent that the metric tensors g_{ij} and g^{ij} - and therefore scale factors - do not appear in the respective transformation of the Coriolis and centrifugal acceleration. This observation is further validated in chapter 3. The local radius $\mathbf{r}$ defines the distance between any given point in the flow field to the rotation axis, whereas $\boldsymbol{\Omega}$ and $\mathbf{u}$ are introduced in section 2.1 as the non-dimensional rotational-velocity vector and the velocity vector respectively. With the definition of the circumferential scale factor h_θ, the components of $\mathbf{r}$ at the position $\theta = 0$ simplify to

$$r_1 \equiv r_x = h_\theta \sin(\psi) \; , \; r_2 \equiv r_\theta = 0 \, , \; r_3 \equiv r_z = h_\theta \cos(\psi) \; . \tag{2.8}$$

Hence, this position $\theta = 0$ is used to define the plane in which the boundary layer is extracted and analysed (cf. section 4.2.3), as different θ-positions yield the same boundary-layer profiles, due to the rotational symmetry of a cone. Further, the rotational-velocity components in the cone's coordinate system are

$$\Omega_x = -\Omega \cos(\psi) \; , \; \Omega_\theta = 0 \, , \; \Omega_z = \Omega \sin(\psi) \; , \tag{2.9}$$

as the cone is defined to rotate in the circumferential direction (cf. section 2.1).

2.3. Linear Stability Theory

2.3.1. Fundamental Idea and Simplifications

In the linear stability theory, the flow-field's fluid- and thermodynamical quantities ($\mathbf{u}$, T, p, ρ) are decomposed into a steady basic flow $\bar{\xi}$ disturbed by an unsteady perturbation $\tilde{\xi}$ such that [19, 29]

$$\xi\left(x^i,t\right)=\bar{\xi}\left(x^i,t\right)+\tilde{\xi}\left(x^i,t\right)\,. \tag{2.10}$$

Introducing Equation 2.10 into Equations 2.2 for each mentioned quantity, subtracting the equations of the basic-flow and neglecting non-linear disturbance terms results in the linearised Navier-Stokes equations. This set of equations characterise the temporal and spatial behaviour of the disturbances in linear order.

For the disturbances, a wave ansatz is introduced. This ansatz is simplified, as the disturbances are assumed to not propagate in wall-normal direction. Further, the perturbation's amplitude does not depend on θ, as the basic flow is invariant in circumferential direction. The corresponding approach is then given by [19]

$$\tilde{\xi}\left(x,\theta,z,t\right)=\hat{\xi}\left(x,z\right)\exp\left(i\Theta\left(x,\theta,t\right)\right)+\text{c.c.}\,. \tag{2.11}$$

In Equation 2.11, $\hat{\xi}$ represents the wave's amplitude function, whereas c.c. denotes the complex conjugate form of the wave approach and Θ represents the wave's phase function. In the cone's curvilinear coordinate systems, Θ takes the form [19, 29]

$$\begin{aligned}\Theta&=h_x^2\int\frac{\alpha_c\left(x\right)}{h_x^2}\mathrm{d}x+h_\theta^2\int\frac{\beta_c}{h_\theta^2}\mathrm{d}\theta-\omega_c t\\&=\int\alpha_c\left(x\right)\mathrm{d}x+\beta_c\theta-\omega_c t\,.\end{aligned} \tag{2.12}$$

In this general approach, α_c and β_c are the complex streamwise and circumferential wavenumbers respectively and ω_c is the complex angular frequency.
In the local stability theory, the amplitude functions $\hat{\xi}$ are simplified to not depend on the streamwise coordinate [19]. Further, upstream information about the disturbances is neglected, which simplifies the phase function to

$$\Theta=\alpha_c x+\beta_c\theta-\omega_c t\,. \tag{2.13}$$

In addition to this locality assumption, the basic flow is also assumed to be parallel. Thus, not only streamwise derivatives are neglected but also the wall-normal velocity component [19]. However, in the local stability analysis of laminar boundary layers, which are approximated using the self-similarity approach for rotating cones in subsonic inflow as in the work of Segalini & Camarri [36] or Dechamps & Hein [8], the basic flow is often assumed to be non-parallel. The differences between non-parallel and parallel basic flows for the local stability analysis applied to the boundary layer of a rotating cone in still fluid approximated with the self-similarity approach is discussed in more detail in chapter 3. The cone's super- and hypersonic laminar boundary layers in chapter 5 are analysed with parallel-flow assumption.

Two theories in the stability analysis are distinguished: The spatial and the temporal theory [29]. In the temporal theory, the disturbance's behaviour with time is described with a complex angular frequency, whereas α is set to be a real number. Contrary, the spatial theory describes the disturbance's change in space with a complex streamwise wavenumber $\alpha_c = \alpha_r + i\alpha_i$ and a real angular frequency $\omega_c = \omega$. In this work, the spatial theory is applied. Further, the circumferential wavenumber is assumed to be real ($\beta_c = \beta$) and aligned with the circumferential direction of the cone's coordinate system, so that $\beta = 0$ holds for two-dimensional disturbances.
With all presented assumptions, the ansatz for the disturbances take the form

$$\tilde{\xi}\left(x, \theta, z, t\right) = \hat{\xi}\left(z\right) \exp\left[i\left(\left(\alpha_r + i\alpha_i\right) x + \beta\theta - \omega t\right)\right] . \tag{2.14}$$

Note that disturbances with $\omega < 0$ are interpreted to propagate in the opposite direction compared to their counterparts with $\omega > 0$. The negative imaginary part of α defines the spatial growth rate of the disturbance. Three cases are distinguished:

$$-\alpha_i \equiv \sigma \begin{cases} > 0 & \text{amplified} \\ = 0 & \text{neutral} \\ < 0 & \text{dampened} \end{cases} . \tag{2.15}$$

This work refers to parameter sets as neutral, if the amplification rate equals zero. For example, a neutral frequency denotes the frequency value, at which $\sigma = 0$. Further, the wavefront count can be defined as $n = \beta / h_\theta$ and describes the amount of wavefronts in circumferential direction. Because periodic boundary conditions apply in θ-direction, n must be an integer value only.

2.3.2. Linear Stability Equations and the NOLOT-Code

Introducing the disturbance ansatz into the linearised Navier-Stokes equations results in the underlying stability equations. Homogeneous boundary conditions are applied, so that the disturbances at the wall and in the free stream vanish for every disturbed quantity except the pressure, for which non-zero values are allowed at the wall. If the local stability theory is applied (including parallel-flow assumption), the resulting stability equations for the amplitude functions in the rotating curvilinear coordinate system of the cone is given by [19]

$$\mathbf{A}\hat{\boldsymbol{\phi}} + \mathbf{B}\frac{\partial\hat{\boldsymbol{\phi}}}{\partial z} + \mathbf{C}\frac{\partial^2\hat{\boldsymbol{\phi}}}{\partial z^2} = \mathbf{0} \quad \text{with} \quad \hat{\boldsymbol{\phi}} = \left(\hat{u}, \hat{v}, \hat{T}, \hat{w}, \hat{\rho}\right)^{tr} . \tag{2.16}$$

The matrices $\mathbf{A}, \mathbf{B}$ and $\mathbf{C}$ only contain basic-flow quantities as well as α, β and ω and are of order 5×5. The components are listed in the work of Hein et al. [19]. The work of Hein et al. [19] also presents the NOLOT-Code (NOnLOcal Transition analysis) and describes the code's discretization process, the solution procedure and a validation of the code.

Discussing the compressible flow of a rotating disk in still fluid using the self-similarity approach (cf. chapter 3), Dechamps & Hein [8] introduced a NOLOT-extension for rotational coordinate systems. Compared to the original NOLOT-Code, the extension included the Coriolis and centrifugal acceleration in the linearised Navier-Stokes equations, resulting in additional rotation terms in the underlying stability equations. Hence, the matrix $\mathbf{A}$ is modified. However, contrary to the statement in section 2.2 that the transition from the Cartesian to a general curvilinear coordinate system does not lead to scale factors in the Coriolis and centrifugal acceleration terms of the momentum equation, the NOLOT-extension presented in Dechamps & Hein [8] includes scale factors in the rotation terms. For example, the $(2,5)$-entry of matrix $\mathbf{A}$ in the NOLOT-extension [8] is given by

$$\begin{aligned}\mathrm{Re}^{-1} \cdot \mathbf{A}\,(2,5) = \frac{1}{\gamma M^2}\left(iT\frac{\alpha}{h_1} + \frac{1}{h_1}\frac{\partial T}{\partial x}\right) + U\frac{1}{h_1}\frac{\partial U}{\partial x} + W\frac{1}{h_3}\frac{\partial U}{\partial z} - m_{21}V^2 \\ + h_1\left(\frac{2\Omega_2 w}{h_3} - \frac{2\Omega_3 v}{h_2} + \Omega_1\Omega_2 x_2 + \Omega_1\Omega_3 x_3 - \Omega_2^2 - \Omega_3^2 x_1\right),\end{aligned}$$

with the adjustments due to the transformation into a rotational coordinate system marked red. In chapter 3, the NOLOT-extension code is validated. The investigation shows, that the statement of section 2.2 is correct and that the scale factors h_1, h_2

and h_3 have to be excluded from the red-marked NOLOT-extension. However, this does not affect the results presented in the work of Dechamps & Hein [8]. The corrected NOLOT-extension code is used in chapter 5 to perform local linear stability analysis for the super- and hypersonic laminar boundary layer of the cone. The influence of the rotation terms as well as the Coriolis and centrifugal-terms individually are of special interest.

2.4. Methods in Linear Stability Analysis

2.4.1. N-factors as a Global Measure of Disturbance Growth

N-factors are used in the e^N-method to predict the transition location between laminar and turbulent flow. However, in order to perform a grid convergence study in section 4.2.2, only N-factors are of interest in this work. For more information on the e^N-method, see Ref. [46].
In local (parallel) stability theory, the spatial growth rate σ is given by the negative imaginary part of the streamwise wavenumber α (cf. section 2.3.1). The integration of the growth rate with respect to a reference position x_0 defines the N-factor as [46]

$$N = \int_{x_0}^{x} \sigma\left(x'\right) \mathrm{d}x' \,, \tag{2.17}$$

with x_0 conventionally being the neutral position at which $\sigma(x = x_s) = 0$. The N-factor represents the accumulated growth of the disturbance between x_0 and the general position x and therefore provides a global measure of the disturbance growth along the considered object.
In section 4.2.2, N-factor curves are computed to perform a grid convergence analysis to determine the required resolution for the basic-flow simulations.

2.4.2. NOLOT-Input File and Manipulation

In general, the NOLOT-input file contains the basic flow, metric terms and the information for the rotation terms (cone's rotation rate and local radius components) at different streamwise locations in increasing order. Hence, the development of the considered instabilities along the cone can be tracked by sweeping through the

different locations of the input file. Further, single positions can be analysed by selecting the respective location in the input file. The wavenumber β or the angular frequency ω can be varied to gain information about the instabilities' behaviour in the parameter space $[\alpha_r, \alpha_i, n, \omega]$.

Furthermore, the influence of individual terms can be considered at single locations on the cone by artificially reducing the respective terms in the NOLOT-input file. This method is applied in section 5.4.2 to determine the influence of the rotation terms as well as the Coriolis and centrifugal terms individually on the considered instabilities. The first entry in the NOLOT-input file represents the default setting, in which each quantity is not modified, whereas in the last entry, the terms of interest are set to zero in the stability analysis. In between, a decreasing factor - in section 5.4.2 referred to as ζ - reduces the influence of the respective terms. For the rotation terms, the decreasing factor reduces the rotation rate. In order to reduce the centrifugal terms in the same linear order as the Coriolis terms, the local radius components are increased using the inverted factor. For the Coriolis terms, the method is applied similar to the rotation terms. But the inverted factor, which increases the local radius components, is squared in order to keep the centrifugal terms constant. Finally, the centrifugal terms are reduced by decreasing the local radius components.

Moreover, the transition between two arbitrary rotation rates $\bar{\Omega}_1$ and $\bar{\Omega}_2$ can be enabled (the rotation rates are specified in section 4.3).
Let $\xi_{i,\bar{\Omega}_1}$ and $\xi_{i,\bar{\Omega}_2}$ refer to a general quantity ξ_i listed in the NOLOT-input file computed for $\bar{\Omega}_1$ and $\bar{\Omega}_2$ respectively. Then, the transition is performed by introducing a factor χ, such that

$$\xi_{i,\mathrm{trans}}(\chi) = \chi \xi_{i,\bar{\Omega}_1} + (1-\chi)\, \xi_{i,\bar{\Omega}_2}\,. \tag{2.18}$$

The first entry contains the basic flow for $\bar{\Omega}_1$, as $\chi = 1$ holds. With the decrease of χ along the entries in the NOLOT-input file, $\bar{\Omega}_2$ becomes more dominant in the basic-flow and is listed entirely at the last entry.
This method is used throughout chapter 5 to track instabilities, whose growth rates decrease with decreasing rotation intensity.

3. Validation of the NOLOT-Extension Code - Self-Similarity Approach for the Rotating Cone in Still Fluid

As mentioned in section 2.3, the NOLOT-extension presented in the work of Dechamps & Hein [8] included scale factors in the rotation terms of the stability equations for rotational coordinate systems. As it is stated in section 2.2, that the Coriolis and centrifugal acceleration have no scale factors in the curvilinear coordinate system, the NOLOT-extension is validated in this chapter.
Therefore, the self-similarity approximation for the boundary layer of a rotating cone in still, incompressible and isothermal fluid is considered. Two versions are distinguished, differing in the choice for the characteristic length. Although both versions lead to the same equations of motion, the absolute values of the basic-flow's fluid-dynamical quantities in the NOLOT-input files differ due to the different non-dimensionalisation; however, the stability-analysis results focusing on the stationary Crossflow-Instability have to match per definition, such that differences can be interpreted as mistakes in the underlying stability equations.
In the work by Dechamps & Hein [8], a similar setup is considered, as the NOLOT-extension is used for the compressible self-similarity solution of a rotating disk (cf. [44]). Because the disk equals a 90°-cone, this work is used as a reference for the validation of the code.
In the works of Hussain et al. [12, 21] and Segalini & Camarri [36], other half-opening angles ($\psi > 40°$) have been considered to which the additional analysis given in section 3.2.2 is compared to.

3.1. Derivation of the Self-Similarity Equations

This section presents the derivation of the equations of motion for the self-similarity approach applied to the incompressible, isothermal flow around a rotating cone without inflow. The derivation is inspired by the work of Segalini & Camarri [36], however this work focuses on the step, at which the different characteristic lengths are introduced. If both presented choices for the characteristic length scale lead to the same equations of motion, the stability analyses have to produce the same results.
Non-essential equations or equations that have already been used in the literature are are only referenced. Further, a more detailed derivation is given in Appendix B.

In the frame of the rotational coordinate system and therefore with the inclusion of the Coriolis and centrifugal terms, the dimensional form of the incompressible, isothermal Navier Stokes Equations in terms of the cone's coordinate system $\{x^*, \theta, z^*\}$ is given in [20, Eq. 2.6-2.10].
First, the Navier-Stokes Equations have to be non-dimensionalised using general characteristic scales for the length, the velocity and the pressure such that

$$\begin{aligned} (x^*, z^*) &= (x, z) \cdot l^*_{\mathrm{ref}}\,, \\ (u^*, v^*, w^*) &= (u, v, w) \cdot u^*_{\mathrm{ref}}\,, \\ p^* &= \rho^* \cdot \left(u^*_{\mathrm{ref}}\right)^2\,. \end{aligned} \tag{3.1}$$

Exemplary, this leaves the streamwise momentum equation at

$$\begin{aligned} &\underline{\frac{\partial u}{\partial t}} + u\frac{\partial u}{\partial x} + \underline{\frac{v}{h}\frac{\partial u}{\partial \theta}} + w\frac{\partial u}{\partial z} - \frac{v^2\sin(\psi)}{h} - 2v\frac{\Omega^* l^*_{\mathrm{ref}}\sin(\psi)}{u^*_{\mathrm{ref}}} - h\frac{\left(\Omega^* l^*_{\mathrm{ref}}\right)^2\sin(\psi)}{\left(u^*_{\mathrm{ref}}\right)^2} \\ &\quad = \frac{1}{\mathrm{Re}}\left(\Delta u + \underline{\frac{2\sin(\psi)}{h}\frac{\partial v}{\partial \theta}} - \frac{(u\sin(\psi) + w\cos(\psi))\sin(\psi)}{h}\right)\,, \end{aligned} \tag{3.2}$$

in which the Reynolds number is defined similar to Equation 2.3. The Laplace operator Δ is taken from [20, Eq. 2.10] and is non-dimensionalised with l^{*-2}_{ref}, as its only dimensional quantities are the scale factors and the spatial derivatives of second order (cf. Appendix B). The other components of the momentum equations and the continuity equations are dealt with analogously. Terms regarding the time and the circumferential direction (underlined in Equation 3.2) are neglected because only the stationary solution of this axisymmetric setup is of interest.

Next, the reference quantities have to be defined specifically.
Two possibilities for the characteristic length l^*_{ref} are distinguished in this chapter: On the one hand $\delta^* = \sqrt{\nu^* / (\Omega^* \sin(\psi))}$, which represents a characteristic length scale for the wall-normal direction and is referred to as version 1 (V1). In the literature [21, 36], this quantity is referred to as the cone's boundary-layer thickness; however, as the boundary-layer profiles in Figure 3.1 show, this definition is not accurate. On the other hand a characteristic length scale L^* for the streamwise direction, which is referred to as version 2 (V2). For V2, any streamwise-related length scale suffices, such as the length of the cone or the local radius; however, the current position $L^* = x^*_s$ is chosen equivalently to the work of Dechamps & Hein [8]. Note that the quantity x^*_s is not affected by the derivative in streamwise direction. Although version 2 simplifies the representation of many quantities in the NOLOT-input file, such as the metric terms or the local radius components, version 1 is more commonly used in the literature, for example in the work of Segalini & Camarri [36] or in any work by Hussain and Garrett et al., that is remotely related to the self-similarity approach for flow around a rotating cone [12, 15, 20, 21].
In order to solve the boundary-layer equations as an approximation of the Navier-Stokes Equations, the quantity $\epsilon = \delta / x_s \ll 1$ is introduced. Further, the wall-velocity at each position x^*_s on the cone respectively defines the reference velocity as $u^*_{\text{ref}} = x^*_s \Omega^* \sin(\psi)$.
For both versions, the corresponding fluid-dynamical quantities and the resulting modifications for Equation 3.2 are summarised in Table 3.1. The table also introduces the quantities x_δ, z_δ, x_L and z_L, which represent the streamwise and wall-normal coordinates non-dimensionalised using either δ^* or $L^* = x^*_s$. The aim is to formulate the boundary layer equations in terms of x_L and z_δ, to weigh the respective terms against each other and sort the equations in orders of ϵ.

Finally, the self-similarity approach is applied. For both versions, it is assumed that the form of the streamwise and circumferential velocity profiles are preserved along the cone and that they only change quantitatively. Further, the wall-normal component is assumed to scale with the boundary layer thickness. This results in the ansatz $(u, v, w) = (x_L u_0(z_\delta), x_L v_0(z_\delta), \epsilon w_0(z_\delta))$. The pressure is also assumed to be self-similar with the position on the cone, such that $p = \epsilon x_L \cot(\psi) p_0(z_\delta)$. However, the change of the pressure in wall-normal direction is negligible [45], leading to $\partial p_0(z_\delta) / \partial z_\delta = 0$. This is tested for the 70°-cone in Appendix C.

From here on, the z_δ-dependency is not written out in the equations (i.e. $u_0 \equiv u_0(z_\delta)$). Inserting the quantities of Table 3.1 and the self-similarity approach into the non-dimensionalised Navier-Stokes equations leaves each term with a specific order $\mathcal{O}(\epsilon)$, which have to be sorted and neglected accordingly. Exemplary shown using the streamwise momentum equation again, for version 1, the terms of order $\mathcal{O}(\epsilon)$ are kept, whereas for version 2, terms of order $\mathcal{O}(1)$ lead to the same differential equation:

$$\begin{aligned}
\text{V1:} \quad & \epsilon x_L u_0 \frac{\partial x_L u_0}{\partial x_L} + \epsilon w_0 \frac{\partial x_L u_0}{\partial z_\delta} - \epsilon x_L \left(v_0^2 + 2v_0 + 1\right) = \epsilon x_L \frac{\partial^2 u_0}{\partial z_\delta^2}\,, \\
\text{V2:} \quad & x_L u_0 \frac{\partial x_L u_0}{\partial x_L} + \epsilon w_0 \frac{1}{\epsilon} \frac{\partial x_L u_0}{\partial z_\delta} - x_L \left(v_0^2 + 2v_0 + 1\right) = x_L \frac{\partial^2 u_0}{\partial z_\delta^2}\,.
\end{aligned}$$

For the continuity equation and the momentum equations in each direction, this leaves the self-similarity approximation for the incrompressible flow around a rotating cone without outer flow as

$$\begin{aligned}
\text{cont. eq.:} \quad & 2u_0 + w_0' = 0\,, \\
\text{mom. eq. in x-dir.:} \quad & w_0 u_0' + u_0^2 - (v_0 + 1)^2 = u_0''\,, \\
\text{in y-dir.:} \quad & w_0 v_0 + 2u_0 (v_0 + 1) = v_0''\,, \\
\text{in z-dir.:} \quad & (v_0 + 1)^2 = p_0' \approx 0\,,
\end{aligned} \tag{3.3}$$

in which the superscript $'$ denotes the z_δ-derivative. Note that v_0**+1** is a reminiscence of the rotational coordinate system and represents the Coriolis and centrifugal terms in this approximation.

Both presented versions lead to the same set of equations to describe the basic flow in the self-similarity approximation. However, it was important to proof this assumption, to rule out any differences due to the length scale choice. Therefore, the statement is validated, that both versions must lead to identical stability analysis results.

Because only the second-order derivative in the wall-normal direction remains from the right-hand-side's viscous terms, Equations 3.3 depict two differential equations of second order and one of first order, which can be rewritten into a system containing five differential equations of first order that is solvable using the *solve_bvp*-function of the PYTHON-module *scipy*.

As boundary conditions, the no-slip condition is assumed and far from the cone's wall (indicated by $z_\delta \to \infty$), the streamwise velocity component vanishes due to the lack of inflow, whereas in the rotational coordinate system, the circumferential component takes the negative value of the cone's rotation. With the above presented non-dimensionalisation, this leads to

$$z_\delta = 0: \quad u_0 = v_0 = w_0 = 0\,, \qquad z_\delta \to \infty: \quad u_0 = 0,\, v_0 = -1\,. \tag{3.4}$$

Equations 3.3 and 3.4 can generally be solved for every rotation velocity as well as for any half-opening angle. The latter is due to the definition of the boundary-layer thickness δ^*: If $\sin(\psi)$ is not included, it will appear in some terms of Equation 3.3 (cf. [15]). The results of Equations 3.3 and 3.4 are shown in Figure 3.1 with the profiles of Fildes et al. [12] included for comparison, being in good agreement with the presented self-similarity solution.

Table 3.1.: Comparison between Version 1 ($l^*_{ref} = \delta^*$) and Version 2 ($l^*_{ref} = L^*$) of the non-dimensionalisation of different quantities.

Quantity	Abbrev.	Version 1	Version 2
Char. Length	l^*_{ref}	$\delta = \sqrt{\frac{\nu^*}{\Omega^* \sin(\psi)}}$	$L^* = x^*_s$
Fluid-dynamical Values:			
Reynolds number	Re	$\frac{\delta^* x^*_s \Omega^* \sin(\psi)}{\nu^*} = \frac{1}{\epsilon}$	$\frac{x^*_s x^*_s \Omega^* \sin(\psi)}{\nu^*} = \frac{1}{\epsilon^2}$
local Reynolds number	Re_l	Re	$\sqrt{\mathrm{Re}}$
Coordinate Transformation:			
	x_δ	x	x/ϵ
	x_L	ϵx	x
	z_δ	z	z/ϵ
	z_L	ϵz	z
Scale Factor	h_θ	$x_L/\epsilon \sin(\psi)$ $+\ z_\delta \cos(\psi)$	$x_L \sin(\psi)$ $+\epsilon z_\delta \cos(\psi)$

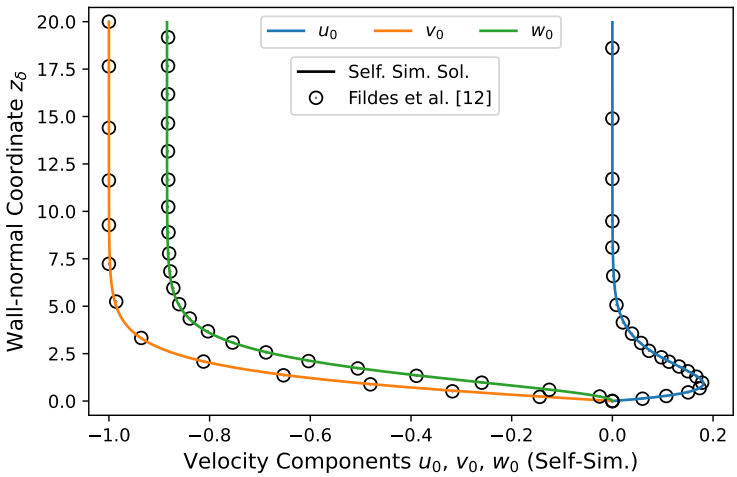

Figure 3.1.: Boundary-layer profiles of the basic flow in the self-similarity approximation: The velocity components u_0 (blue), v_0 (orange) and w_0 (green) are compared to the literature [12] (circles).

3.2. Local Stability Analysis Results for the Self-Similarity Approach

This section provides results of the stability analysis for the rotating cone's boundary layer in still fluid, approximated with the self-similarity approach presented above. The stability analysis focuses on the the stationary Crossflow-Instability, comparing this work's results with the literature [8, 21, 36].
Firstly, the code validation of the in Dechamps & Hein [8] presented extension of the NOLOT-code [19] for stability analyses in rotating frames of references is performed. As the NOLOT-extension is corrected, an analysis of the Crossflow-Instability is given, comparing the results computed with NOLOT to the literature and briefly introducing methods used in chapter 5 to analyse the rotating cone with super- and hypersonic inflow.

3.2.1. Code-Validation for the Rotating Disk

For the NOLOT-input file containing the basic-flow data, the non-dimensionalisation has to be performed consistently. Hence, either the coordinate set $\{x_\delta, z_\delta\}$ (V1) is used or the set $\{x_L, z_L\}$ (V2). Each version leads to different adjustments for the

derivatives, because the self-similarity solution is computed in terms of $\{x_L, z_\delta\}$. However, the stability analysis results must match per definition because they are based on the same basic flow, as it is shown in section 3.1.

The thermodynamic reference values have been adopted from Dechamps & Hein [8] and approximately represent atmospheric conditions ($T^*_\infty = 300\,\mathrm{K}$, $p^* \approx 101.3\,\mathrm{kPa}$, $\nu^* \approx 1.57 \cdot 10^{-5}\,\frac{\mathrm{m}^2}{\mathrm{s}}$). These values are used throughout the next sections. This also holds for the rotational speed of $\Omega^* \approx 0.77\,\mathrm{Hz}$. However, because the rotation rate is included in the definitions of δ^* and the local Reynolds number, the absolute value of Ω^* is only restricted to be greater than zero. For example, a rotation rate of $\Omega^* \approx 0.77\,\mathrm{Hz}$ leads to the same neutral curve in the non-dimensional α_r-Re_l-space as a rotation rate of $\Omega^* \approx 100\,\mathrm{Hz}$. Similar to the literature [8, 36], the analysis is performed in a non-parallel manner, which includes streamwise derivatives in the stability equations. As this procedure differs to the stability analysis presented in chapter 5 for the super- and hypersonic boundary layer of the rotating cone, section 3.2.2 examines the differences of parallel and non-parallel analyses in more detail.

In the work of Dechamps & Hein [8], the NOLOT-extension for stability analysis in rotating frames of references has been applied on V2 and scale factors were still included in the rotation terms of the stability equations. This NOLOT-version is referred to as "old NOLOT-ext." and has initially been used in this work as well to analyse the stationary Crossflow-Instability of the rotating disk for both the V1- and the V2-version. Figure 3.2(a) shows the respective neutral curves for the streamwise wavenumber α_r, varying the position on the cone and therefore the local Reynolds number $Re_l = \delta^* x_s^* \Omega^* \sin(\psi) / \nu^*$ (cf. Table 3.1). The circles indicate the neutral curve presented by Dechamps & Hein [8].
The domain enclosed by the literature's neutral curve [8] is divided into two different types of instability. The generally more unstable mode is more dominant for high streamwise and circumferential wavenumbers and is referred to as Type-I mode in the literature. The unstable domain in the α_r-Re_l-space for low streamwise and circumferential wavenumbers is consistently being referred to as Type-II mode. Both types are characterised using the neutral local Reynolds number $\mathrm{Re}^{I/II}_{l,\mathrm{n}}$ and are examined in more detail in the next section.
Using the old NOLOT-extension, the neutral curve computed with V2 only shows small discrepancies with the results presented by Dechamps & Hein [8], which can be explained with the different basic flows. Dechamps & Hein [8] implemented a self-

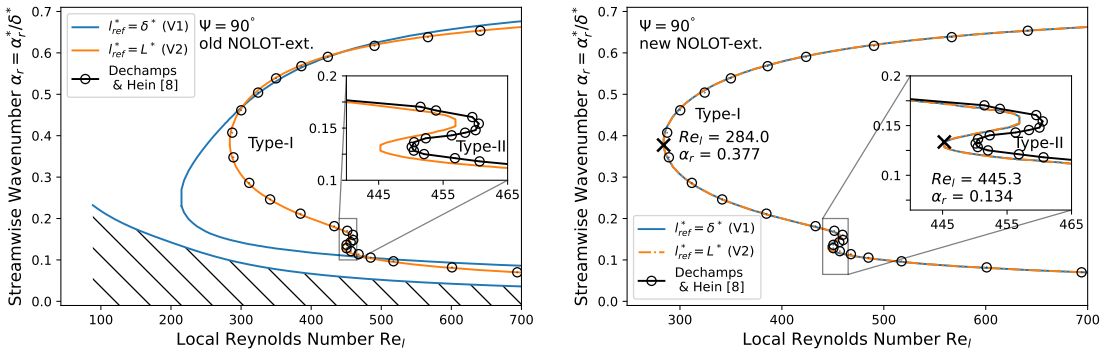

(a) (b)

Figure 3.2.: Neutral curves of the stationary Crossflow-Instability in the α_r-Re_l-space for the rotating disk computed with the old NOLOT-extension [8] (a) and the corrected NOLOT-extension (b): In (a), the black parallel lines denote an unstable domain, whose boundaries could not be resolved.

similarity solver for a disk rotating in a compressible fluid, that has been reported to have a stabilising effect on subsonic boundary layer compared to incompressible flows (cf. [29, 34]). This is, for example, due to non-zero temperature derivatives caused by the compressibility. But the differences only show up in the absolute values of the neutral local Reynolds numbers and do not affect the form of the neutral curves.

Using δ^* as a characteristic length in V1 leads to a different result. Two unstable domains are observed in the α_r-Re_l-space: Indicated by the black parallel lines, the unstable area for low streamwise wavenumbers extends to negative α_r and smaller local Reynolds numbers as well. However, the neutral curve in that domain could not be resolved. Further, the neutral curve for high streamwise wavenumbers does not depict both types of instabilities and the unstable domain in the α_r-Re_l-space extends to lower local Reynolds numbers compared to V2.

The observed differences indicate that the old NOLOT-extension was incorrect because the scale factors have falsely been included in the rotation terms. However, this did not affect the computations of either Dechamps & Hein [8] or for V2 due to the choice of the reference length. As shown in Table 3.1, the only non-zero non-dimensional scale factor takes the form $h_\theta = x^*/L^* \sin(\psi)$. With the location on the cone as characteristic streamwise length and with the disk resembling the extreme case of a 90°-cone, the scale factor takes a value of $h_\theta = 1$ for all wall-normal

coordinates. It equals the case of scale factors not being included in the rotation terms and therefore results in the correct neutral curves.

The error in the stability equations has been corrected and the corresponding neutral curves in the α_r-Re_l-space are shown in Figure 3.2(b). Perfect resemblance is reached and the curves are indeed in agreement with the results of V2 computed with the old NOLOT-extension. The smaller neutral local Reynolds numbers compared to Dechamps & Hein [8] are due to the different basic flows, however the qualitative resemblance has been reproduced. The neutral Reynolds numbers for different half-opening angles are also given in the next section in Table 3.2.

3.2.2. Code-Validation for the Rotating Cone

As section 3.2.1 only validates the NOLOT-extension for the rotating disk, this section generalises this validation for the rotating cone. Therefore, stability analysis results with the corrected stability equations are presented for the boundary layer of the rotating cone in still fluid approximated with the self-similar solution presented in section 3.1.
Different half-opening angles are considered to analyse their effect on the cones' boundary layer and the analysis focuses on the stationary Crossflow-Instability.
Version 1 is used such that $l^*_{\mathrm{ref}} = \delta^*$ non-dimensionalises every length-related quantity from here on. An additional investigation on the differences between parallel and non-parallel computations is given as well.
To validate of the corrected NOLOT-extension, the results are compared to the literature, for example the works of Segalini & Camarri [36] and Hussain et al. [21].
Further, analysing methods are introduced, which are also used in chapter 5, and presenting stability analysis results for the Crossflow-Instability in still incompressible fluids allows a comparison to the Crossflow-Instability observed in supersonic compressible fluids.

Cone with Half-Opening Angle of 60°

In the work of Segalini & Camarri [36], an extensive stability analysis was performed for the 60°-cone, which is used as a reference. First, the neutral curve in the n-Re_l-space is visualised in Figure 3.3(a), with n being the wavefront count as introduced in section 2.3. The two different curves represent computations with the inclusion of

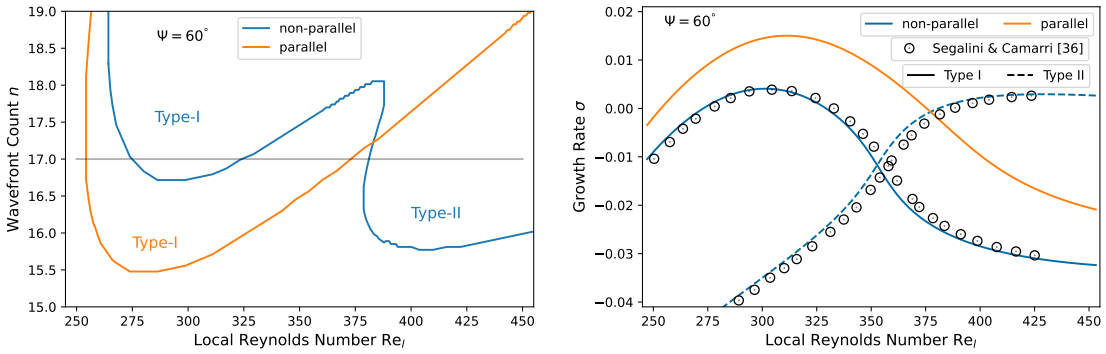

(a) (b)

Figure 3.3.: (a) Neutral curves of the stationary Crossflow-Instability in the α_r-Re_l-space for the cone with $\psi = 60°$, (b) growth-rate curves with respect to the local Reynolds number: Both (a) and (b) compare non-parallel (blue) and parallel (orange) local stability analysis results. The black line in (a) defines the wavefront-count value ($n = 17$) considered in (b).

streamwise derivatives as well as the wall-normal velocity component (non-parallel) and without their inclusion (parallel) in the stability equations. For the latter, the Type-II mode's neutral local Reynolds number is shifted to a parameter range outside of this figure's frame so that the mode destabilises at a position further downstream. Hence, the Type-II mode gets destabilised with the assumption of parallel basic flow. Oppositely, the Type-I mode stabilises, with the neutral point of the non-parallel computation being located at higher circumferential wavenumbers and local Reynolds numbers compared to the parallel analysis (cf. Tables 3.2 & 3.3).

As mentioned in chapter 2, local stability theory is usually linked with parallel computation. However, this section presents both parallel and non-parallel stability analysis results, because both methods are used in the literature regarding self-similarity approaches for rotating cones/disks in still fluid (cf. parallel: [12], non-parallel: [8, 36]), whereas in chapter 5, the stability analyses performed for the laminar boundary layer of a rotating cone in super- and hypersonic inflow are computed with the parallel-flow assumption and therefore without the wall-normal velocity component (cf. [39]).

The black line in Figure 3.3(a) represents the section in the n-Re_l-space considered in Figure 3.3(b), which shows the growth-rate evolution with the local Reynolds number for the waves with a wavefront count of $n = 17$. Again, the orange curve

presents the results for parallel computations, whereas the blue curves represent the non-parallel stability analysis results. Due to the Type-II mode not being unstable in the considered parameter range for parallel computations, only one growth-rate curve is plotted in Figure 3.3(b). Hence, the figure again shows, that, with the inclusion of the streamwise derivatives, the Type-I mode stabilises and the Type-II mode destabilises in the considered domain. The black circles visualise the results presented by Segalini & Camarri [36], with good agreement being reached for both instability types. Note that in the work of Segalini & Camarri [36], parallel computations do not refer to the exclusion of streamwise derivatives but the neglect of the "streamwise evolution of the eigenvalues and eigenfunctions" [36, chap. I.]. In this work, this is referred to as local computations (cf. chapter 2). The small discrepancies between the NOLOT-computation results and those of Segalini & Camarri [36] are noted and are most likely numerical errors or caused by small differences in the basic flow. Hence, the comparison in Figure 3.3(b) validates the corrected NOLOT-extension for the cone's geometry.

Further, Figure 3.4 shows that the corrected NOLOT-extension computes physically valid amplitude functions for the stationary Crossflow-Instability. Here as well as in chapter 5, amplitude functions are used to characterise the respective instability types and therefore to differentiate between modes which occupy parameter-space

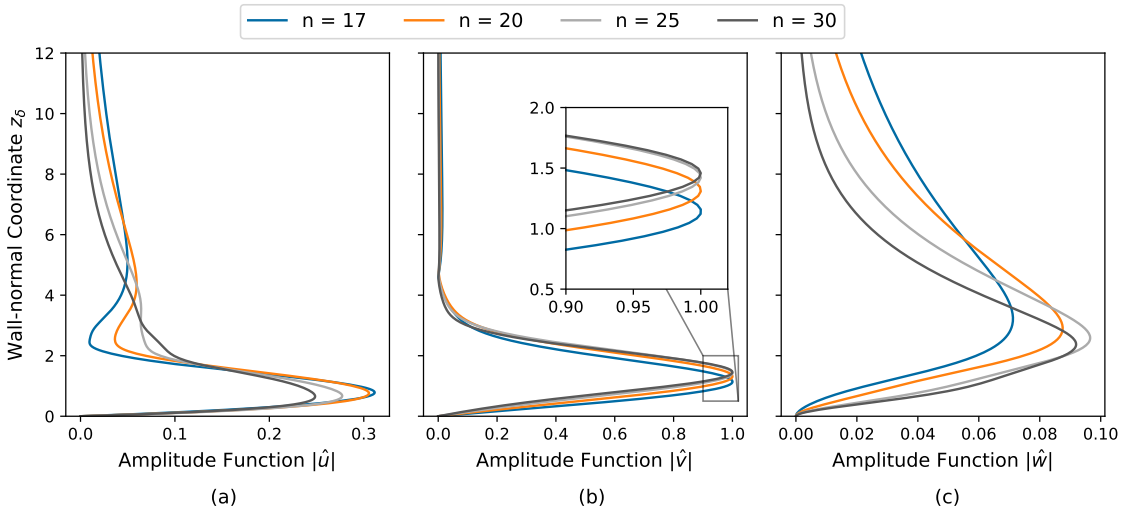

Figure 3.4.: Amplitude functions $|\hat{u}|$ (a), $|\hat{v}|$ (b) and $|\hat{w}|$ (c) of the stationary Crossflow-Instability for different wavefront counts n: The increase from $n = 17$ (blue) to $n = 30$ (dark grey) visualises the transition in the parameter space from Type-I to Type-II stationary Crossflow-Instability.

domains in close vicinity. Therefore, Figure 3.4 considers the velocity amplitude functions $|\hat{u}|$, $|\hat{v}|$ and $|\hat{w}|$ for a local Reynolds number of $\mathrm{Re}_l = 390$, increasing the wavefront count from $n = 17$ to $n = 30$.
Most distinctively, the circumferential velocity function is the dominant disturbance factor, but this is expected due to the lack of external flow, the fluid being incompressible and pressure gradients being negligible such that the cross-flow velocity represents the driving mechanism for the Crossflow-Instability [2, 28]. The circumferential velocity amplitude function consists of one global maximum, which can be used for the classification of the instability types: For $n = 17$, the Type-II mode is dominant, with the maximum being located at $z_\delta \approx 1.1$ and shifting towards higher wall-normal coordinates with the increase of the wavefront count. However, for $n = 25$, the Type-I mode becomes the dominant instability, as the maximum at $z_\delta \approx 1.5$ does not change with the wavefront count increase to $n = 30$. Moreover, for the Type-II mode an additional local maximum at $z_\delta \approx 5$ in the $|\hat{u}|$-amplitude function is observable.

Cones with different Half-Opening Angles

This section compares parallel and non-parallel stability analyses in more detail, as the stationary Crossflow-Instability in the boundary layer of the rotating cone in otherwise still, incompressible fluids is analysed for different half-opening angles ψ.

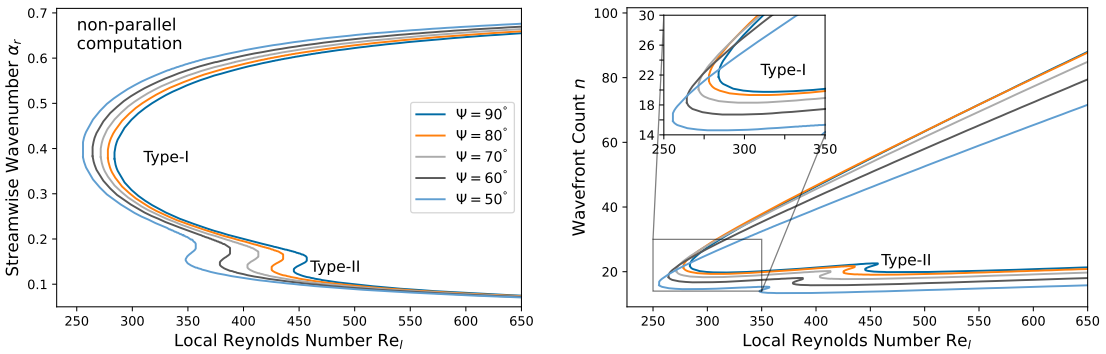

(a) (b)

Figure 3.5.: Neutral curves of the stationary Crossflow-Instability in the α_r-Re_l-space (a) and n-Re_l-space (b) for non-parallel stability analysis and different half-opening angles.

The analysis focuses on angles $\psi > 40°$ because for lower angles, the Centrifugal-Instability is reported to become more dominant [21, 23]. Figure 3.5 visualises the neutral curves in the α_r-Re_l-space (a) and the n-Re_l-space (b) respectively for half-opening angles between $\psi = 50°$ and $\psi = 90°$ for non-parallel computations. Both the Type-I and the Type-II modes destabilise with the decreasing half-opening angles, which is indicated by the decreasing neutral local Reynolds numbers $\mathrm{Re}_{l,\mathrm{n}}^{I/II}$, which are listed in Table 3.2 together with the neutral wavenumbers.
As Segalini & Camarri [36] did not consider half-opening angles other than $\psi = 60°$, the analysis in Figure 3.5 lacks references for comparison. However, Figures 3.2(b) and 3.3 show, that this work's non-parallel stability analysis reproduces the results for $\psi = 90°$ (disk) in the work of Dechamps & Hein [8] and the results for $\psi = 60°$ in the work of Segalini & Camarri [36]. Hence, the neutral curves for the other half-opening angles are assumed to be correct as well.

Figure 3.6 visualises the neutral curves in the α_r-Re_l-space (a) and the n-Re_l-space (b) respectively for half-opening angles between $\psi = 50°$ and $\psi = 90°$ for parallel computations. As for the non-parallel computation, both the Type-I and the Type-II modes destabilise with the decreasing half-opening angles. Further, parallel computations stabilise the Type-II mode and slightly destabilise the Type-I mode, which transfers to the other half-opening angles as well. The respective neutral local Reynolds numbers and the neutral wavenumbers $\mathrm{Re}_{l,\mathrm{n}}^{I/II}$ are listed in Table 3.3. The destabilising effect has also been reported in the work of Fildes et al. [12]. However,

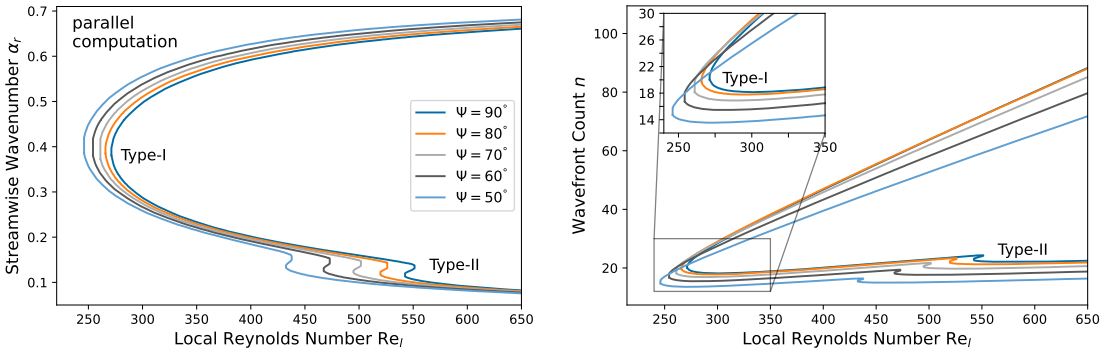

(a) (b)

Figure 3.6.: Neutral curves of the stationary Crossflow-Instability in the α_r-Re_l-space (a) and n-Re_l-space (b) for parallel stability analysis and different half-opening angles.

the neutral Reynolds numbers are not in agreement for neither the non-parallel nor the parallel computations. Hence, a more detailed comparison between the stability equations presented in the work of Fildes et al. [12] and implemented in the corrected NOLOT-extension must be considered in future studies.

Table 3.2.: Neutral parameters of the stationary Crossflow-Instability for non-parallel stability analysis.

	non-parallel computations							
	Type-I				Type-II			
ψ	$\mathrm{Re}^{I}_{l,n}$	α_r	β	$\approx n$	$\mathrm{Re}^{II}_{l,n}$	α_r	β	$\approx n$
90°	284.0	0.377	0.0476	22	445.3	0.134	0.0458	21
80°	278.0	0.379	0.0494	21	425.3	0.139	0.0470	20
70°	271.6	0.381	0.0517	20	403.6	0.143	0.0481	19
60°	264.3	0.383	0.0544	18	378.8	0.149	0.0495	17
50°	255.6	0.381	0.0579	16	348.0	0.156	0.0512	14

Table 3.3.: Neutral parameters of the stationary Crossflow-Instability for parallel stability analysis.

	parallel computations							
	Type-I				Type-II			
ψ	$\mathrm{Re}^{I}_{l,n}$	α_r	β	$\approx n$	$\mathrm{Re}^{II}_{l,n}$	α_r	β	$\approx n$
90°	271.3	0.381	0.0363	20	542.5	0.120	0.0421	23
80°	265.8	0.385	0.0380	20	519.7	0.124	0.0431	22
70°	261.1	0.373	0.0385	18	494.8	0.126	0.0437	21
60°	254.2	0.379	0.0408	17	467.3	0.132	0.0451	19
50°	246.0	0.386	0.0440	15	432.5	0.138	0.0466	16

4. Laminar Basic Flow Computation

As the NOLOT-extension, presented in the work of Dechamps & Hein [8], has been corrected and validated in chapter 3, the aim is to perform local linear stability analyses for the laminar boundary layers of rotating cones ($\psi \in [5°, 7°, 10°, 15°]$) in super- and hypersonic axial oncoming flow. Therefore, the basic flows for each setup must be simulated. Note that the boundary layers of these setups are not approximated using a self-similarity ansatz. In chapter 3, this approach is only used to simplify the process of the code validation of the NOLOT extension. However, a comparison between the stability-analysis results using numerical simulations and the less accurate self-similarity approach to determine the basic flows of rotating cones in super- and hypersonic oncoming flow could be of interest for future work.

The procedure to obtain the basic flow is visualised in Figure 4.1. The grids are prepared using the grid-construction tool *MEGACADS* [3]. Therefore, the position of the compression shock is computed, as these regions must be resolved in more detail (cf. section 4.2.1). In section 4.2.2, a grid convergence study is performed in order to determine the amount of grid points necessary to ensure the simulation's quality.
The basic flows are computed using the flow solver TAU of the DLR (cf. section 4.1). Simulations without rotation determine the reference values in order to compute the rotation rates for each setup (cf. section 4.3). In order to perform linear stability analysis, the laminar the boundary layers are extracted of the flow solution and the NOLOT-input files are prepared. Therefore, the metric terms are computed analytically as described in section 2.2.
In section 4.3, the basic flow is compared to the literature [39].

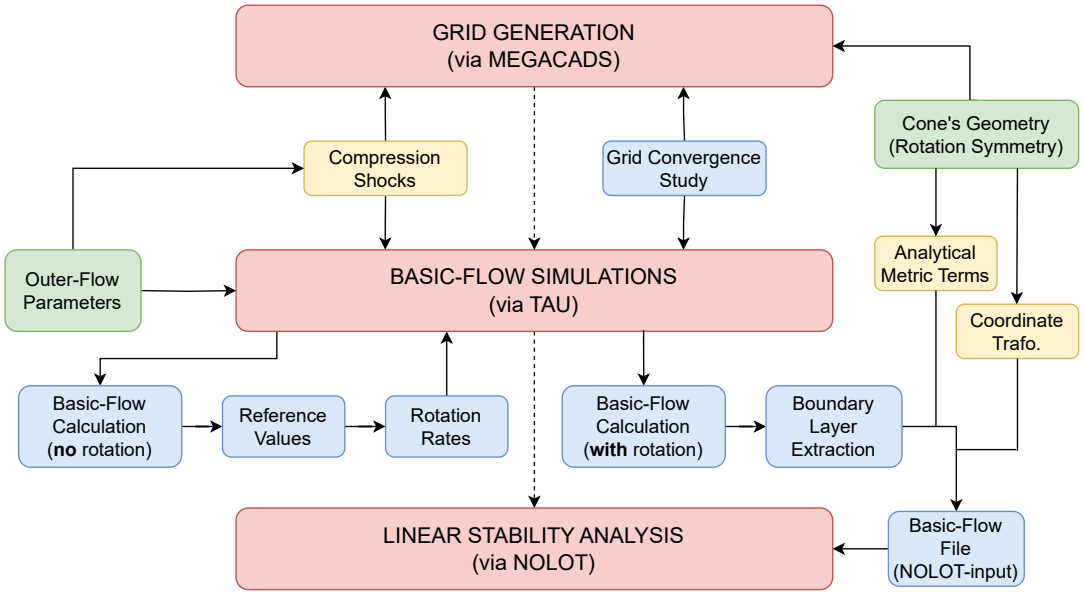

Figure 4.1.: Scheme describing the process for basic-flow simulations in order to perform stability analysis: Main steps are coloured red. Green items describe external parameters, which determine attributes (yellow) important for the grid or the NOLOT-input file. The intermediate steps are coloured blue.

4.1. Flow-Field Solver TAU

As preceding knowledge about the flow field, e.g. about the shock wave position, is of importance to create grids of high quality (cf. section 4.2.1), this chapter starts with an introduction of the flow-field solver TAU, which is developed and used at the DLR.

In the TAU-Code, a variety of different flow-discretization schemes and turbulence models are implemented [10]. Generally, TAU solves the Reynolds-averaged Navier-Stokes Equations (RANS eq.) describing the mean flow, in which random fluctuations - interpreted as part of turbulence - are averaged out of the equations. [11, pp. 395 ff.] But note that the laminar basic flow is of interest and therefore computed only. The mean-flow is evaluated for each finite volume, set externally based on the given grid of the considered setup. Therefore, the RANS equations in conservative form are spatially and temporally discretized using finite-difference quotients to approximate the derivatives, resulting in a difference equation. For more information on this method, see [11] and [13].

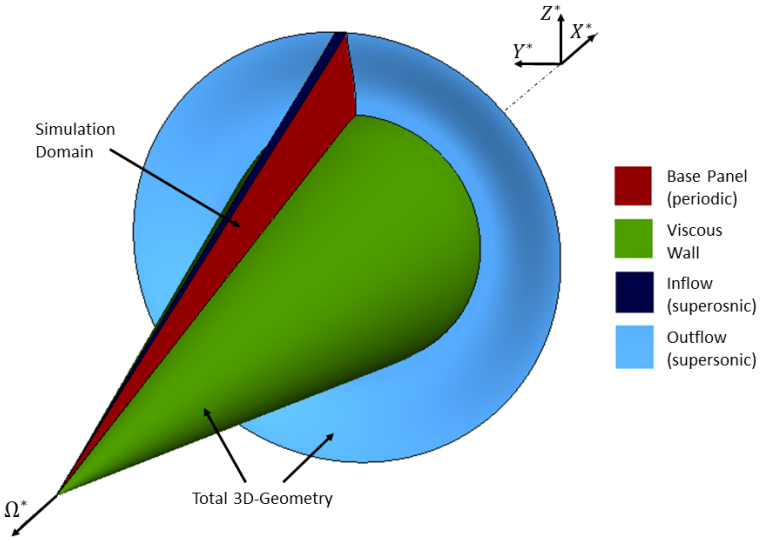

Figure 4.2.: Simulation domain cut out of the three-dimensional grid: Due to the rotational symmetry, only a segment needs to be considered, which leads to new boundaries in circumferential direction (periodic base panels, red). The viscous-wall boundary condition (green) is set for the cone's wall.

An implicit Euler scheme (cf. [11], p. 158) is used for the temporal discretization and the corresponding timestep size is specified by the CFL-number [6], which takes the smallest spatial length in the grid as a reference. Further, in this work, the TAU-implementation of the so called AUSMDV scheme (Advection Upstream Splitting Method Combining Difference and Vector Splitting) is used, which computes the mass flux between adjacent volumes to determine the thermo- and fluid-dynamical quantities of one volume based on its neighbouring volumes. This upwind scheme has originally been published in [47] and is reported to improve computations with included shock waves [10].

As boundary conditions, five specific implementations in TAU are of importance when a cone is simulated with super- or hypersonic axial oncoming flow (cf. Figures 4.2 and 4.3): The supersonic in- and outflow (dark and light blue), the viscous wall (green) and the periodic base panels (red) due to the rotational symmetry. The supersonic in- and outflow work similar to the farfield boundary included in TAU: Generally, the flow-field data at the farfield's boundaries are determined by the oncoming flow, which is set, e.g. with the free-stream Mach number M_∞ or the free-stream pressure p_∞. These reference values are separately dealt with in section 4.1.2.

In TAU, points inside the grid's domain are used to determine the fluid-dynamical quantities outside the boundaries of the farfield using the so called AUSM-scheme (Advection Upstream Splitting Method) [27] as discretization. For the supersonic in- and outflow boundaries, this method reduces to the following distinction: If the outer flow is supersonic ($M_\infty > 1$), the inflow's boundary is directly set by the free-stream reference values and the state outside the outflow's boundary equals the state of the corresponding neighbouring volume in the grid's domain.
The cone's surface is treated as a viscous wall. Therefore, the no-slip condition holds such that no relative velocity at the wall is present (cf. [7]) and the wall is treated to only allow laminar flow. Along with this boundary condition, other characteristics of the wall can be specified, as the cone's rotation or the thermodynamic treatment.
The cone's rotational symmetry allows to simulate only a fraction of the respective geometry's total three-dimensional domain, which reduces the computational cost significantly. Therefore, a segment is cut out of the three-dimensional grid, as it is visualised in Figure 4.2, whereas the resulting domain, on which the simulation is performed, is shown in Figure 4.3. Note that the perspective in Figure 4.3 is skewed and that the same colour-scheme is used as in Figure 4.2 for the respective boundary conditions (only in translucent form). For the resulting segment's base panels in θ-direction (red area in Figures 4.2, 4.3), periodic boundary conditions are applied, so the flow field can be expanded to three dimensions. However, the geometric parameters of this segment have a major impact on the simulation's quality and computation cost and are therefore discussed in more detail in the next section.

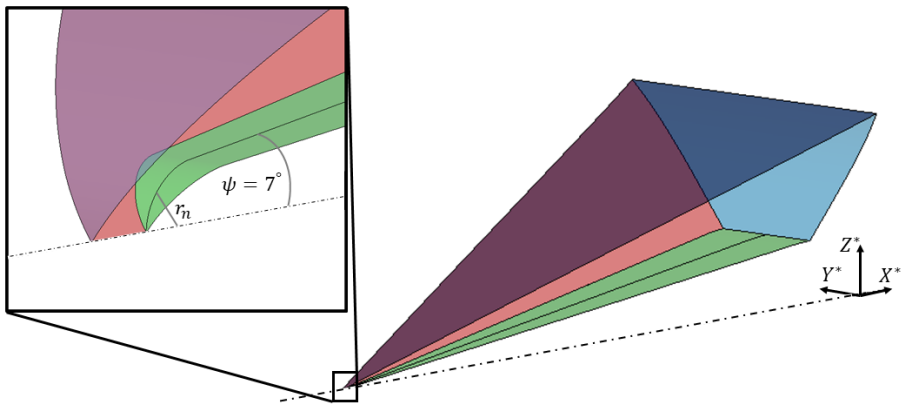

Figure 4.3.: Close-up of the extracted segment as a simulation domain: The same colour scheme as in Figure 4.2 is used.

4.1.1. Angle of Rotation and Base Panels

As stated above, the cone's rotational symmetry can be taken advantage of to only compute the flow field in a fraction of the total three-dimensional domain. Therefore, only a segment is considered (cf. Figure 4.3), which is described by two properties: The number of base panels N_p, in which the segment is divided (representing the amount of grid points GP_θ in circumferential direction with $\mathrm{GP}_\theta = N_p - 1$), and the wedge's apex angle, in the following referred to as rotation angle ϵ_r to avoid confusion with the cone's half-opening angle ψ. Both properties affect the simulation's quality and computational cost: Numerically, the geometry of a cone can only be approximated and the level of agreement is determined by the number of base panels and the rotation angle. However, the more base panels are included, the more grid points have to be considered, increasing the computation cost. Further, small rotation angles have been found to increase the computation time as well.

Extensive studies have been performed, comparing the basic flow results for different ϵ_r and base panel amounts N_p. Without visualisation, comparing the flow field around a non-rotating cone with $\psi = 7°$ for $\epsilon_r = 1^\circ$ with the solution for $\epsilon_r = 3^\circ$, only a negligible loss of quality has been observed; however, the computation time for a converged solution decreases by a factor of about 6.

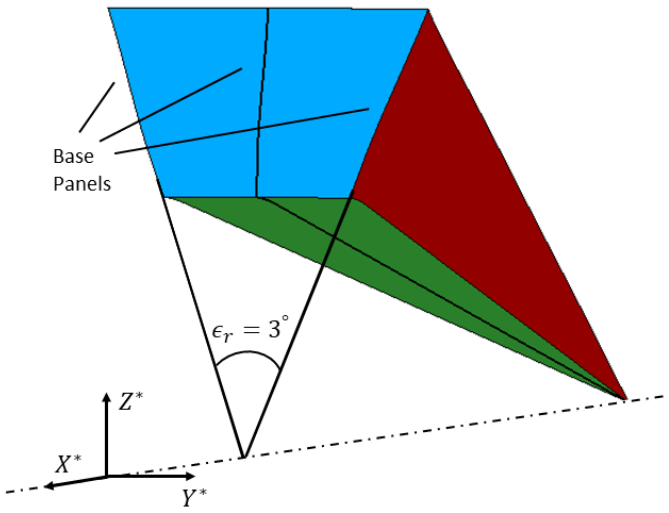

Figure 4.4.: Close-up of the simulation domain with respect to the outflow boundary condition: The same colour scheme as in Figure 4.2 is used. An angle of rotation of $\epsilon_r = 3°$ and the number of base panels $N_p = 3$ is chosen for the segment.

Further, the quality improves with N_p only taking odd numbers, because with the wedge being centered in the x-z-plane, a base panel is located at $\theta = 0$ (cf. Figure 4.3). This improves the boundary-layer extraction process because $\theta = 0$ depicts the simplest extraction position, and the flow-field data do not need to be interpolated compared to even N_p.
As a results, $\epsilon_r = 3°$ has been chosen for this work along with a base panel amount of $N_p = 3$. Hence, if expanded to three dimensions, the geometry's base contour consists of 240 edges. The resulting segment is visualised in Figure 4.4.

4.1.2. Free-Stream Parameters for Oncoming Axial Flow

In TAU, the oncoming axial flow is externally set using reference parameters, which determine the free-stream's thermo- and fluid-dynamical quantities like the Mach number, pressure, temperature or density. Two different speed regimes are considered in this work: Supersonic ($1 < M_\infty = 3.214 < 5$) as well as hypersonic ($5 < M_\infty = 6.1$) flow.
The supersonic flow over a rotating cone has been examined in the work of Song & Dong [39], in which linear stability analysis has been performed on the solutions obtained from the boundary-layer equations for cones with a half-opening angle of $\psi = 7°$ rotating with different intensities. The authors additionally validated the basic flows with results of Navier-Stokes simulations, using free-stream parameters to match the properties at the boundary-layer edge. In order to ensure comparability, these free-stream parameters are adopted in this work for the supersonic flow.
For the hypersonic flow, the free-stream velocity of Oddo et al. [31] is used; however, the farfield's temperature is kept constant compared to the supersonic case. Examining the influence of the free-stream temperature on the instabilities of the rotating cone could be of interest for future studies.

Both sets of free-stream parameters are listed in Table 4.1 and hold for each half-opening angle ψ in the corresponding speed regime. The viscosity is computed with the Sutherland law [41]. Further, the wall's temperature is set constant at $T^*_\mathrm{W} = 300\mathrm{K}$ throughout the simulation (cf. [39]), which, combined with the free-stream temperature, matches experimental conditions. The chosen wall temperature is expected to have different effects on the boundary layer for the super- and the hypersonic speed regime respectively. For a Mach number of $\mathrm{M}_\infty = 3.214$, a wall temperature of $T^*_\mathrm{W} = 300\mathrm{K}$ has a heating effect, while for $\mathrm{M}_\infty = 6.1$ the wall cools

Table 4.1.: Free-stream parameters for the flow-field simulation.

Quantity	Abbrev.	Supersonic M3-case	Hypersonic M6-case
Mach number	M_∞	3.214	6.1
Unit Reynolds Number [1/m]	$\mathrm{Re}_{\infty,\mathrm{unit}}$	5648600.0	10720740.5
(Axial) Velocity [m/s]	U^*_∞	447.64	849.61
Temperature [K]	T^*_∞	48.28	
Pressure [Pa]	p^*_∞	883.85	
Density [10^{-2} kg/m^3]	ρ^*_∞	6.379	
Heat Capacity Ratio	γ	1.4	
Prandtl Number	Pr	0.72	

down the boundary layer. This is estimated by calculating the laminar adiabatic wall temperature as described in Ref. [35]. It could be of interest for future work to vary the wall temperature in order to gain a more detailed knowledge about the influence of the cooling and heating effects of the wall on the instabilities considered in chapter 5.

From here on, the speed regimes are referred to as M3(-case) and M6(-case) respectively, whereas the notation 'setup' distinguishes between each choice of inflow and half-opening angle. For example, the 7°-M3-cone refers to the setup of a flow with the free-stream Mach-number of $M_\infty = 3.214$ (M3-case) over a cone with half-opening angle $\psi = 7°$.

The comparison to the literature of the resulting basic flow is given in section 4.3.

4.2. Grid Development Process and Simulation Strategy

This section presents the grid development process, which is divided into two important steps: The shock wave's position for each half-opening angle of the respective M-case is determined and a grid-convergence study is performed, to ensure the quality of the corresponding simulation.

Further, a brief description of the TAU-simulation strategy and the consequent boundary-layer extraction is given in this section.

4.2.1. Shock Wave and Importance for the Grid

The shock wave is a physical phenomenon, which, inter alia, arises in front of an object travelling with supersonic speed [9, p. 292] and has already been reported and analysed for cones in the works of Busemann [4] and Grozdovskii [18].
A shock wave is characterised by its quasi-discontinuity, in which fluid- and thermodynamical quantities adjust abruptly to the disturbance caused by the obstacle [9, p. 291]. For additional information, Ref. [9] contains a more extensive description of this phenomenon. If numerical simulations of supersonic flows are performed, the grid domain that covers the shock wave and the area of quasi-discontinuity must be resolved in more detail in order to accurately describe the change of states. Otherwise, the flow field downstream of the shock wave could be falsified. Therefore, computations on grids with lower accuracy have been performed for each considered setup to consecutively determine the shock waves' positions. The resulting zone of the grid around the shock-wave position, which needs to be resolved with higher accuracy, is shown in Figure 4.5(a) as the red- and orange-coloured regions.

4.2.2. Number of Grid Points and Grid Convergence

The grid domain can be divided into different zones each affecting the simulation's quality differently. The different zones are shown in Figure 4.5(a) for the wall-normal direction and in Figure 4.5(b) for the streamwise direction. The number of grid points in streamwise direction determines the resolution of the cone's nose (coloured as dark red) and the cone's surface (coloured as light orange), whereas in wall-normal direction, the shock wave position (coloured as red) and a layer near the wall (coloured as yellow) must be well-resolved. The near-wall layer is of height $\approx 6 \cdot 10^{-3}\,\mathrm{m}$ and is checked to contain the boundary layers of the respective setups. Although the grid-convergence study is performed for every zone in Figure 4.5, this section only presents the method for the near-wall layer in wall-normal direction and the cone's surface in streamwise direction, as these are the zones with the most amount of grid points. Nevertheless, the sufficient amounts of grid points for the shock-wave region and the zone defined by the cone's nose as well as for the intermediate zones of Figure 4.5 are stated at the end of this section to present the final grid. This section refers to the number of grid points in the near-wall layer as GP_l and to the number of grid points in streamwise direction on the cone's surface as GP_s.

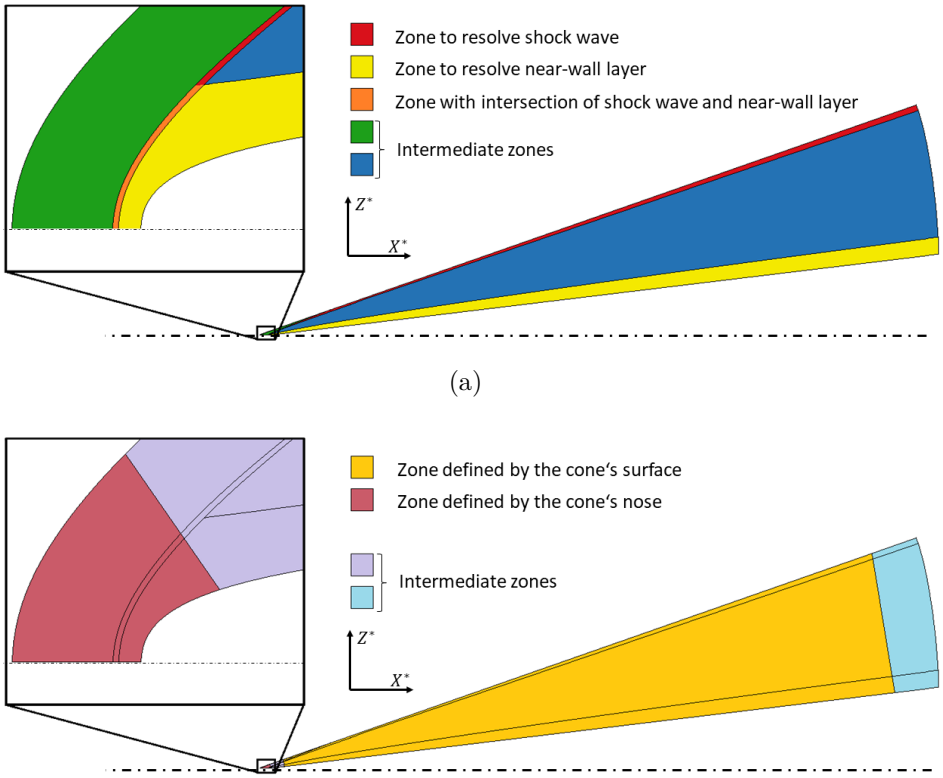

Figure 4.5.: Different zones to determine the grid-point distribution in wall-normal direction (a) and in streamwise direction (b) in the course of the grid-convergence study.

As linear stability theory is performed in chapter 5 for the laminar boundary layers of the presented setups and the quality of linear-stability results highly correlates with the basic-flow quality, the grid-convergence study uses N-factor curves (cf. section 2.4) because they provide a global measure of the disturbance growth [29]. Further, individual growth-rate curves with respect to the location on the cone are compared. A sufficient number of respective grid points is reached, if the N-factor or growth-rate curves do not change with a further grid-point increase. For the two speed regimes in 4.1.2, this study is performed individually, using the 2^{nd}-Mode representatively for the M6- and the 1^{st}-Mode for the M3-case. Rotation is not considered, as the number of grid points for non-rotational setups is assumed to be sufficient for the rotational setups as well. The convergence study focuses on the 7°-cone and the results are adopted for the other half-opening angles ($\psi = 5°, 10°, 15°$).

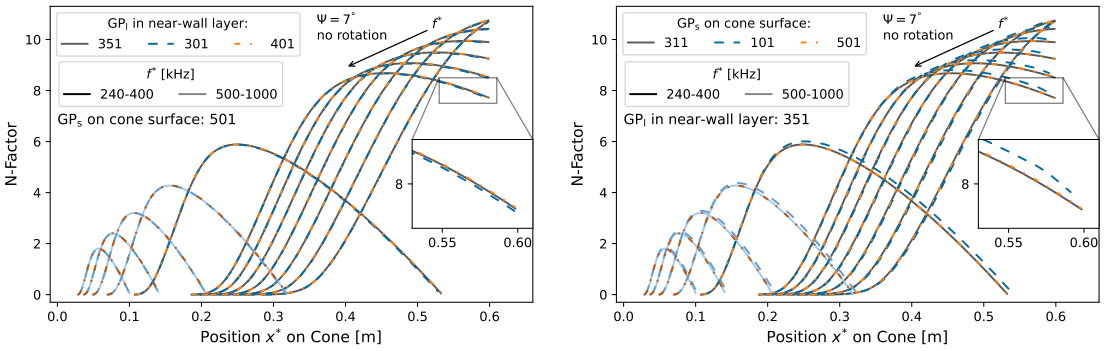

(a) (b)

Figure 4.6.: N-factor curves for the M6-case's 2nd-Mode for different frequencies to determine the grid convergence by varying the number of points in the near-wall layer (a) and on the cone's wall (b).

Representatively for the M6-case, Figures 4.6 (a) and (b) plot the 2nd-Mode's N-factors for different frequencies against the position x^* on the cone. In Figure 4.6(a), the streamwise grid point number GP$_s$ of the cone's surface is kept constant, as the wall-normal resolution in the near-wall layer is varied. In 4.6(b), it is the other way around. The grid-point number of the zone, that is not varied, is chosen sufficiently high. For the 2nd-Mode, lower frequencies are more important in this work because they represent the frequency domain for which the mode is unstable at the position of interest in chapter 5 (i.e. $x^* = 0.4\,\mathrm{m}$).
As the N-factor curves in Figure 4.6(a) for GP$_l$ = 351 and GP$_l$ = 401 are in good agreement, GP$_l$ = 351 is chosen to resolve the near-wall layer in wall-normal direction. In Figure 4.6(b), the curves with a grid-point amount of GP$_s$ = 311 and GP$_s$ = 501 are on top of each other, such that the number of grid points in streamwise direction on the cone's surface is set to GP$_s$ = 311. Note that the distance between the different grid points increases with the position on the cone in order to match the grid-volume size at both the cone's nose and the cone's base.

Figure 4.7 summarises the same approach for the M3-case's 1st-Mode, however only the grid-point number GP$_l$ in the near-wall layer is varied, as the streamwise resolution of the cone's surface is adopted from the M6-case. Further, only frequencies between 4-20 kHz are considered. For higher frequencies, the 1st-Mode is already unstable at positions near the cone's nose, which corresponds to the orange-coloured zone in Figure 4.5. N-factor curves originating in that area can not be considered,

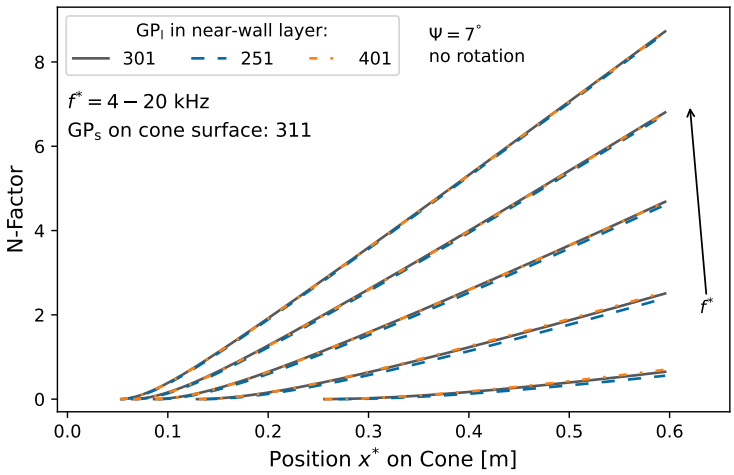

Figure 4.7.: N-factor curves for the M3-case's 1$^{\text{st}}$-Mode for different frequencies between $f^* = 4 - 20\,\text{kHz}$ to determine the grid convergence depending on the number of points in the near-wall layer.

which is is due to problems in the extraction of the boundary-layer's basic flow. In that domain, the shock wave intersects with the near-wall layer, which causes problems with the boundary-layer edge detection criterion (cf. section 4.2.3). To resolve the issue, a shock-wave adapted boundary-layer edge criterion is needed in order to neglect the shock wave in the basic flow. However, this problem does not affect the stability analysis results presented in chapter 5, as they focus on the position $x^* = 0.4\,\text{m}$. Therefore, this work continues without adapting the boundary-layer edge criterion and instead of considering N-factor curves in the grid-convergence study of the M3-case, individual growth-rate curves are analysed.

Figure 4.7 shows that for low frequencies, grid convergence of the M3-case is already reached for a grid-point number of $\text{GP}_l = 301$ in the near-wall layer's wall-normal direction. Comparing the individual growth-rate curves along the cone without considering the apex, 301 grid points in wall-normal direction have been found to be sufficient for higher frequencies as well, because the maximal difference in the growth rate curves of $\text{GP}_{\text{bl}} = 301$ and $\text{GP}_{\text{bl}} = 351$ is 0.8%.

The resulting grid for the M3-case is visualised in Figure 4.8. In streamwise direction, the grid consists of 550 grid points, whereas the nose is resolved with 113 points and the cone's surface with 311 points. The additional 126 points are added in the intermediate zones of Figure 4.5(b). In wall-normal direction, the grid consists of 484 grid points, from which 301 points are in the near-wall layer, 21 points resolve the

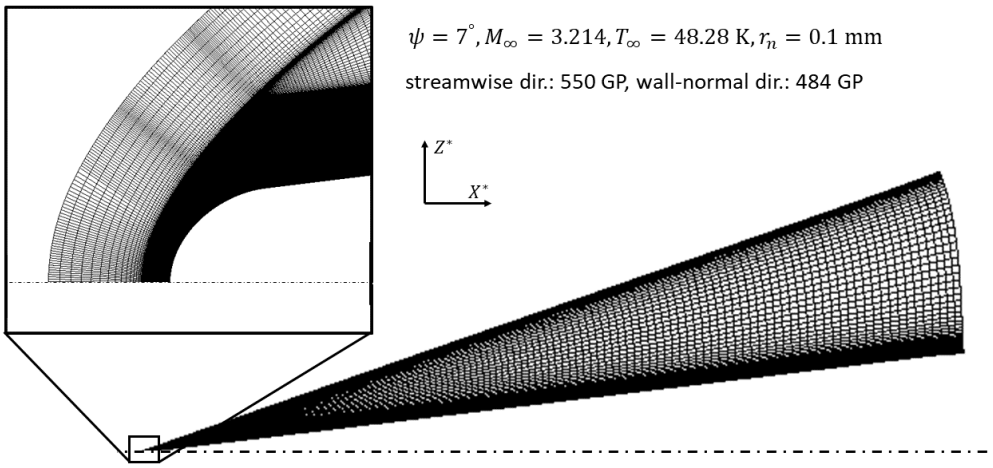

Figure 4.8.: Final grid of the 7°-M3-case: The grid consists of 550 grid points in streamwise direction and 484 grid points in wall-normal direction. The detailed distribution is given in section 4.2.2.

shock wave and 161 are added in the intermediate zones of Figure 4.5(a). The grid for the M6-case only differs by 50 additional grid points in the wall-normal direction, as shown above. These grid parameters are adopted for the different half-opening angles respectively.

4.2.3. Time Convergence, Simulation Strategy and Boundary-Layer Extraction

In addition to the grid convergence presented in section 4.2.2, there is also the time convergence of the simulation. Therefore, TAU computes a residual vector for each control volume V_j around the grid point P_j as

$$\mathbf{R}\,(j) = \frac{1}{V\,(j)}\mathbf{Q}^F\,(j)\ .$$

$\mathbf{Q}^F(j)$ represents the fluxes through the boundaries of the control volume V_j and the components of the residual vector are given by

$$\mathbf{R}\,(j) = \left(res^n_{\rho}(j), res^n_{\rho u_1}(j), res^n_{\rho u_2}(j), res^n_{\rho u_3}(j), res^n_{\rho E}(j)\right)^{tr}\ .$$

The superscript n denotes the current iteration step and j runs between 1 and the overall number of grid points N. For more information about the notation, see [10]. In this work, the residual-vector's first component is used to define the convergence criterion. Thus, the root mean square of the density residual defines the global residual as

$$||res_\rho^n||_\infty = \sqrt{\sum_{j=1}^{N} \frac{\left(res_\rho^n(j)\right)^2}{N}}\,.$$

The convergence criterion is given by

$$||res_\rho^n||_\infty \overset{!}{<} 10^{-8}\,. \tag{4.1}$$

At this criterion, agreement between the basic-flow profiles of the boundary layer at different iteration steps has been reached as well as agreement between stability analysis results, such as individual growth rate curves or neutral curves in the frequency-wavefront-count domain.
Different rotation rates are considered in this work (cf. section 4.3). With the increase of the rotation intensity, the previously computed flow-field of the next lower rotation rate serves as the initial guess for the new computation, which enhances the simulation's convergence and reduces the computational cost.

In order to perform local stability analysis with the corrected NOLOT-extension code, boundary-layer profiles from the laminar flow-field solution are extracted to generate NOLOT-input file containing the basic flow.
In this work, the boundary-layer edge detection criterion is defined as

$$U_e^*\Big|_{x^*=x_s^*} \equiv 0.9988 \cdot \max_{z^*} \left(|\mathbf{U}^*\left(x_s^*, z^*\right)|\right)\,, \quad z^* \in [0, h_{\mathrm{NW}}^*] \tag{4.2}$$

for each position x_s^* respectively, with $|\mathbf{U}^*|$ representing the absolute value of the dimensional velocity vector. Note that h_{NW}^* describes the height of the near-wall layer marked in Figure 4.5(a). The detection criterion is applied to this restricted domain to obtain the basic-flow data of the boundary layer only. Otherwise, the shock wave would be included, as it is the case for the orange-coloured domain in Figure 4.5(a), which caused the problems with the computation of N-factor curves originating in that zone (cf. section 4.2.2).

The metric terms and the local radii in the NOLOT-input file are computed analytically, as presented in section 2.1. Further, because TAU computes the flow field in the non-rotating Cartesian coordinate system, the velocities are transformed into the cone's rotational coordinate system, for which the velocity of the cone's wall has to be subtracted from the circumferential velocity component. This method represents an approximation of the general transformation into the rotational frame of reference, as it is assumed that $\delta^* \ll x^* \sin(\psi)$. However, this approximation is used in this work to ensure comparability with the results of Song & Dong [39] and leads to $v(z=0) = 0$ and $v(z \to \infty) < 0$ as shown in section 4.3.

4.3. Rotation Rates and Basic-Flow Results

4.3.1. Definition of Rotation Rates and Reference Values

The rotational velocities Ω^* are determined equivalently to the work of Song & Dong [39] via the definition of a general rotation rate, which weighs the rotational speed of the cone's wall against the external flow such that

$$\bar{\Omega} = \frac{\Omega^* x^* \sin(\psi)}{U_e^*} \,. \tag{4.3}$$

This definition ensures comparability between the different considered setups and will therefore be used throughout this work as description for the rotational intensity. The position of interest, $x^* = 0.4\,\mathrm{m}$, is chosen analogously to Song & Dong [39]. The boundary-layer edge velocity u_e^* is determined using the non-rotational simulation for each speed regime of the oncoming flow (cf. section 4.1.2) and half-opening angle respectively. The non-rotational simulations also provide the reference velocities for the corresponding rotational setups throughout this work because with onset of rotation, this quantity does not change significantly (cf. Figure D.1 in Appendix D). This also holds for the Blasius length $\delta^* = \sqrt{\frac{x^* \mu^*}{\rho_e^* U_e^*}}$, which provides the reference length.

4.3.2. Comparison of the Basic Flow to Literature

The boundary-layer edge values for the thermo- and fluiddynamical quantities of the non-rotational setup are listed in Table 4.2. Unfortunately, for the 7°-M3-cone,

Table 4.2.: Boundary-layer edge and reference values for each setup.

at $x^* = 0.4\,\mathrm{m}$, $\bar{\Omega} = 0$							
Case	ψ	M_e	u_e^* [m/s]	T_e^* [K]	p_e^* [Pa]	δ^* [mm]	$\mathrm{Re}_{\mathrm{blasius}}$
M3	7°	3.0	437.8	52.9	1193.3	0.20	1923.2
	→ [39]	3	433.8	52	N/A	0.2	2000
	5°	3.1	441.5	51.7	1064.8	2.11	1850.9
	10°	2.9	431.1	55.5	1436.8	1.89	2039.3
	15°	2.7	417.6	61.2	1977.5	1.71	2225.2
M6	5°	5.6	841.3	56.1	1392.2	1.35	2716.2
	7°	5.4	836.5	59.4	1777.3	1.23	2965.2
	10°	5.0	827.4	66.8	2547.7	1.09	3320.7
	15°	4.4	807.1	83.3	4361.2	0.93	3810.5
ref. val.			$\equiv u_{\mathrm{ref}}^*$	$\equiv T_{\mathrm{ref}}^*$		$\equiv l_{\mathrm{ref}}^*$	

the free-stream reference values presented in section 4.1.2 do not lead to perfect agreement with the flow field presented in Song & Dong [39].

This is also shown in Figures 4.9 (a)-(d), in which boundary-layer profiles are visualised using u_e^*, T_e^* and δ^* from Table 4.2 for non-dimensionalisation, such that $\mathbf{u} = \mathbf{u}^*/u_e^*$, $T = T^*/T_e^*$ and $z = z^*/\delta^*$. Because this work's reference values differ compared to the work of Song & Dong [39], the boundary-layer profiles of [39] are renormalised with the reference values of Table 4.2 to ensure comparability.

The qualitative form for each curve u, v, w and T is reproduced, however it differs quantitatively compared to the results in the work of Song & Dong [39]. Especially, the temperature at the boundary-layer edge does not match, which influences the viscosity and therefore the Blasius Reynolds-number $\mathrm{Re}_{\mathrm{blasius}} = \rho_e^* u_e^* \delta^* / \mu_e^*$ as well as the boundary-layer edge velocity, as it is computed via $M = u_e^*/\sqrt{\gamma T_e^* \mathrm{R}_M^*}$, with R_M^* defined as in section 2.2. The reasons for the differences are speculative. The most obvious cause could be the different nose radii. In this work, the nose radius is chosen as $r_N = 0.1\,\mathrm{mm}$, whereas the cone's tip radius in Song & Dong [39] is one order of magnitude smaller. The resulting difference in the flow around the apex could transfer up to the position $x^* = 0.4\,\mathrm{m}$. However, in the work of Song & Dong [39], it has been reported based on the work of Sivasubramanian & Fasel [38], that the nose radius does not affect the boundary-layer profiles and the linear stability results at distances greater than $2000 \cdot r_N$ from the cone's tip. Unfortunately, a nose radius of $r_n = 0.01\,\mathrm{mm}$ led to problems in the grid development process, such that the influence of the cone's tip has to be revisited in future work. Nonetheless, this

work utilises the results computed with the TAU code, although the differences are expected to transfer to the rotational setups as well.

Using the boundary-layer edge values presented in Table 4.2 and the definition of the rotation rates $\bar{\Omega}$ in Equation 4.3, the dimensional angular velocity for the respective setup and rotation rate can be computed and is listed in Tables D.1 and D.2 of Appendix D.
For $\bar{\Omega} = 0.3$ and $\bar{\Omega} = 0.75$, a comparison of the boundary-layer profiles to the profiles computed by Song & Dong [39] is given in Figures 4.9 (a)-(d). As mentioned, the boundary-layer profiles presented in the work of Song & Dong [39]) are renormalised in terms of this work's reference values. The observed discrepancies for the non-rotational 7°-M3-cone transfer to the rotational setups as expected. The differences in the boundary-layer edge values lead to small differences in the rotational velocities,

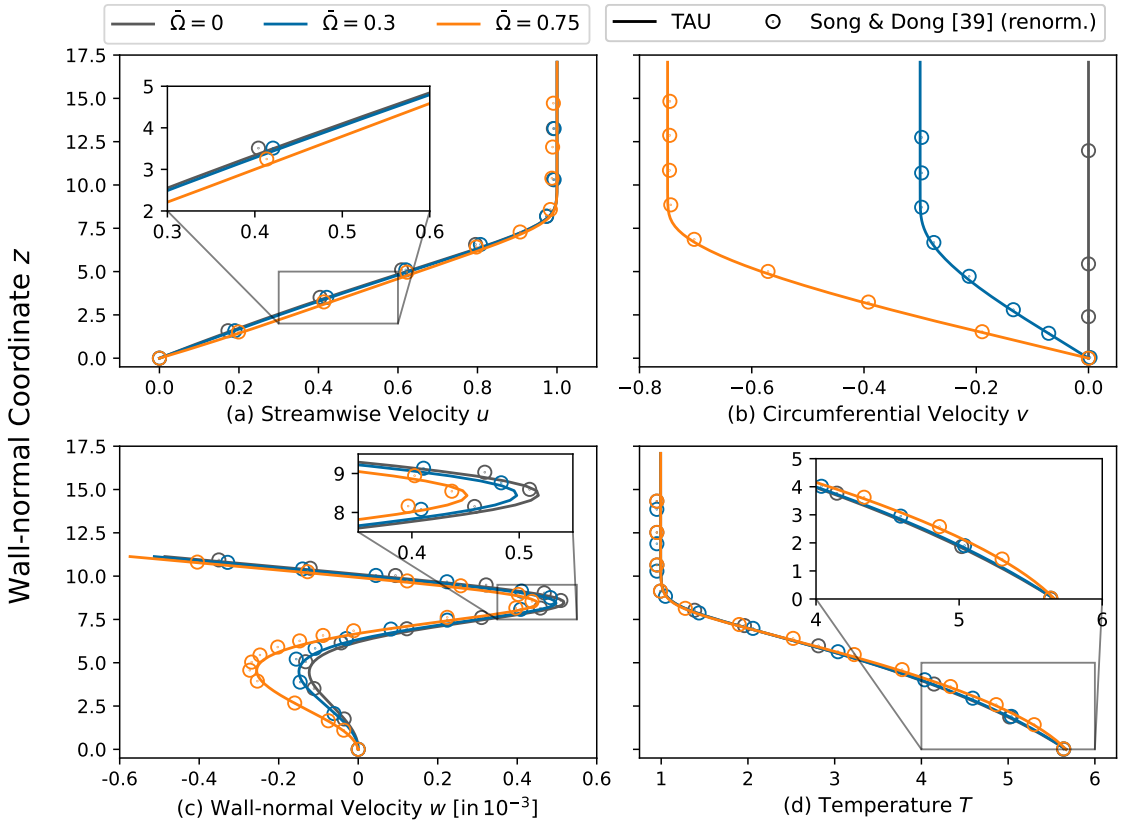

Figure 4.9.: Boundary-layer profiles u (a), v (b), w (c) and T (d) for the 7°-M3-case at $x^* = 0.4\,\mathrm{m}$ varying the rotation rate: The rotation rates $\bar{\Omega} = 0$ (black), $\bar{\Omega} = 0.3$ (blue) and $\bar{\Omega} = 0.75$ (orange) are compared to the literature [39] (circles).

which explains the deviation to the literature's curve ([39], circles) compared to the TAU solution for $\bar{\Omega} = 0.75$ in the u- and the v-profile. Because the rotation does not influence the temperature far away from the cone, the boundary-layer edge temperature does not change with the onset of rotation and still depicts the same shift compared to Ref. [39]. The wall-normal velocity component does not match quantitatively with the results of Ref. [39] as well. However, these differences are negligible as this velocity component is not considered in the stability analysis (cf. section 2.2). Otherwise, the profiles are in good agreement with the literature [39].

As the cross-flow velocity component is expected to be a driving mechanism for the Crossflow- and Centrifugal-Instability (cf. section 1.2), a transformation into a streamline coordinate system is performed to predict the influence of the rotation intensity on both modes and the difference to the results of Song & Dong. The velocity along the streamline is referred to as U_p, whereas U_c defines the perpendicular component. The transformation is similar to Equation 3.1 a.) and b.) in the work of Song & Dong [39] and is defined as

$$\begin{aligned} U_p = u\cos\left(\Phi_e\right) + v\sin\left(\Phi_e\right) \ , \quad U_c = -u\sin\left(\Phi_e\right) + v\cos\left(\Phi_e\right) \\ \text{with} \quad \Phi_e = \tan^{-1}\left(v_e\right) \ . \end{aligned} \tag{4.4}$$

The resulting curves are shown for the 7°-M3-case for the rotation rates $\bar{\Omega} = 0.3$ and $\bar{\Omega} = 0.75$, with the circles again referring to the renormalised results of Ref. [39]. The velocity component U_p along the streamline is assumed to mainly influence the 1^{st}- and the 2^{nd}-Mode, as this velocity component is dominated by the external axial inflow and these instabilities are not expected to be driven by the rotation. Hence, the small qualitative differences observed in the section up to $z = 8$ of Figure 4.10 (a) could lead to small differences in the stability results for the mentioned instabilities compared to the literature [39]. For the velocity component U_c in Figure 4.10 (b), differences are observed between this work and the results of Song & Dong [39] in the maximum's position and value as well as in the position of the turning point leading to the asymptote towards zero for high wall distances. These deviations could cause different stability analysis results for the Crossflow- and Centrifugal-Instability and increase with the rotation intensity, as the maximum value does not match the curve of Song & Dong for $\bar{\Omega} = 0.75$. Further, the asymptote for $\bar{\Omega} = 0.75$ is slightly shifted towards positive velocities, which also leads to a mismatch in the inflection point compared to the curve of Song & Dong [39].

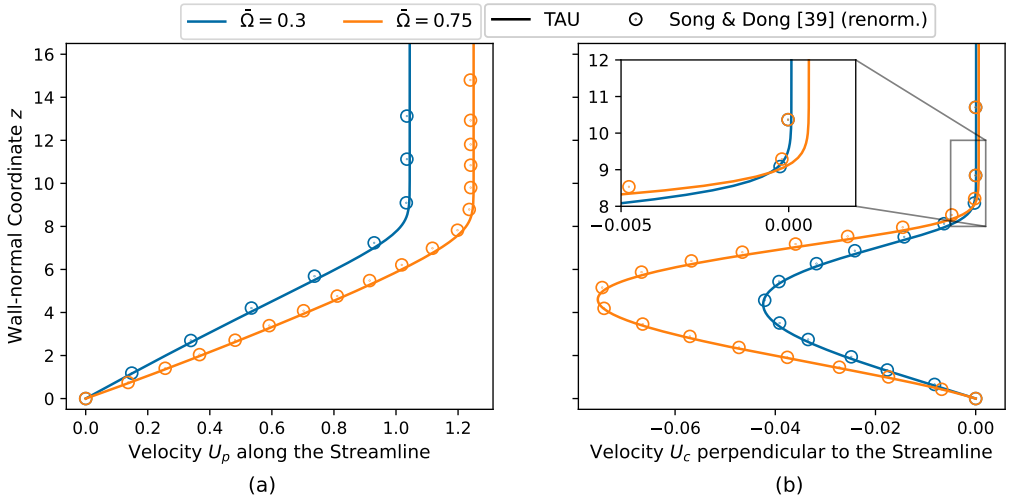

Figure 4.10.: Profiles of the velocity components U_p (a) along and U_c (b) perpendicular to the streamline for the 7°-M3-case at $x^* = 0.4\,\mathrm{m}$: The transformation is given in Equation 4.4. The rotation rates $\bar{\Omega} = 0.3$ (blue) and $\bar{\Omega} = 0.75$ are compared to the literature [39] (circles).

Due to these differences in the boundary-layer profiles, small discrepancies between the stability analysis results obtained with the corrected NOLOT-extension code and the results presented in Song & Dong [39] for the 7°-M3-cone are expected. However, the differences are assumed to be of quantitative nature, such that the qualitative behaviour, e.g. with the increase of the rotation rate, is not affected.

4.3.3. Influence of Half-Opening Angle and Free-Stream Velocity on Basic Flow

This section presents the basic flow in terms of boundary-layer profiles and compares the influence of the half-opening angle and the speed of the oncoming axial flow. Therefore, the boundary-layer profiles are plotted in dimensional form. This ensures comparability, as the non-dimensional profiles could lead to false conclusion due to the different reference values of the respective cone setups; especially because the reference length $l^*_{ref} = \delta^*$ (Blasius length) does not necessarily scale with the boundary-layer thickness. This method is also applied for the comparison of linear stability analysis results if the half-opening angle or the speed regime is varied.

Figure 4.11, visualises the boundary-layer profiles for the velocity components ((a)-(c)) as well as for the temperature (d). Three different half-opening angles in the

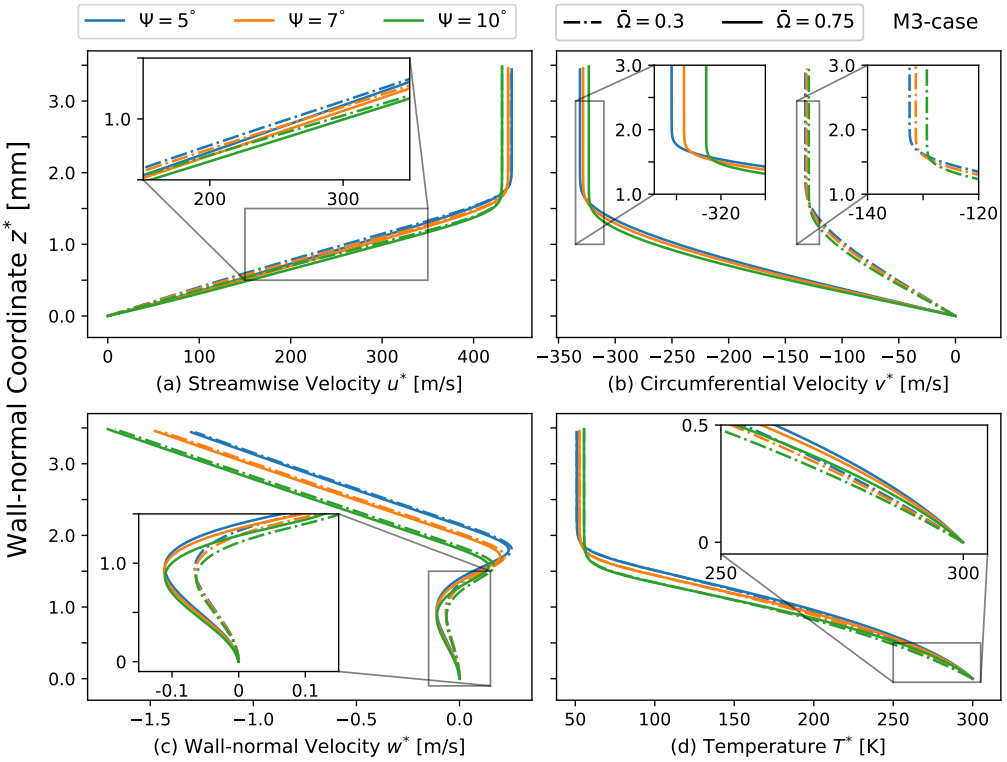

Figure 4.11.: Boundary-layer profiles u (a), v (b), w (c) and T (d) for cones with different half-opening angle ($\psi = 5°, 7°, 10°$) and rotation rates ($\bar{\Omega} = 0.3, 0.75$) for the M3-case at $x^* = 0.4\,\mathrm{m}$.

M3-case's speed regime for two rotation rate $\bar{\Omega} = 0.3$ and $\bar{\Omega} = 0.75$ are considered. Figure 4.11 (a) shows the different boundary-layer edge velocities of the considered setups, which decrease with broader cones (cf. Table 4.2). However near the wall ($z^* < 1.5\,\mathrm{mm}$), the slope of the u^*-velocity component with respect to the wall-normal coordinate ($\frac{\mathrm{d}u^*}{\mathrm{d}z^*}$) increases with the half-opening angle. As the 1^{st}- and 2^{nd}-Mode are expected to be driven by the velocity component along the streamline, in which the streamwise velocity component is dominant, the slope's increase in Figure 4.11 (a) could indicate a destabilisation of the respective modes. The same holds for the circumferential component in Figure 4.11 (b) regarding the Crossflow- and Centrifugal-Instabilities, as the slope of the circumferential velocity with respect to the wall-normal coordinate decreases further with the half-opening angle. However, v^* decreases with ψ at the boundary-layer edge, which represents the wall rotation and therefore could stabilise the instabilities. The boundary-layer edge temperature visible in Figure 4.11 (d) increases with ψ. This also holds for the slope, with which the temperature decreases in wall-normal direction ($\frac{\mathrm{d}T^*}{\mathrm{d}z^*}$).

Finally, Figure 4.11 compares boundary-layer profiles between the two speed regimes presented in section 4.1.2. Three setups are considered: Two half-opening angles in hypersonic oncoming flow and the 7°-M3-case for comparison. Further, the respective profiles are shown for the rotation rates $\bar{\Omega} = 0.3$ and $\bar{\Omega} = 0.75$.
Per definition, the boundary-layer edge velocity of the streamwise component increases with the oncoming-flow speed, which leads to the increase of the wall's rotation speed, as it is defined via the reference velocity in Equation 4.3. Otherwise, the same effects of the half-opening angle variation and rotation speed increase are observed as in the M3-case. Most significantly, the temperature near the wall ($z^* = 0\,\text{mm}$ to $z^* \approx 0.5\,\text{mm}$) surpasses the wall-temperature and forms a local maximum, which is a consequence of the cooling effect of the wall on the boundary layer in the M6-case as described in section 4.1.2. The absolute value of this maximum is constant for different half-opening angles, but increases with the rotation intensity.

Additional boundary-layer profiles for each half-opening angle, rotation rate and speed regime are included in Appendix E.

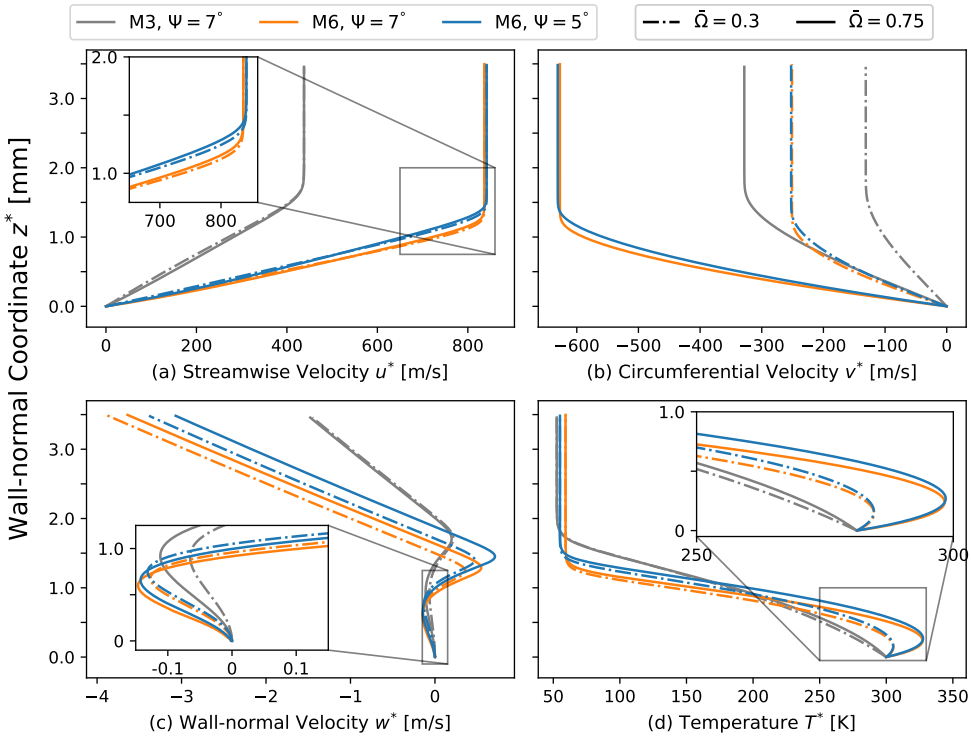

Figure 4.12.: Boundary-layer profiles u (a), v (b), w (c) and T (d) for cones with different half-opening angle ($\psi = 5°, 7°$) and rotation rates ($\bar{\Omega} = 0.3, 0.75$) comparing supersonic and hypersonic oncoming flow at $x^* = 0.4\,\text{m}$.

5. Linear Stability Analysis Results - Rotating Cone in Super- & Hypersonic Oncoming Flow

In this chapter, the results of the linear stability analyses are discussed which have been conducted for the cone's super- and hypersonic laminar boundary layers extracted from the TAU-simulation results as presented in chapter 4. The overall approach is summarised in Figure 5.1: Each instability-type of section 1.2 is investigated separately but with the same general procedure: First, the individual instability type is characterised and the results are compared to the work of Song & Dong [39]. Therefore, the analyses focus on the position of $x^* = 0.4\,\mathrm{m}$ unless it is stated otherwise. Further, the influences of the rotation rate $\bar{\Omega}$, the half-opening angle ψ and the usage of the metric and rotation terms in the stability equations are discussed. Note that differences compared to the literature [39] are expected due to the different basic-flow results; however, these are not expected to influence the qualitative results of the parameter studies. Comparisons of amplitude functions are used to characterise the instabilities and to identify any changes in the currently observed mode. Further, growth-rate curves are compared and analysed, either at specific frequencies or by showing the isosurfaces in the ω-n-space. Note that the metric and rotation terms in the stability equations are used, if not stated otherwise and are referred to as the *default setting* (or *w/all terms* in the Figures). The combination of metric and rotation terms is also referred to as *additional terms*.
The cone with a half-opening angle of $\psi = 7°$ is utilised for comparison with the literature [39] and ψ is only varied for examining its influence on the instability characteristics. Therefore, it is also mentioned individually if any other half-opening angle is considered.

The aim is a general understanding of the instabilities' characteristics and their changes due to rotation. It is also asked how metric and rotation terms affect the modes individually and the modes' behaviour with the half-opening angle and the free-stream Mach number is investigated. Therefore, the growth rates' behaviour is mostly tracked in the following analysis.

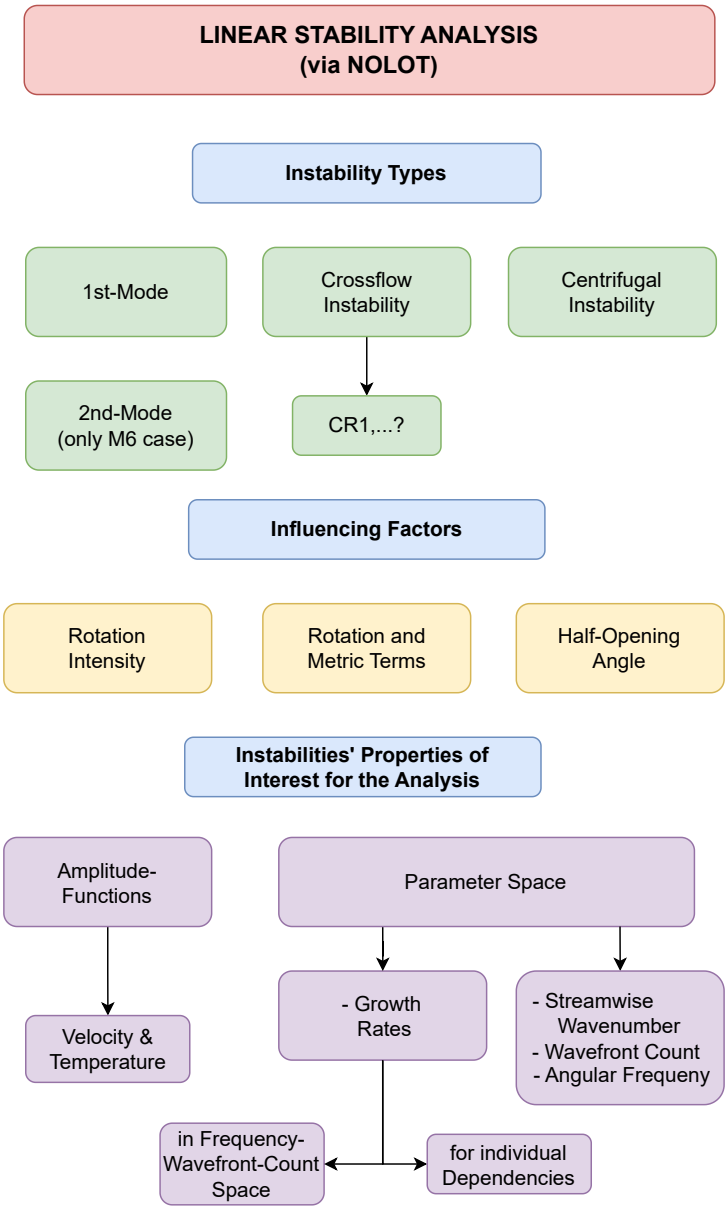

Figure 5.1.: Schematic of the strategy utilised for the linear stability analysis: The instability types (green) are characterised and analysed regarding the influence factors (yellow) using the properties of the instabilities (violet).

5.1. The 1st- and 2nd-Mode

At first, the 1st- and the 2nd-Mode are considered. The 2nd-Mode is stable for the M3-case and therefore only observable for the M6-case (cf. Mack [29]). Hence, this section firstly examines the 1st-Mode for both the M3- and the M6-cases.

5.1.1. The 1st-Mode with Oncoming Flow in the Supersonic Speed Regime (M3-Case)

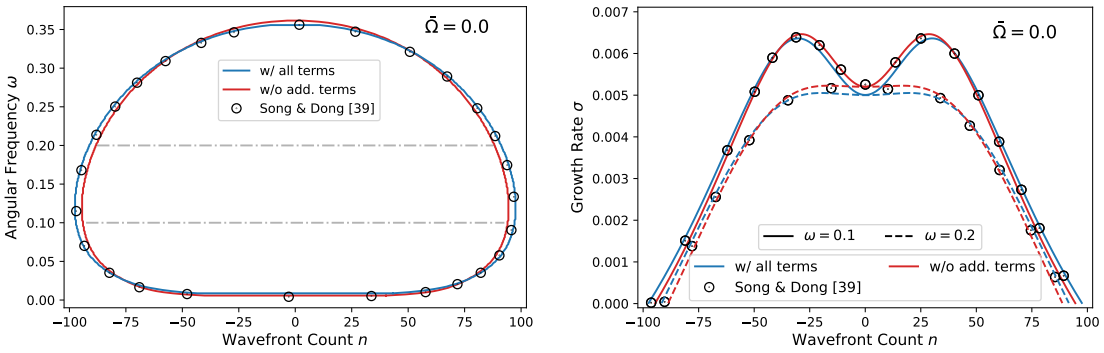

(a) (b)

Figure 5.2.: Comparison of neutral curves (a) and growth rate curves (b) to the literature [39] (circles) with linear stability analysis conducted for the 7°-M3-case with (blue) and without (red) the metric and rotation terms. The dash-dotted lines in (a) represent the frequencies $\omega = 0.1$ and $\omega = 0.2$ considered in (b).

Characterisation without Rotation

First, the non-rotational case of $\bar{\Omega} = 0$ is considered. Figure 5.2(a) compares the respective neutral curves of the 1st-Mode between this work and Song & Dong [39]. For the red curve, metric terms are excluded from the stability equations, whereas the blue curve denotes the neutral curve solution for the default settings. Additionally, Figure 5.2(b) visualises the growth rates' dependency on the wavefront count n at the frequencies marked in Figure 5.2(a) using the same colour-scheme as before. Good agreement with the literature has been reached implying that the stability equations in the work of Song & Dong [39] are similar to the stability equations implemented in the NOLOT-code. The observed small deviations are consequences of

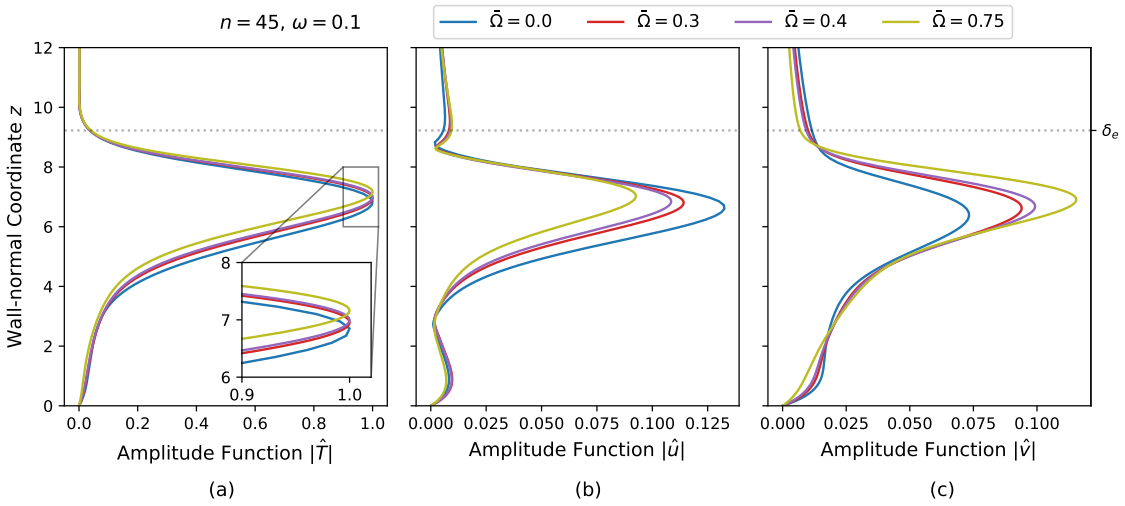

Figure 5.3.: Comparison of the 1st-Mode's amplitude functions $|\hat{T}|$ (a), $|\hat{u}|$ (b) and $|\hat{v}|$ (c) at $n = 45$ and $\omega = 0.1$ for different rotation rates.

the different basic flows (cf. section 4.3). Further, both plots show the symmetrical character of the 1st-Mode without rotation, as it has been observed in the work of Reed & Balakumar [2] or Mack [30]. For example, both maxima in the growth-rate-function for $\omega = 0.1$ appear at the same wavefront counts $\pm n$. However, this is to be expected due to the cone's rotational symmetry.

In this section, a more detailed characterisation of the 1st-Mode is given. Figures 5.3(a) to (c) show the amplitude functions of the streamwise and circumferential velocity $|\hat{u}|$ and $|\hat{v}|$ as well as the temperature $|\hat{T}|$ for different rotation rates. The wall-normal component $|\hat{w}|$ has not been included because of its negligible influence on the instability due to its order of magnitude compared to the other quantities. The plotted amplitude-functions correspond to parameters in the 1st-Mode's most unstable area in the frequency-wavefront-count space and can therefore be interpreted representatively for the whole instability.
Apparently, the temperature is the dominant disturbance amplitude function for the 1st-Mode. The amplitude function $|\hat{T}|$ depicts a single and defined peak and has a generally asymptotic nature towards zero in wall-normal direction. The maximum can therefore be used as a characterisation and lies at $z \approx 0.74\delta_e$ for the 1st-Mode's non-rotational case. Both disturbance velocity-components are approximately equal in their dominance with the absolute maximum of $|\hat{u}|$ being slightly higher. Further, the 1st-Mode is characterised by the two distinct local maxima of the streamwise

velocity amplitude-function, one being located close to the Blasius-length δ (corresponds to $z = 1$) and the other one near the boundary-layer edge δ_e.
In the work of Song & Dong [39], a different parameter set near the neutral point of the spatially stationary waves ($n = 0$) with a circumferential wavenumber β corresponding to non-integer wavefront counts n has been used for the amplitude-functions' visualisation, which is why they are not included in Figure 5.3. However, approximately the same maximum position of each amplitude-function has been found as well as the temperature fluctuation being the dominant quantity.

Onset of Rotation and Increase of Rotation Intensity

Now, the impact of the rotation intensity on the instability characteristics is addressed. Regarding the amplitude functions for $\bar{\Omega} = 0.3$ in Figure 5.3, the circumferential component becomes more dominant compared to the non-rotational case, even surpassing the maximum value of $|\hat{u}|$, and further, each amplitude-functions' absolute maximum shifts towards the boundary-layer edge. Otherwise, no changes in the distinctive characteristics of the instability's amplitude functions can be observed with the onset of rotation. However, the other rotation rates are also depicted in Figure 5.3, as these specific parameters are of importance in this section as well.

Next, the mode's change in the parameter space is examined. Figure 5.4 shows contour lines of the the 1^{st}-Mode's growth rates and the corresponding contour-lines in the frequency-wavefront-count domain for $\bar{\Omega} = 0.3$. The unstable area breaks its symmetry (cf. Figures 5.2) and shifts towards positive wavenumbers and lower frequencies with the onset of rotation. Therefore, waves travelling with the rotation of the cone destabilise and contrary, waves which travel against the cone's rotation, stabilise. This is in accordance with the work of Reed & Balakumar [2] and further, the mode's neutral curve nearly matches the observation presented in Song & Dong [39], as indicated by the dotted black curve in Figure 5.4. A visualisation for $\bar{\Omega} = 0.75$ is given in the appendix F as well as the individual growth-rate curves for $\omega = 0.1$ and $\omega = 0.2$ to show the consistency of this trend.
Figure 5.4 also hints at the mode's extension towards negative frequencies (cf.section 5.2), which has been identified as the Crossflow-Instability/Mode in the work of Song & Dong [39]. In the work of Liu [28] on the supersonic laminar boundary layer of a flat plate with cross-flow component in the basic flow, a similar extension of the 1^{st}-Mode is observed and it is discussed, whether the extension should be referred

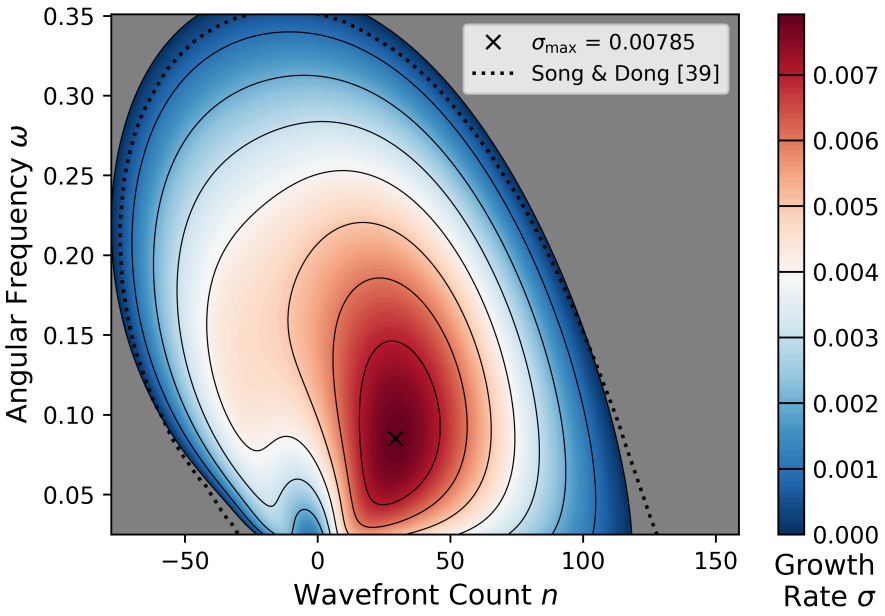

Figure 5.4.: Contour lines of the 1st-Mode in the ω-n-space for the 7°-M3-case with $\bar{\Omega} = 0.3$. In the grey-coloured domain, the 1st-Mode is stable ($\sigma < 0$). The dotted line refers to the result of the 1st-Mode's neutral curve presented in Song & Dong [39].

to as Crossflow-Instability or not. This is examined in more detail in section 5.2. However, note that the 1st- and the Crossflow-Mode share a common domain in the parameter space and are therefore difficult to track individually. Hence, some domains in the positive frequency-space near $\omega = 0$ of Figure 5.4 may not be linked to the 1st-Mode but to the Crossflow-Instability. However, this is also examined further in section 5.2 and it can be assumed, that for the angular frequencies of $\omega = 0.1$ and $\omega = 0.2$, the 1st-Mode is still the dominant instability (cf. Figure 5.4). Hence, these angular frequencies can be used for the analysis of the other influential parameters on the 1st-Mode's instability characteristics.

Influence of Metric and Rotation Terms

First, the influence of the metric and rotation terms in the stability equations is of interest. Figure 5.5 shows the growth-rate dependency on the wavefront count n for four different scenarios at the mentioned angular frequencies of $\omega = 0.1$ and $\omega = 0.2$ (for $\bar{\Omega} = 0.3$): The blue curve denotes the default setting with metric and rotation terms included; the red curve the opposite with both term sets excluded

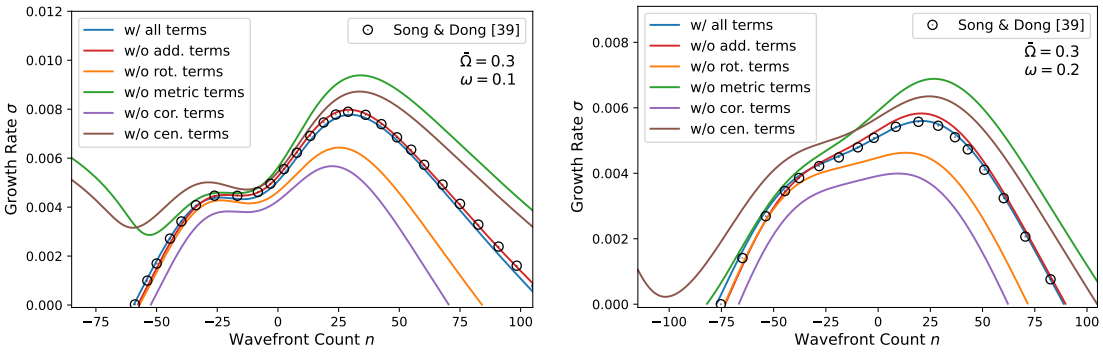

Figure 5.5.: Growth-rate curves plotted as a function of the wavefront count n at $\omega = 0.1$ (a) and $\omega = 0.2$ (b), varying the inclusion of metric and rotation terms in the stability equation (7°-M3-case, $\bar{\Omega} = 0.3$).

in the computations. Further, the green and the orange curve represent computations in which both have been deactivated separately to consider their individual influence. The growth rate is lowered due to the deactivation of the rotation terms. This indicates the general destabilising effect of the rotation terms on the 1$^{\text{st}}$-Mode. The opposite holds for the metric terms, as the growth rate is increased with their deactivation instead. But together, they balance out their individual effects such that the difference between the default setting and the exclusion of both term sets is minimal, with the latter being slightly less unstable. Also, the growth-rate curves of Figure 5.5 are in good agreement with the observations of Song & Dong [39], although the neutral curves do not match exactly for lower frequencies (cf. Figure 5.4). This indicates that the differences between both results are more dominant for the modes which occur with the onset of rotation, as e.g. the Crossflow-Instability (see section 5.2).

Unfortunately, the observation that the growth rate increases steadily in the negative wavenumber section for the computations without metric terms can not be explained entirely. It seems that during the computation the mode shifts to another mode nearby in parameter space. But in general, leaving out the metric terms means that the considered boundary-layer data is interpreted in terms of a flat plate instead of a cone which is the reason why that behaviour is not examined in more detail.

In Figures 5.5 (a) and (b), additional growth-rate curves are shown for computations, in which the Coriolis and centrifugal terms are excluded from the stability

equations' rotation terms respectively. The Coriolis terms depict the destabilising mechanism for the 1st-Mode, whereas the centrifugal terms have a stabilising effect. Further, the observed growth rate increase for low wavefront counts with the exclusion of the metric terms is reproduced for the case in which only the Coriolis terms are included in the rotation terms (and is also observable for $\omega = 0.2$). Hence, the Coriolis terms cause this effect, however the reason remains speculative.
The influence of the Coriolis and centrifugal terms will be revisited in section 5.4.2, as it is analysed, how each mode considered in this work behaves with the reducing influence of the respective terms.

Half-Opening Angle Variation

Finally, the 1st-Mode's dependency on the half-opening angle ψ is of interest.
Figure 5.6 depicts the growth-rate dependency on the frequency for $n = 45$, varying the half-opening angle and the rotation rate. Except for the wavenumber count, this figure is plotted in dimensional form to ensure comparison: The reference length is defined as the Blasius length $l^*_{ref} = \delta^*$ as in the work of Song & Dong [39] and is inter alia used for non-dimensionalising the frequency and the growth rate. However, the Blasius length does not scale with the boundary-layer thickness (cf. Equation 4.2). Therefore, comparisons between the non-dimensional growth-rate curves could lead to false conclusions. Contrary, the dimensional perspective allows a quantitative comparison and is generally applied if the ψ-dependency is examined or if a direct comparison of the M3- with the M6-case is performed. Note that the non-dimensional neutral curves might be identical, if the reference length is the boundary-layer thickness (although it is not tested in this work).
Two important conclusions are visible in Figure 5.6: On the one hand, the growth rate curves shift towards lower frequencies for increasing rotation rates as it has been observed before. Although the general idea of rotation destabilising the 1st-Mode still holds, the specific case of $n = 45$ stabilises for frequencies higher than a ψ-dependent critical value, which is marked with a cross for each half-opening angle in Figure 5.6. On the other hand, the increase of the half-opening angle destabilises the 1st-Mode. The maximal growth rate increases as well as the frequency range at which the 1st-Mode is unstable. This observation holds not only for the non-rotational case but also for $\bar{\Omega} = 0.3$. However, a further analysis of these cases for different wavefront counts shows an exception to this result. For $n = 0$, the

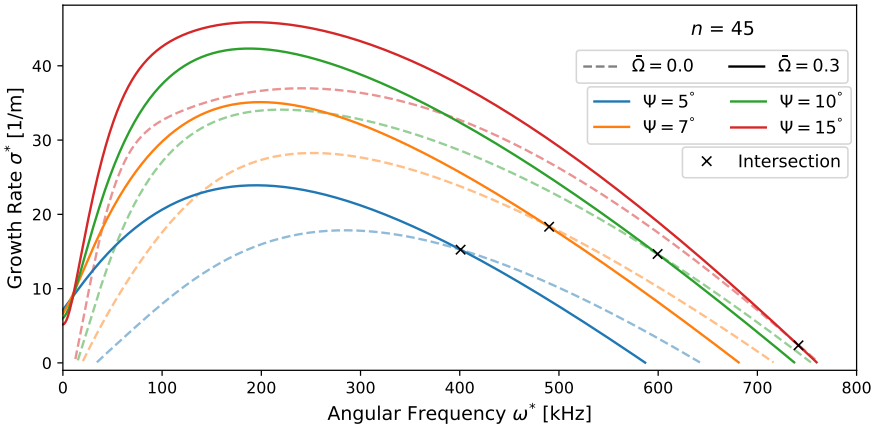

Figure 5.6.: Growth-rate curves plotted as a function of the angular frequency ω^* for different half-opening angles and rotation rates. The quantities are in dimensional form to compare absolute changes in the growth rate due to the half-opening angle variation.

unstable frequency-range does in fact decrease switching from a 10°- to a 15°-cone. This trend is already indicated in Figure 5.6 because the differences between the respective curves do decrease with higher half-opening angles. Unfortunately, higher angles have not been considered and this result is left open for future investigation.

5.1.2. Increase of the Oncoming Flow Speed to the Hypersonic Regime (M6-Case)

As mentioned in 1.2, the 2$^{\text{nd}}$-Mode only appears in M6-case and is identified as the more dominant mode in the parameter space, as different studies have reported prior to this work [2, 5, 16, 30]. It has also been observed that the unstable frequency domain shifts towards higher values compared to the 1$^{\text{st}}$-Mode and that the 2$^{\text{nd}}$-Mode is most dominant in its two-dimensional form ($n = 0$) [5, 16]. These three observations are shown in Figure 5.7 for the hypersonic non-rotating cone, as the 1$^{\text{st}}$- and 2$^{\text{nd}}$-Mode's growth rates are plotted in the frequency-wavefront-count domain for the M6-case. A comparison between Figures 5.7 and 5.4 shows that the 2$^{\text{nd}}$-Mode is not only more dominant but that the maximal growth rate of the 1$^{\text{st}}$-Mode decreases as well with the switch from supersonic to hypersonic flows. This is in agreement with observations of Chen [5] and Mack [29].

With the onset of rotation, similar results compared to the M3-case can be concluded

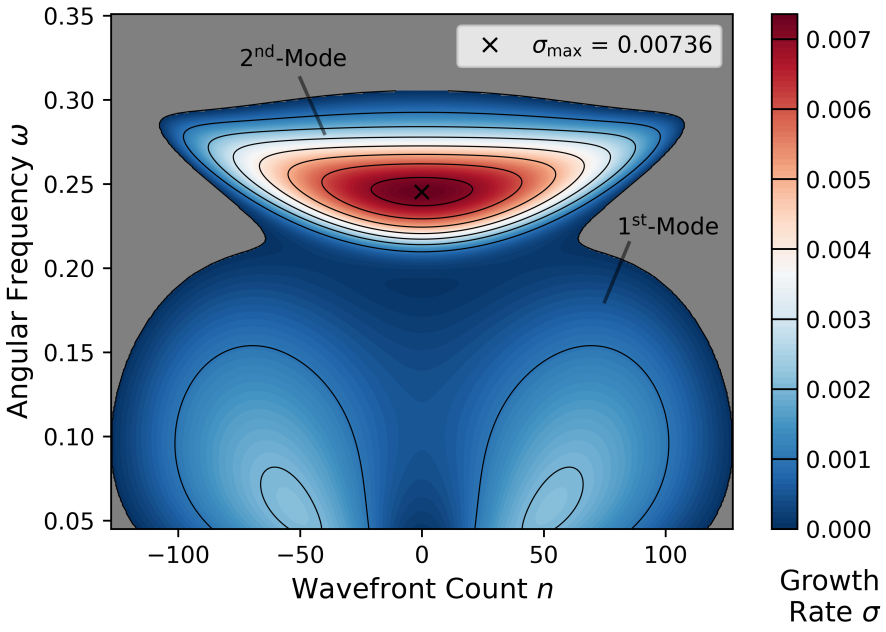

Figure 5.7.: Contour lines of the growth rate σ of the 2$^{\text{nd}}$-Mode in the ω-n-space for the 7°-M6-case without rotation. In the grey-coloured domain, the mode is stable ($\sigma < 0$).

for the M6-cases' 1$^{\text{st}}$-Mode, which is why supporting visualisations are only given in the Appendix F. The 1$^{\text{st}}$-Mode's unstable domain is also shifted towards positive wavenumbers and lower frequencies for the M6-case. Moreover, the rotation terms still destabilise and the deactivation of the terms causes the complete stabilisation of the 1$^{\text{st}}$-Mode in the parameter space. Ultimately, the effects of the metric and rotation terms almost balance each other out in the M6-case as well.
The only difference between the 1$^{\text{st}}$-Mode in the M6-case and in the M3-case lies in the ψ-dependency and will be dealt with in the next section.

For the 7°-cone, both the 1$^{\text{st}}$- and the 2$^{\text{nd}}$-Mode are directly connected in the parameter space. This has been reported prior to this work, e.g. by Mack [30]. However, the modes can disconnect with the variation of the half-angle (cf. Figure 5.11). For the 7°-cone, a differentiation between the 1$^{\text{st}}$- and the 2$^{\text{nd}}$-Mode is not possible from only analysing the growth rate behaviour. Instead, the visualisation of the amplitude functions in Figure 5.8 gives an insight into the mode shift with increasing frequency. The respective amplitude functions for the M3-case are included as well but using the corresponding reference values such that the comparison has to be dealt with caution.

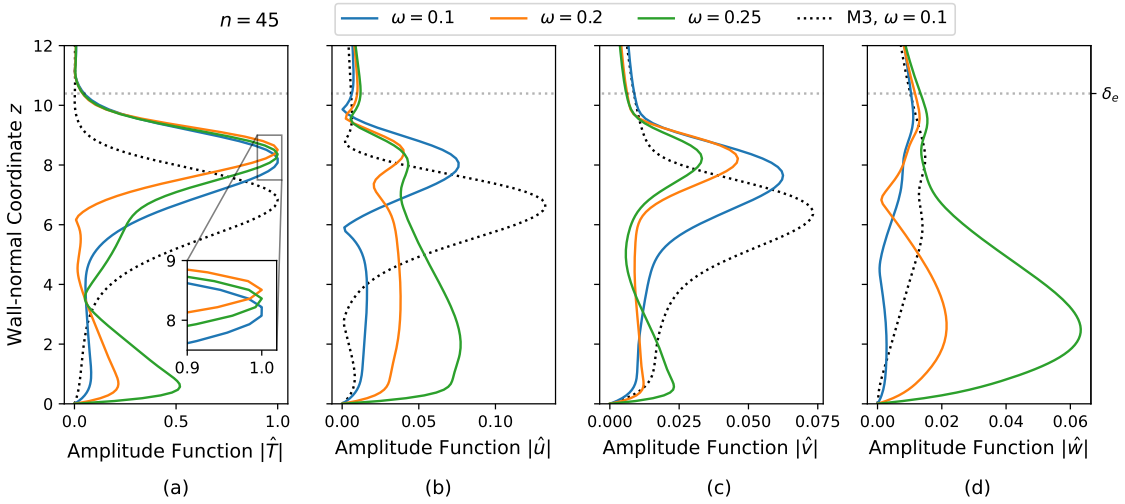

Figure 5.8.: Comparison of the amplitude functions $|\hat{T}|$ (a), $|\hat{u}|$ (b) $|\hat{v}|$ (c) and $|\hat{w}|$ (d) between the 1st-Mode at $\omega = 0.1$ and the 2nd-Mode at $\omega = 0.25$ (7°-M6-case, $n = 45$, no rotation).

Figure 5.8 shows that the transition from super- to hypersonic flows does not change the dominant disturbance quantity. But the maximum of $|\hat{T}|$ shifts towards the boundary-layer edge, now being located at $z = 0.79\delta_e$. The main difference between the M3- and the M6-case is the near-wall maximum, which does not only increase for the streamwise velocity-component but also appears for the other amplitude functions. This has been observed in prior studies as well [5, 33, 38]. Otherwise, the general distinctive characteristics stay the same with the three observed maxima of the $|\hat{u}|$-amplitude-function and the order of magnitude of $|\hat{w}|$ still being negligibly small for the 1st-Mode compared to the other amplitude functions.
With the frequency increase from $\omega = 0.2$ to $\omega = 0.25$ and therefore the shift from the 1st- to the 2nd-Mode, the near-wall local maximum further increases for each amplitude function and results to be the absolute maximum of the $|\hat{u}|$- and $|\hat{w}|$-velocity amplitude-function. Further, the influence of the streamwise and the circumferential velocities decrease and as the near-wall maximum of the wall-normal component increases, $|\hat{w}|$ becomes the shared dominant velocity amplitude function for the 2nd-Mode together with $|\hat{u}|$. Note that the near-wall maximum in the temperature amplitude function correlates with the boundary-layer profiles of the M6-cases' basic flow as the temperature profile also forms a near-wall local maximum, which surpasses the temperature of the wall (cf. Figure 4.12).

5.1.3. The 2nd-Mode with Oncoming Flow in the Hypersonic Speed Regime (M6-Case)

Influence of the Cone's Rotation

To the best of the author's knowledge, the influence of the cone's rotation on the 2nd-Mode has not been examined at all prior to this work. Therefore, Figure 5.9 shows the instabilities' general behaviour in the frequency-wavenumber plane for $\bar{\Omega} = 0.3$. An additional visualisation for $\bar{\Omega} = 0.75$ is included in the Appendix F as well as the growth-rates' dependency on the wavefront count n with changing rotation rates.

As mentioned before, the 1st-Mode still shifts towards positive wavenumbers and negative frequencies, which results in the transition to the Crossflow-Mode which has already been observed in the M3-case. However, the 2nd-Mode behaves contrary by shifting in the area of negative wavenumbers, meaning that waves travelling against the rotation of the cone become more unstable. Considering the hypersonic boundary layer of a flat plate, Liu [28] observed that with a cross-flow component in the basic flow, the 2nd-Mode shifted towards positive wavenumbers as did the 1nd-Mode. Hence, the 2nd-Mode on the rotating cone behaves contrary to the 2nd-Mode

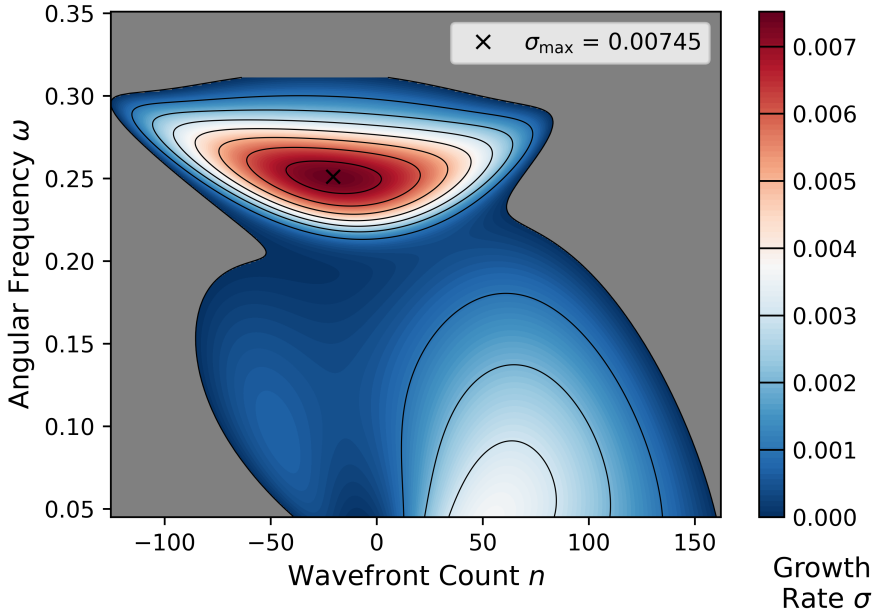

Figure 5.9.: Contour lines of the growth rate σ of the 2nd-Mode in the ω-n-space for the 7°-M6-case and $\bar{\Omega} = 0.3$. In the grey-coloured domain, the mode is stable.

on the non-rotating swept flat plate with cross-flow component. Further, a comparison between Figure 5.7 and 5.9 shows that the mode also shifts towards higher frequencies in the parameter space such that these waves are more unstable. As a similarity with the 1st-Mode, the mode's maximal growth rate increases with the rotation rate as well, which implies a general destabilising effect for the 2nd-Mode with rotation.

Influence of Metric and Rotation Terms

This section considers the influence of the rotation terms in the stability equations on the 2nd-Mode as well as the effect of the metric terms.
Therefore, Figure 5.10(a) shows the growth rate's dependency on the wavefront count n at the angular frequency $\omega = 0.25$ for the four different computation methods (default settings, no metric terms, no rotation terms and no additional terms), using the same colour scheme as in Figure 5.5. Generally, the influence of the terms on the 2nd-Mode is exactly the same as for the 1st-Mode: The rotation terms destabilise and the metric terms stabilise the instability. This is visualised in Figure 5.10(a) with the orange curve being located beneath and the green curve located above the growth-rate curve calculated without both terms in the stability equations. Further, the effects again balance each other out leading to the default-setting curve (*w/all terms*). However, the respective effects are not as strong as observed for the 1st-Mode in the M3-case and a better agreement between default settings and exclusion of both terms can be observed. Without visualisation, an additional analysis shows that these effects increase with the rotation intensity.

Half-Opening Angle Variation

With onset of rotation, the effect of the half-opening angle on the 2nd-Mode is similar to the non-rotating case: With the increase of ψ, the mode destabilises except for the transition from $\psi = 10°$ to $\psi = 15°$, as the maximal growth rate stays constant. Now, the question arises, why the 15°-cone is so far of from the other cases in the frequency domain. The answer is given in Figure 5.11 for the non-rotational case representatively. With increasing half-opening angle, the distance in the parameter space between the 1st- and the 2nd-Mode increases. The 2nd-Mode's unstable domain not only shifts towards higher frequencies but the 1st-Mode's occupied domain in the parameter space also shrinks significantly. This is observable both in dimensional

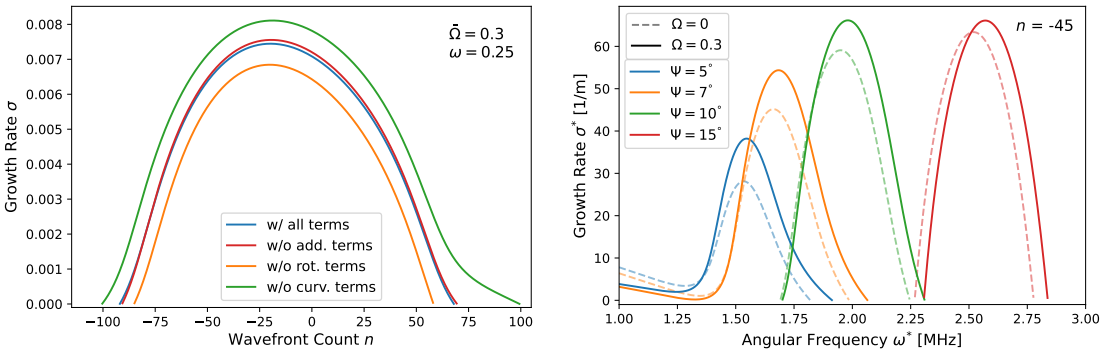

(a) (b)

Figure 5.10.: Growth-rate curves plotted as a function of the wavefront count n for $\omega = 0.25$, varying the inclusion of metric and rotation terms in the stability equation in (a) (7°-M6-case) and growth-rates curves plotted as a function of the angular frequency ω^* at $n = 45$, varying the half-opening angle in (b) (M6-case).

and dimensionless form, not making this observation a product of the different choices of reference values. Thus, the increase of the half-opening angles has a stabilising effect on the 1st-Mode in the frequency domain, contrary to the effect observed in the M3-case. Moreover, the detachment between the 1st- and 2nd-Mode increases with the half-opening angle such that even broader cones are of interest for future work. In the work of Mack [29], merging of the 1st- and the 2nd-Mode has been reported to be caused by the Mach-number increase. This is in agreement with the results of Figure 5.11, as the boundary-layer edge velocity at the location of $x^* = 0.4\,\mathrm{m}$ increases with decreasing half-opening angles (cf. Table 4.2). Further, Figure 5.11 visualises an expansion of the unstable wavefront-count domain with increasing half-opening angle. This expansion is due to the corresponding increase of the local radius such that for a given wavelength in circumferential direction, more wavefronts spatially fit into the boundary layer comparing $\psi = 15°$ with lower half-opening angles. Finally, an expansion of the 1st-Mode's unstable domain at low frequencies for the 5°-cone is observable. This irregularity has only been observed once in the convergence study of the basic-flow simulation. Stability analyses have been applied on basic flows of the non-rotational M3-case, which where simulated on unconverged grids, to see the differences to fully converged solutions with such expansions for low frequencies being the only difference. It indicates, that the results for the 5°-M6-case may not be fully grid-converged. The convergence study has only

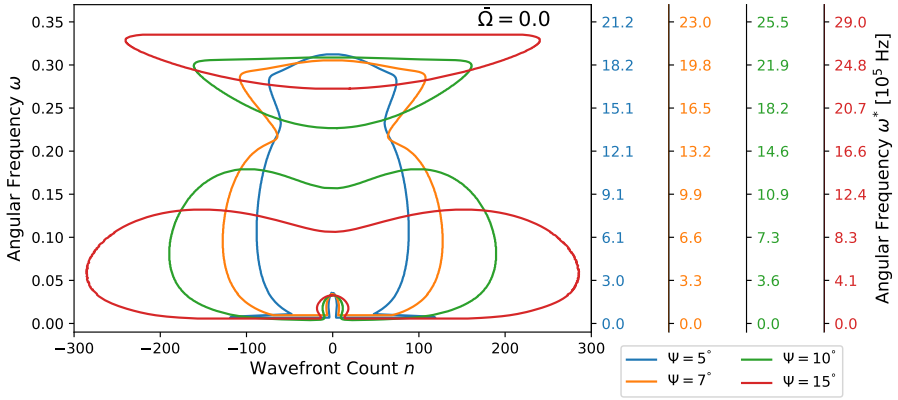

Figure 5.11.: Neutral curves for the 1st- and 2nd-Mode in the ω-n-space, varying the half-opening angle. The ordinates to the right denote the respective setup's dimensional angular frequency.

been performed for the 7°-cone and the grid resolutions were adopted for the other half-opening angles of the respective oncoming axial flows. But as mentioned, it only affects the low frequency-area and does not invalidate the other results observed above. This specific setup has still to be dealt with caution in the discussion of the Crossflow- and Centrifugal-Instabilities in the next sections.

5.2. The Crossflow-Instability

As mentioned in section 5.1.1, the Crossflow-Instability/Mode has been observed by Song & Dong [39] as the 1st-Mode's extension for positive wavenumber, with both partly sharing the same parameter space and therefore not being separable. Contrary, Liu [28] argued for the swept flat plate with cross-flow velocity component, that this extension can not be referred to as a Crossflow-Instability because no characteristic differences can be observed for the original 1st-Mode and its extension. Thus, examining the shift between the modes in more detail using the amplitude functions, this work adds a new argument for the Crossflow-Instability notation to this discussion. Subsequently, the Crossflow-Mode is analysed for the same influencing factors as before: Influence of the rotation, the half-opening angle ψ and the metric and rotation terms in the stability equations. Additionally, new modes with physically reasonable amplitude functions are reported and examined in more detail. From here on, the Crossflow-Instability is generally abbreviated as CR-Mode. Thus, the extension of the 1st-Mode is referred to as CR1-Mode.

5.2.1. Characterisation of Three Different Crossflow-Modes

Using rotation and metric terms in the stability analysis, two additional modes are reported in this work, partly sharing the parameter space with the CR1-Mode and not appearing with the exclusion of these terms.
Hence, the CR1-Mode is characterised first by visualising the transition process from the 1st-Mode. Moreover, a description is given, how the new modes have been found and how their amplitude functions differ from the CR1-Mode. Note that, in order to introduce the newly found modes, results of section 5.2.2 are referenced, which generally focus on the CR1-Mode. Finally, each new mode is examined individually in sections 5.2.3 and 5.2.4.

Transition from 1st-Mode to Crossflow-Instability (CR1-Mode)

In the parameter space, the 1st-Mode transits continuously into the CR1-Mode with decreasing angular frequency ω in both the M3- and the M6-case. Thus, the M3-case is chosen representatively for this study. In the amplitude functions in Figure 5.12, this shift is visible for the rotation intensity of $\bar{\Omega} = 0.4$ at a wavefront count of $n = 45$, as the frequency is decreased down to $\omega = 0$, which represents the stationary waves of the CR1-Mode. Again, Figure 5.12 (a) contains the amplitude functions for the temperature, whereas (b) and (c) plot the respective velocity amplitude functions. As for the 1st-Mode, the temperature is the dominant disturbance quantity in the CR1-Mode. However, there is a change in the intensity of the velocity components: The magnitude of $|\hat{u}|$ increases, whereas the maximum value of the circumferential amplitude function decreases with decreasing ω. This is counter-intuitive, given that the CR1-Mode is destabilised due to the cross-flow component in the basic flow, which linearly scales with the circumferential velocity component (cf. Equation 4.4). However, this trend changes with increasing rotation rates: For $\bar{\Omega} = 0.75$ the rotation intensity causes the circumferential velocity component to become more dominant, which is expected, as the rotation rate $\bar{\Omega}$ represents the ratio between oncoming axial flow and the wall's rotation speed (cf. section 4.3). Further, each amplitude function only consists of one distinct global maximum, as the two local maxima of $|\hat{u}|$ recede with the frequency decrease from $\omega = 0.05$ to $\omega = 0.01$. Moreover, the position of the $|\hat{T}|$-maximum changes in that frequency range, which therefore can be declared as the range, in which the shift between 1st- and CR1-Mode occurs for this specific wavenumber. This method of comparing

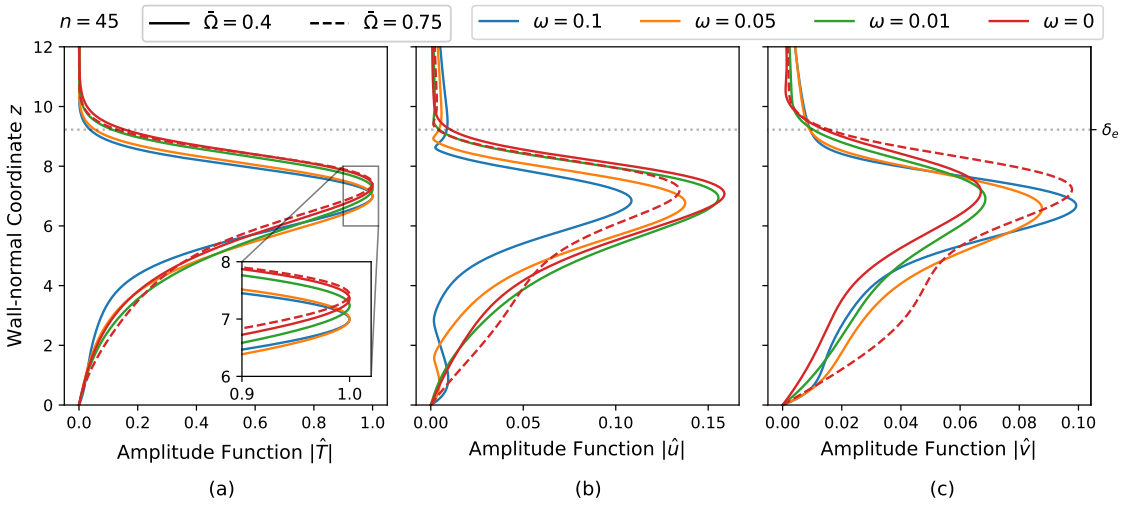

Figure 5.12.: Comparison of the amplitude functions $|\hat{T}|$ (a), $|\hat{u}|$ (b) and $|\hat{v}|$ (c) at $n = 45$ with decreasing ω, visualising the shift from the 1st- to the CR1-Mode (7°-M3-case).

the amplitude functions and investigating the changes in the characteristics of the amplitude functions with the mode shift could be applied for each wavefront count n and at a much higher frequency resolution to clearly separate the 1st-Mode from the CR1-Mode in the parameter space. However, it is beyond this work's scope and is left open to be analysed in future studies.

Revisiting the discussion about this mode's designation, Liu [28] states, that "no distinguishable features are observed pertaining uniquely to cross-flow mode". However, the results of Figure 5.12 argue for the extension to be referred to as a Crossflow-Instability mode, as it shows a change in the amplitude functions' characteristics with the frequency decrease, which clearly distinguishes the 1st-Mode from the CR1-Mode. Futher, Reed & Balakumar [2] reported that the Crossflow-Instability "covers a wide band of unstable frequencies (including zero)", which holds for this work's CR1-Mode as well.

Furthermore, features in the amplitude functions are reproduced, which have been reported for the Crossflow-Mode in the incompressible boundary layer of the cone rotating in still fluid (cf. Figure 3.4). For example, the Type-II-Mode, which is dominant at $\omega = 0$, also depicts only one maximum in the velocity amplitude functions. Further, $|\hat{v}|$ is the dominant velocity amplitude function, which also holds for the supersonic CR1-Mode if $\bar{\Omega} > 1$. Although comparisons between subsonic and supersonic instabilities have to be dealt with caution, the similarities between both

modes argue for the 1st-Mode's extension to be designated as a Crossflow-Instability. Thus, this work continues to refer to this extension when the cone is rotating as a Crossflow-Instability mode and therefore the CR1-Mode.

CR2-Mode superposed with the CR1-Mode's Frequency-Wavefront-Count Space

The analysis of the stationary CR1-Mode in section 5.2.2 depicts an abnormality in the growth rates' dependency on the circumferential wavenumber, for example for the rotation rate $\bar{\Omega} = 1$ (cf. Figure 5.16): For low wavefront-counts, a local maximum is observable, which does not fit to the growth-rate curve for higher n. This maximum belongs to a newly found mode, from here on referred to as the CR2-Mode. Note that, despite the name, the CR2-Mode is not related to the 2nd-Mode in any way. The CR2-Mode intersects with the CR1-Mode's parameter space for specific combinations of parameters and rotation rates (cf. Figures 5.25) but the separation of the CR1- and the CR2-Mode in the parameter space has been performed successfully for six different rotation rates.
To validate that the CR2-Mode depicts physical amplitude functions which differ from those of the CR1-Mode, the amplitude functions are shown in Figure 5.13 for $\bar{\Omega} = 0.4$ and different wavefront counts. Note that the CR2-Mode is only unstable using the default settings in the stability analysis. First, Figure 5.13 depicts another new characteristic of the CR1-Mode: The amplitude functions change significantly switching from $n = 5$ to $n = 25$. Although this behaviour could resemble a mode shift, the growth rate functions do not support this hypothesis (cf. Figure 5.16). The CR2-Mode behaves similarly, as the $|\hat{T}|$-maximum position for $n = 5$ is also located at a different wall-normal distance compared to higher wavefront counts. However, the CR2-Mode also depicts such a behaviour for the growth rate curves (cf. Figure 5.19(a)), as the growth-rate curve for low n does significantly differ compared to the growth rates at high n. Thus, this discussion is continued in section 5.2.3. For higher wavefront counts, the respective modes' maximal $|\hat{T}|$-positions detach, shifting upwards for the CR2-Mode and downwards for the CR1-Mode. Moreover, the velocity-components become less dominant for both modes. However, the qualitative form of the amplitude functions change, as the $|\hat{v}|$-function for example develops a near-wall local maximum for the CR2-Mode, which is only vaguely noticeable for the other two amplitude functions.

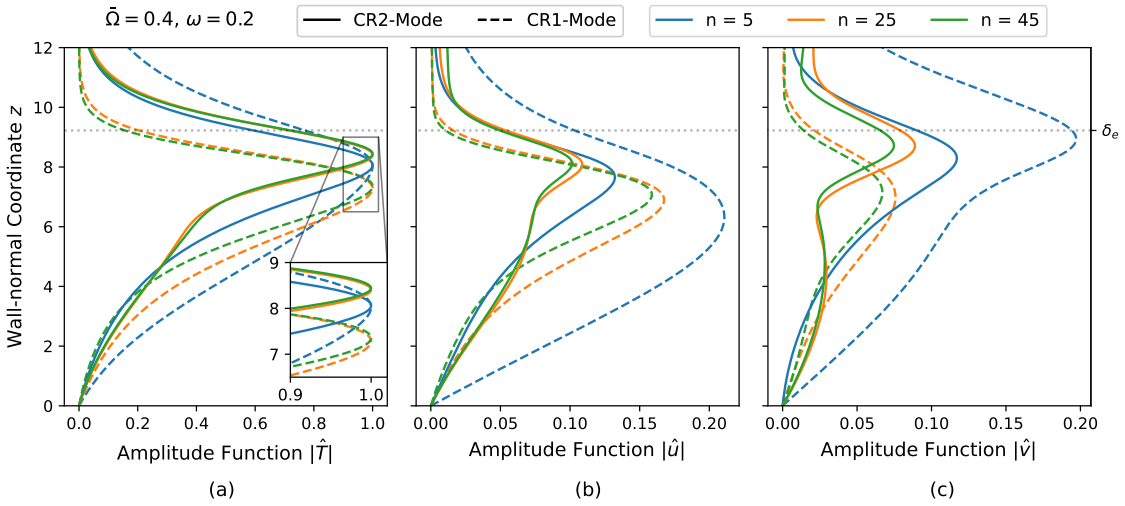

Figure 5.13.: Comparison of the amplitude functions $|\hat{T}|$ (a), $|\hat{u}|$ (b) and $|\hat{v}|$ (c) between the CR1- and CR2-Mode at $\omega = 0.2$ with increasing n (7°-M3-case).

Further, the CR2-Mode's amplitude functions look physically valid, as for example no oscillations can be observed in the considered frame and the functions tend to zero in wall-normal direction. This implies that that the CR2-Mode is to be analysed as the other modes, which is performed in section 5.2.3. However, it is unsure whether it is a real physical mode and will be discussed in more detail in chapter 6.

CR3-Mode extending the CR1-Mode's unstable Frequency-Domain

As the CR1-Mode's frequency is decreased, another mode shift occurs, which is shown in the analysis of the CR1-Mode in section 5.2.2: The CR1-Mode is expected to stabilise as the growth rate decreases along with the frequency. However, the growth-rate curve depicts a sudden and unexpected increase (cf. Figure 5.20(a)), which is identified to belong to a mode other than the CR1-Mode. This newly found mode, from here on intuitively referred to as CR3-Mode, can also not be isolated in parameter space from the CR1-Mode. Just as the the CR1-Mode is an extension of the 1st-Mode, the CR3-Mode emerges from the CR1-Mode and broadens the unstable parameter-space domain (more details are given in section 5.2.4). The shift from the CR1- to the CR3-Mode can again be observed in the amplitude functions visualised in Figure 5.14 in which the frequency is decreased for a rotation rate of $\bar{\Omega} = 0.4$ and a wavefront count of $n = 45$. The shift appears to happen between

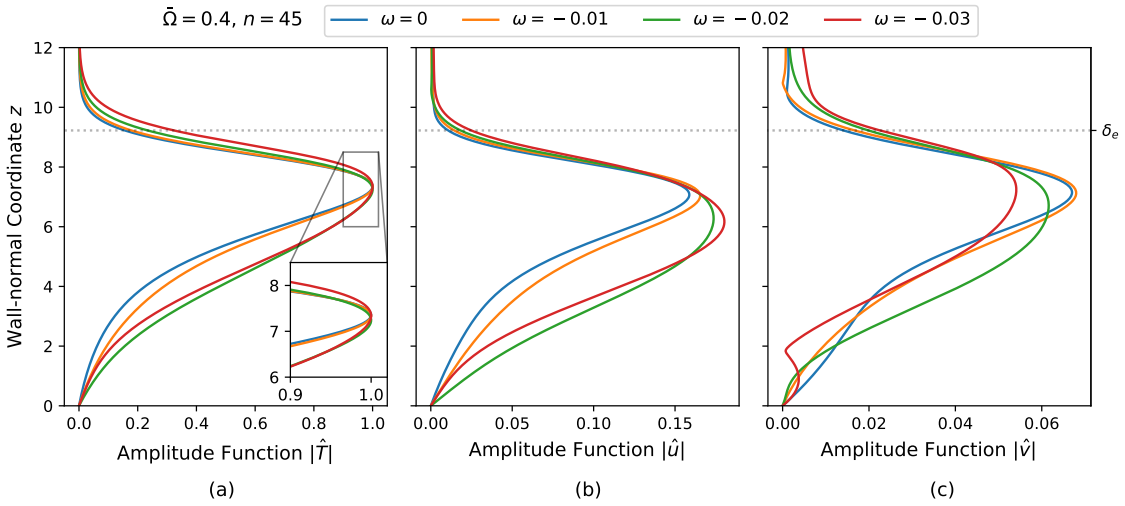

Figure 5.14.: Comparison of the amplitude functions $|\hat{T}|$ (a), $|\hat{u}|$ (b) and $|\hat{v}|$ (c) at $n = 45$ with decreasing ω, visualising the switch from the CR1- to the CR3-Mode (7°-M3-case).

$\omega = -0.01$ and $\omega = -0.02$ for this specific wavenumber of n = 45, because each amplitude function changes its form. For example, the circumferential velocity amplitude function develops a local maximum near the wall with decreasing frequency. Further, the behaviours of $|\hat{T}|$ and $|\hat{u}|$ change respectively as the amplitude functions decrease with ω in the region $z < 7$. However, the observed similarities between the CR1- and the CR3-Modes' amplitude functions underline the difficulty to isolate the modes. For example, the maximum position of the temperature amplitude does not change. Also, both modes generally depict one distinct maximum and an asymptotic nature towards zero near and far from the wall.
Note that, as for the CR2-Mode, the CR3-Mode is only unstable using the default settings in the stability analysis. Moreover, as the CR3-Mode depicts physically valid amplitude functions, it is analysed as a physically valid mode in section 5.2.4. However, the discussion about the physical validity is revisited in chapter 6.

5.2.2. Investigation of the CR1-Mode

Influence of Rotation and of the Additional Terms in the Stability Equations

As the CR2- and the CR3-Mode prevent a distinct isolation of the CR1-Mode in the parameter space using the default settings, this discussion starts examining the differences between the in- and exclusion of the metric and rotation terms in the

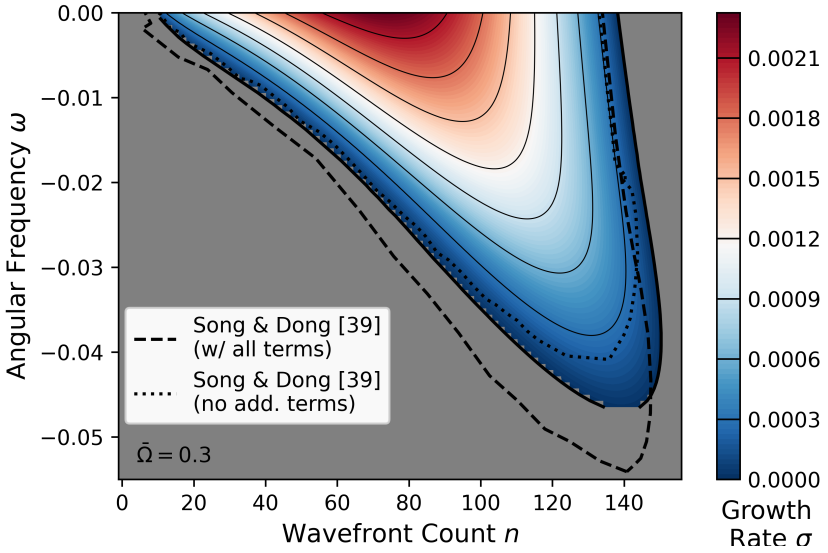

Figure 5.15.: Contour lines of the growth rate σ of the CR1-Mode in the ω-n-space for the 7°-M3-case and $\bar{\Omega} = 0.3$ without rotation and metric terms in the stability equation. In the grey-coloured domain, the mode is stable. The dashed and dotted curves refer to the neutral curves of the CR1-Mode presented in Song & Dong [39] computed with and without metric and rotation terms.

stability analysis. Therefore, the 7°-M3-case is of interest first. Because no individual growth rates have been plotted in the work of Song & Dong [39] with exclusion of the rotation and metric terms, the presented neutral curves have to be used for comparison to this work. Song & Dong [39] claim that the metric and rotation terms have only a small destabilising effect on the CR1-Mode. This is shown in Figure 5.15, as the dotted and dashed lines represent the results of Song & Dong [39] for the default settings and exclusion of the additional terms respectively.

Neither of the neutral curves presented in Song & Dong [39] depict perfect agreement with the neutral curve of this work (contour line $\sigma = 0$ in Figure 5.15). For the comparison of the analyses without additional terms, this work's neutral curve fits the literature's [39] for low wavefront counts, however neither does the minimal unstable frequency nor the neutral curve for high wavefront counts. As the stability-analysis results for the the non-rotating cone are in good agreement between the results computed with the corrected NOLOT-extension code and the results presented in Song & Dong [39] (cf. Figure 5.2(a)), the mismatches of the CR1-Mode are expected to be caused by the differences in the basic flow (cf. Figure 4.10): The respective

cross-flow velocity component U_c in the streamline-oriented coordinate system (cf. Equation 4.4) shows slight differences between this work and Song & Dong [39]. As the CR1-Mode destabilises due to the onset of rotation and the corresponding formation of the cross-flow component (cf. [28]), the observed differences in the neutral curves can be explained with the cross-flow component differences.

Using the default settings in the stability analysis of the CR1-Mode, single growth-rate curves describing stationary waves with $\omega = 0$ are used for comparison because the presence of the CR3-Mode prevents the CR1-Mode's isolation in the frequency-wavefront-count domain and therefore the display of contour lines such as Figure 5.15. Hence, Figure 5.16 visualises the growth-rate curves as a function of the wavefront count n for different rotation rates. The dotted lines represent the NOLOT-computations without the inclusion of metric and rotation terms in the stability equations. It is apparent that the additional terms stabilise the stationary CR1-Mode: The growth rates are generally lower for the respective curves computed with the default-settings and the unstable circumferential wavenumber domain is smaller.
Also, Figure 5.16 partly visualises the growth-rate curve for $\bar{\Omega} = 0.3$ calculated with the exclusion of the metric terms in the stability equations. It shows that, as for the 1$^{\text{st}}$-Mode, the rotation terms represent a destabilising mechanism for the CR1-Mode and the metric terms act stabilising. However, no growth-rate curves with the exclusion of the rotation terms are included in Figure 5.16 because, as stated in section 5.1, each CR-Mode is entirely stable if the rotation terms are excluded. This is revisited in section 5.4.2. Further, the growth-rate curve of Song & Dong [39] is generally higher than the respective curve computed with NOLOT. As for the neutral-curve differences, this is likely due to the differences in the basic flow.
Moreover, as mentioned in section 5.2.1, the curve computed with the default-settings for $\bar{\Omega} = 1.0$ has a local maximum for low circumferential wavenumbers (at $n \approx 5$) belonging to the CR2-Mode, as it was not separable from the CR1-Mode in that specific setup. For higher rotation rates, the switch from the CR1- to the CR2-Mode does not take place, because both mode's growth rate curves might not intersect. Therefore, the CR2-Mode is more difficult to find in the parameter space and the maximum is not depicted at all for $\bar{\Omega} > 1$. This discussion is revisited in section 5.4.1.
Also, the general form of the default-setting curves differ from the results without additional terms in the stability equations: It does not resemble a parabolic-like

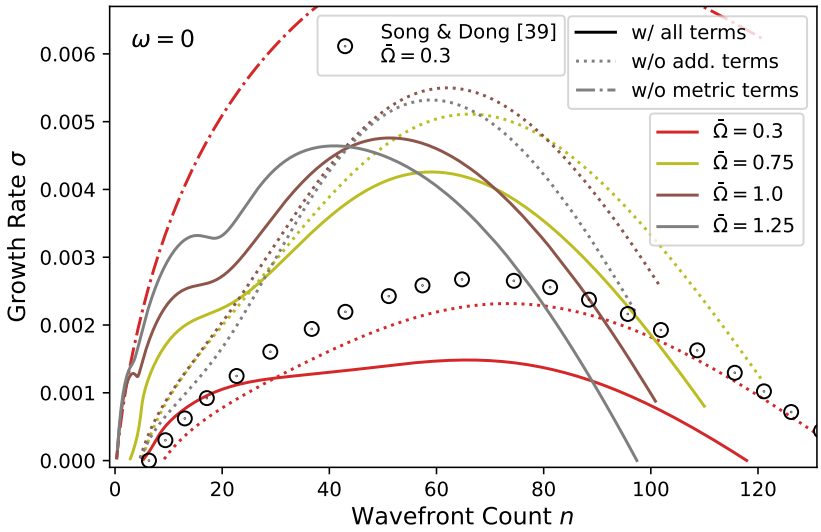

Figure 5.16.: Growth-rate curves of the CR1-Mode plotted against the wavefront count n at $\omega = 0$, varying the inclusion of the additional terms (metric and rotation terms) in the stability equation as well as the rotation rates (7°-M3-case).

function anymore as it is the case without using the additional terms. Instead the solid curves can each be divided into two section; one for low wavenumbers and one for high wavenumbers. For rotation rates lower than $\bar{\Omega} = 0.3$, the left part is dominant, depicting the absolute maximum of the CR1-Mode. With increasing rotation intensity, this changes, as the left part is a plateau or an additional local maximum (cf. growth-rate curve for $\bar{\Omega} = 1.25$ at $n \approx 10$) leading to the mode's absolute maximum on the right side. This division into the two parts does not explain the abnormality in the amplitude functions observed in Figure 5.13 because the left maximum/plateau also covers wavefront counts up to $n \approx 25$. Thus, for the stability analysis using the *default settings*, the CR1-Mode behaves differently with the increase of rotation, depending whether lower or higher wavefront counts are considered.

Lastly, the increase of rotation destabilises the CR1-Mode further, even for rotation rates higher than $\bar{\Omega} = 1.0$. At that point, the stationary CR1-Mode's growth rate may not increase, however this is due to the observed shift towards negative frequencies, as the stationary waves are not the most unstable disturbances for the CR1-Mode anymore. Consistently, this trend does not change whether the additional terms are in- or excluded in the computations.

Half-Opening Angle Variation

Furthermore, the influence of the half-opening angle is of interest which is visualised in Figure 5.17(a) for the stationary CR1-Mode at $\bar{\Omega} = 0.4$. Again, the dimensional growth rates are used to avoid falsified conclusions due to the different reference values.
The increase of the half-opening angles has a destabilising effect on the CR1-Mode and this effect further increases in intensity switching from $\psi = 10°$ to $\psi = 15°$. This holds not only for the results computed with the default settings but also for the stability-analysis results without both rotation and metric terms included. The parabolic-like form of the growth-rate curves for the analysis without additional terms and the non-parabolic-like form with the default settings are reproduced for every angle as well, as each curve computed with the default settings is divided into the mentioned two parts. Further, the CR2-Mode is observable for the 15°-cone at $n \approx 13$ as it could not be isolated from the CR1-Mode in that setup.

Shift to Hypersonic Flows

The switch from super- to hypersonic flow does not give any new significant insights as well. However, Figure 5.17(b) contains the stationary CR1-Modes' growth rates for five different setups. It shows that the CR1-Mode gets destabilised with the speed increase of the oncoming flow velocity. Otherwise, the characteristics are similar to the results above: The stationary CR1-Mode's growth rate curves depict a parabolic-like form for the exclusion of the additional terms and are more unstable compared to the curves of the results computed with the default settings. The latter are again divided into the two mentioned parts and also, the influence of the rotation rate's increase and the half-opening angle are the same as for the M3-case.
However, a problem in the NOLOT-computation is recognisable which is also of importance in the next sections. The red curve stops at a wavefront count of $n \approx 135$ without reaching its neutral point on the abscissa. As mentioned in section 2.4, NOLOT-computations are either performed for constant frequencies or constant circumferential wavenumbers, as the other one is varied using a specific increment. The results of the previous computation serve as initial values. In some computations, a very small increment is chosen and, although an adaptive sweeping method has been implemented, the increment decreased such that the computations are too time-consuming. This is the reason, why some curves are not fully resolved as it is

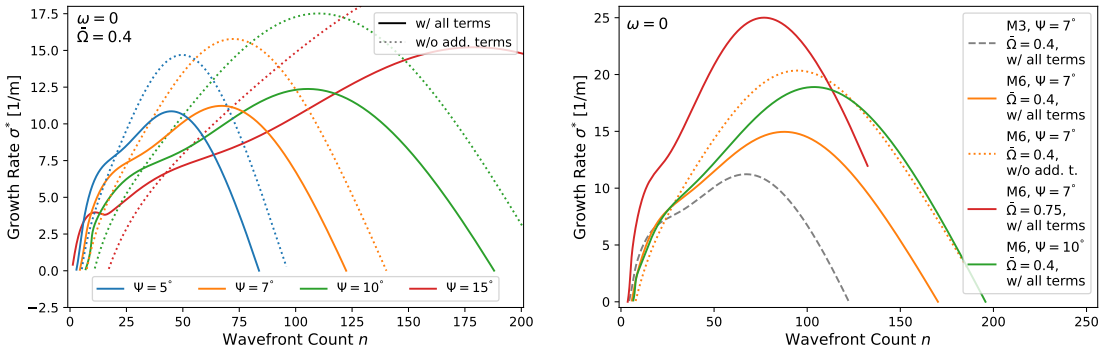

(a) (b)

Figure 5.17.: Growth-rate curves of the CR1-Mode plotted against the wavefront count n at $\omega = 0$ varying the half-opening angle and the inclusion of additional terms in the stability equation in (a) (7°-M3-case) and varying specific parameters as the Mach number in (b).

the case here. This problem will reoccur in the next sections but does not prevent the examination of the influencing factors for the different modes.

This concludes the analysis of the CR1-Mode. Unfortunately, as explained above, the negative frequency domain has mostly been neglected in the analysis. However, the results are expected to be similar to those presented in Song & Dong [39] and could be subject of future work.

5.2.3. Investigation of the CR2-Mode

This section focuses on the CR2-Mode and examines, how it behaves under the different influencing factors. As mentioned before, this mode is only unstable and therefore detectable if the rotation and metric terms are included in the linearised stability equations. Furthermore, although the CR2-Mode has been detected for the M6-case, it was impossible to isolate it from the CR1-Mode. Therefore, this section focuses on the M3-case only and does not examine the CR2-Mode for hypersonic free-stream conditions.

Behaviour in the Frequency-Wavefront-Count Space

Initially, a general overview of this mode is given to understand how it behaves in the frequency-wavefront-count domain. Such an attempt is shown in Figure 5.18

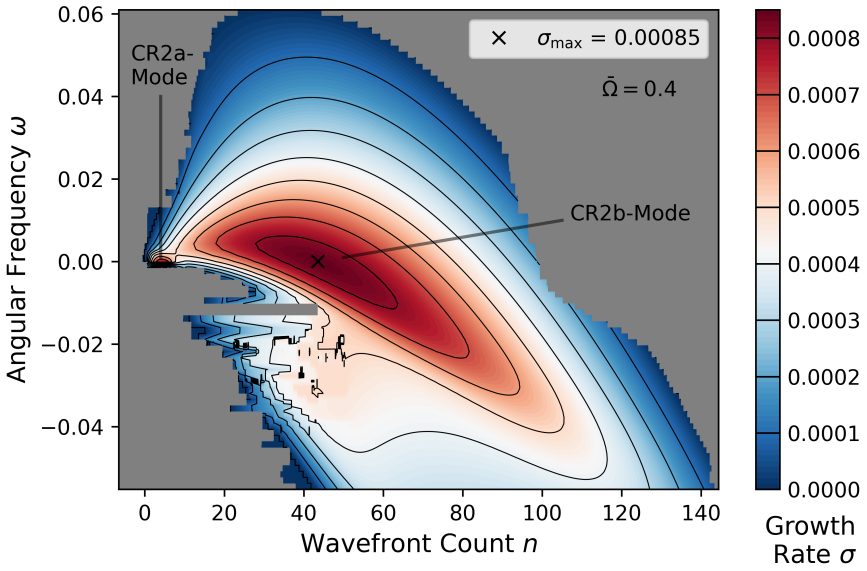

Figure 5.18.: Contour lines of the growth rate σ of the CR2-Mode in the ω-n-space for the 7°-M3-case at $\bar{\Omega} = 0.4$. The mode is stable in the grey-coloured domain. The contour for $\sigma = 0$ is not included due to the resolution problems.

for the 7°-M3-cone rotating with $\bar{\Omega} = 0.4$. Unfortunately, two resolution problems are apparent. For larger circumferential wavenumbers, the β-increment problem leads to high computation times such that the computation had to be aborted and the neutral curve could not be resolved in that domain. For negative frequencies, the unresolved sections originate from the superposition of the CR1- and the CR2-Mode in the parameter space. The constant switches between these two modes lead to jumps in the growth-rate functions such that the contours are not continuous.
Nevertheless, the CR2-Mode's characteristics are shown in Figure 5.18. The mode is generally less unstable than the CR1-Mode. The maximal value of $\sigma_{\max} = 0.00085$ is less than half of the CR1-Mode's most unstable growth-rate value for the same setup. Further, it consists of two distinct maxima, one at low circumferential wavenumbers and one for higher β-values. The left maximum can be identified as the wavenumber domain, in which the $|\hat{T}|$-amplitude function has a differently located maximum compared to the higher n (cf. Figure 5.12). The region around the right maximum is way broader and the maximum growth-rate value of the right part is similar to the left side's maximum growth-rate value. However, the right part becomes more unstable for a rotation rate of $\bar{\Omega} > 0.3$ compared to the left maximum. The right

maximum is stretched towards negative frequencies and higher wavenumbers, which seems to be the general behaviour of all CR-modes with the onset of rotation. But maximum values are located at $\omega \approx 0$ which still holds for increased rotation rates. Therefore, the stationary CR2-Mode can be used representatively to determine the influence of increased rotation. From here on, the CR2-Mode's part containing the left maximum is referred to as the CR2a-Mode and the part containing the right maximum as CR2b-Mode because both depict different behaviours with respect to the different influencing factors (as it can be seen in the next section).

Influence of Rotation

To analyse the influence of the rotation intensity, Figure 5.19(a) plots the growth rates of the CR2-Mode's stationary waves as a function of the wavefront count n for different rotation rates.
Again, the neutral points for each curve for higher wavenumbers is not resolved, as the increment problem increases the computation time. However, the important characteristics are still included: The growth rates of both the CR2a- and CR2b-Mode increase along with the rotation rate, which indicates the destabilising effect of the rotation intensity, and the CR2b-Mode's maximum exceeds the CR2a-Mode's maximum for a rotation rate of $\bar{\Omega} = 0.4$ (cf. Figure 5.18). However, the unstable circumferential wavenumber domain shrinks for both the CR2a- and the CR2b-Mode which is most likely due to a shift of the most unstable domain towards negative frequencies. This may not influence that the maximal growth-rate position is located at frequencies of $\omega = 0$ (stationary), but the general form of the CR2b-Mode's maximum in the frequency-wavefront-count space is less extended towards high n. As mentioned in the previous section, the mode is not separable from the CR1-Mode in the parameter space for higher rotation rates. For lower growth rates, the method presented in section 2.4 is used: Both the CR2a- and the CR2b-Modes are tracked individually for the transition between two rotation rates, such as $\bar{\Omega} = 0.3$ and $\bar{\Omega} = 0.2$, in order to provide initial values for the lower rotation rate. As visualised in Figure 5.19(a), the CR2b-Mode's growth rate for $\bar{\Omega} = 0.1$ is negligibly small and is separated from the CR2a-Mode, which underlines the separation of the CR2-Mode into the CR2a- and CR2b-Mode. Note that the dashed line for $\bar{\Omega} = 0.1$ represents an unstable domain, that can not be assigned to any mode considered in this work and is therefore neglected.

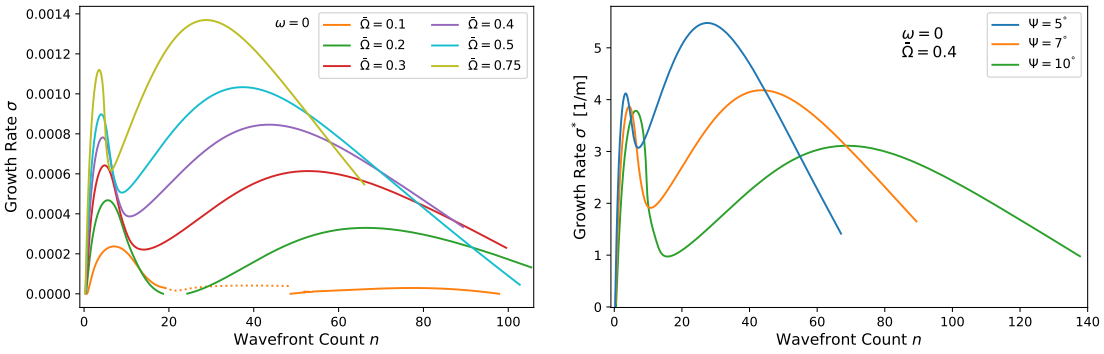

(a) (b)

Figure 5.19.: Growth-rate curves of the CR2-Mode plotted against the wavefront count n at $\omega = 0$ varying the rotation rate in (a) (7°-M3-case) and varying the half-opening angle in (b). In (a), the dashed part for $\bar{\Omega} = 0.1$ is not part of the CR2-Mode.

Influence of the Half-Opening Angle

The influence of the half-opening angle is visualised in Figure 5.19(b). Contrary to the above presented instabilities, the stationary CR2-Mode gets stabilised with increasing ψ. This holds for both the CR2a- and CR2b-Mode, but the CR2b-Mode broadens in the wavenumber-domain such that the number of unstable CR2-Mode waves increases along with the half-opening angle. As seen in Figure 5.17(a), the stationary growth-rate curve of the CR2-Mode for $\psi = 15°$ could not be isolated but is expected to fit into the observed trend.

It remains to be answered where the CR2-Mode originates, why it destabilises using the default settings in the NOLOT-computation and if the mode represents a physical instability. This is revisited in chapter 6.

5.2.4. Investigation of the CR3-Mode

In this section, the CR3-Mode's behaviour for the different influencing factors is of interest. Due to the increment problem in the stability analysis computation, the analysis is more difficult than for the other modes. Such small step sizes have to be chosen to compute the CR3-Mode's growth rates not only for high circumferential wavenumbers but also for further decreasing frequencies that a global picture in the parameter space is beyond the scope of this work. Nevertheless, the growth rate

dependency on the frequency for individual wavefront counts n can be calculated to give an idea of the mode's behaviour.
As mentioned before, the CR3-Mode is only unstable and therefore detectable using the default-settings in the stability analysis. Hence, only the influence of rotation, the half-opening angle and the speed of the oncoming axial flow are examined.

Influence of Rotation

Considering $n = 45$ and $n = 65$, the evolution of the growth rate is plotted in Figure 5.20 as a function of the angular frequency for rotation rates ranging from $\bar{\Omega} = 0.1$ to $\bar{\Omega} = 1.0$. The curve for $\bar{\Omega} = 0.1$ differs notably compared to the other rotation rates but this is due to the chosen wave ansatz: With decreasing frequency, the current mode switches to the CR3-Mode's parameter space for frequencies $\omega \geq 0$. At $\omega \approx -0.025$, the mode changes into the complex conjugate parameter space of the 1$^{\text{st}}$-Mode (cf. Equation 2.11). Hence, the observed curve is the equivalent of the growth-rate trajectory for positive and increasing frequencies at a wavefront count of $n = -45$. Moreover, the rotation's destabilising effect on the CR3-Mode is visible, as the maximal value increases as well as the unstable frequency domain with the increase of rotation intensity. Without giving a visualisation, the neutral frequency of waves with a wavefront count of $n \approx 122$ for example is located at $\omega \approx -0.15$. Instead, Figure 5.15 shows a neutral frequency of $\omega \approx -0.043$ for the CR1-Mode without the additional terms in the stability equations. Thus, the correlation between the CR1- and the CR3-Mode is similar to the CR1- and the 1$^{\text{st}}$-Mode: At a specific frequency range, a shift between CR1- and CR3-Mode takes place, such that the overall unstable frequency-wavefront-count domain gets extended, when metric and rotation terms are both included in the stability equations.
The statement that the CR3-Mode can distinctly be distinguished from the CR1-Mode is supported by the observation in Figure 5.20 that the CR3-Mode detaches from the CR1-Mode with increasing rotation rate. For $n = 45$, this phenomenon is visible for a rotation rate of $\bar{\Omega} = 1.0$. For higher circumferential wavenumbers and therefore higher maximal growth rates, the critical rotation rate decreases such that the modes are already fully detached for $\bar{\Omega} = 0.75$ at $n = 65$. Therefore, higher rotation rates are not included in Figure 5.20. However, the observed trends of increasing growth rates and increasing frequency-distances between the CR1- and CR3-Modes' unstable domains are expected to transfer to higher $\bar{\Omega}$.

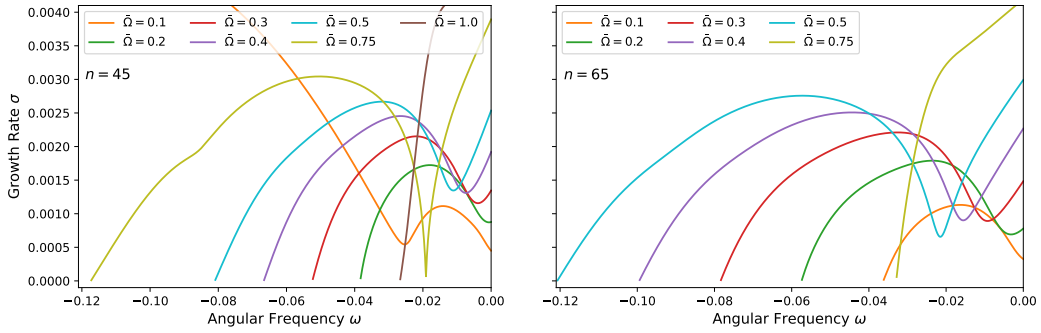

(a) (b)

Figure 5.20.: Growth-rate curves of the CR1- and CR3-Mode plotted against the angular frequency for different rotation rates at $n = 45$ in (a) and $n = 65$ in (b) (7°-M3-case).

Dependency on Half-Opening Angle and Inflow

For the influence of the half-opening angle, Figure 5.21(a) depicts the growth-rate curves of the CR1- and the CR3-Mode for different half-opening angles and for two rotation rates. The growth-rate curves show the same trends as before: The CR3-Mode detaches from the CR1-Mode for the most unstable setup of $\psi = 5°$ and $\bar{\Omega} = 0.75$ and the maximal growth rates and unstable frequency domains increase along with the rotation intensity for the respective angles as well. Otherwise, the half-opening angle has a stabilising effect on the CR3-Mode contrary to the CR1- and the 1$^{\text{st}}$-Mode: For example, the 5°-cone's CR3-Mode destabilises for more negative frequencies than the 10°-cone, which corresponds to the destabilising effect on the CR1-Mode. However, the CR3-Mode then extends towards more negative frequencies for the 5°-cone and has an higher maximal growth rate value, indicating the destabilising effect of reducing ψ. Changing to hypersonic flows, Figure 5.21(b) compares the growth-rate curves for both M-cases for three different rotation rates. As in the M3-case, the rotation intensity destabilises the CR3-Mode in the M6-case. Further, the switch from super- to hypersonic flows destabilises the CR3-Mode, as the neutral frequency for $\bar{\Omega} = 0.75$ and $n = 45$ is located at $\omega^* \approx -5.4 \cdot 10^5$ Hz compared to $\omega^* \approx -2.6 \cdot 10^5$ Hz for the M3-case.

Because of the increment problem, this concludes the analysis of the CR3-Mode. However, as for the CR2-Mode, the discussion about the physical validity of the CR3-Mode is revisited in chapter 6.

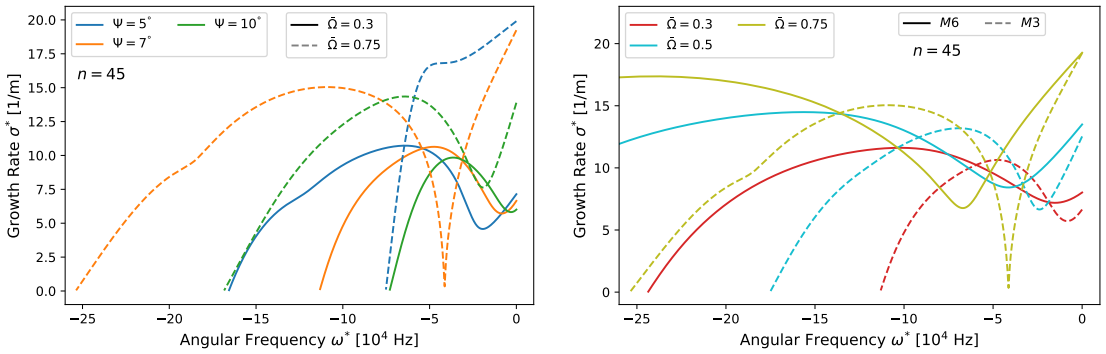

(a) (b)

Figure 5.21.: Growth-rate curves of the CR1- and CR3-Mode plotted against the angular frequency at $n = 45$ for different half-opening angles and rotation rates in (a) (M3-case) and different oncoming-flow speeds and rotations rates in (b) (7°-cone).

5.3. The Centrifugal-Instability

Finally, the Centrifugal-Instability is of interest and is referred to as the CE-Mode from here on. In the work of Song & Dong [39], it is reported that this instability is only unstable with rotation and metric terms included in the stability equations. This work shows that only the rotation terms cause the destabilisation of the Centrifugal-Mode. Further, two methods to determine the critical rotation rate at which this instability becomes unstable are compared. The methods are tested for two different cones' half-opening angles and both M-cases respectively.

5.3.1. Influence of Rotation, Half-Opening Angle and Speed Regime of Oncoming Flow

Figure 5.22 shows the CE-Mode's behaviour in the frequency-wavefront-count domain for a rotation rate of $\bar{\Omega} = 0.75$. A corresponding visualisation for $\bar{\Omega} = 1.25$ is given in Appendix F. Compared to the stationary growth-rate curves of the CR1-Mode in Figure 5.16, the CE-Mode is more unstable, with the maximal growth rate twice as high. Further, the unstable domain shifts towards higher wave front counts and the most unstable area in parameter space is located at negative frequencies. Contrary to the already considered modes, this maximal growth-rate position shifts

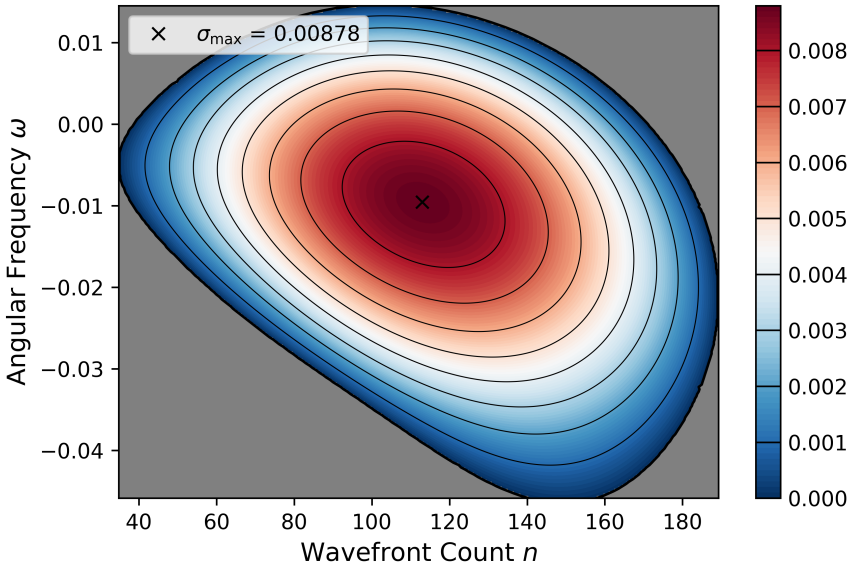

Figure 5.22.: Contour lines of the growth rate σ of the CE-Mode in the ω-n-space for the 7°-M3-case at $\bar{\Omega} = 0.75$. The mode is stable in the grey-coloured domain.

towards lower wavenumber counts and higher - and for increasing rotation rates even positive (c.f. F.11) - frequencies with increased rotation intensity. However, the growth-rate curves of the stationary CE-Mode visualised in Figure 5.23(a) destabilises despite the observed shifts, which is due to the modes general destabilisation with increased rotation: The maximal growth rate of the CE-Mode for $\bar{\Omega} = 1.25$ is three times as high as for $\bar{\Omega} = 0.75$.

Additionally, the comparison to the results of Song & Dong [39] is given in Figure 5.23(a) for the stationary CE-Mode. Good agreement has been reached between this work and Song & Dong [39] for the left side of the CE-Mode's growth rate curve for each considered rotation rates. However, the stability analysis of Song & Dong [39] reveals a more stable CE-Mode, as the respective maximal growth rates are lower and narrower bandwidths of the amplified wavefront-count range are observed. The mismatches can be explained with the differences in the basic flow and were therefore expected.

Figure 5.23(b) summarises the influence of the half-opening angle and the free-stream Mach number on the stationary CE-Mode representatively. First, the increase of ψ flattens the growth rate curve: The maximal growth rate lowers and the unstable domain shifts towards higher wavenumber counts. Since the frequency

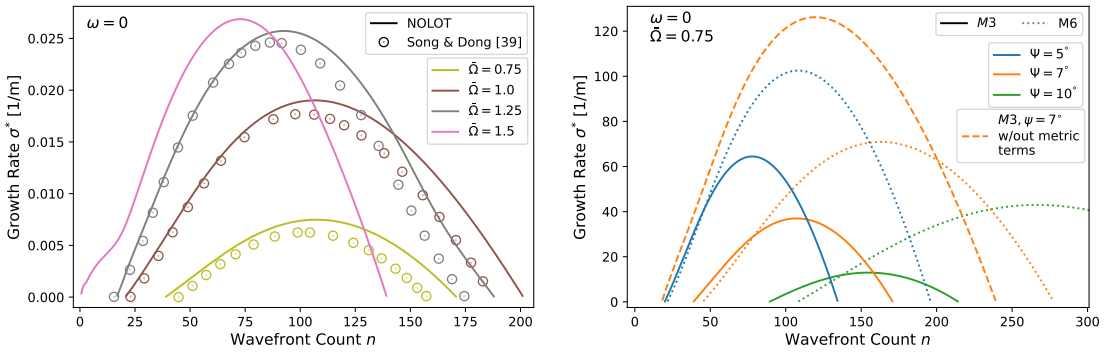

(a) (b)

Figure 5.23.: Growth-rate curves of the CE-Mode plotted against the wavefront count n at $\omega = 0$ for different rotation rates in (a) (7°-M3-case) and different half-opening angles and oncoming-flow speeds in (b).

representing the CE-Mode's maximal growth rate is found to be approximately constant with variation of the half-opening angle (c.f. Figure F.12), the decrease in the growth-rate curve is due to the stabilising effect of the half-opening angle and not from any shift in the frequency domain. The shift towards higher wavefront-counts is the same as for the other modes (c.f. Figure 5.11) and is caused by the increase of the cone's local radius. However, the change in the growth rates shows that the increase of the local radius is not as important as the corresponding decrease of the dimensional rotation rate due to the decrease of the reference velocity with the half-opening angle increase (c.f. Tables 4.2, D.1 and D.2). This is due to two reasons: The effects of the rotation terms in the stability equations outweigh the influence of the metric terms on the mode's behaviour, although the mode destabilises significantly with the exclusion of the metric terms, as indicated by the dashed curve in Figure 5.23(b). Further, the change in the rotation rate outweighs the change of the local radius within the rotation terms. This indicates that, for the CE-Mode, the Coriolis terms are more dominant than the centrifugal terms, as only the centrifugal terms linearly depend on the local radius (c.f. Equation 2.6). Moreover, the centrifugal terms could cause a stabilisation due to the quadratic dependency on the rotation rate. This is examined in more detail in section 5.4.2.

The comparison between the M3- and the M6-case does not provide any new insights. The behaviour with the half-opening angle is similar, as is the influence of the rotation rate. However, the mode generally destabilises with the Mach-number increase as shown in Figure 5.23(b).

5.3.2. Prediction of the Critical Rotation Rate

In this section, two different methods are presented in order to predict the critical rotation rate at which the stationary CE-Mode becomes unstable at the position $x^* = 0.4\,\mathrm{m}$: Linear extrapolation is compared to the method introduced in section 2.4. Each quantity in the respective plot is given in dimensionless form because only the qualitative comparison is of interest, unlike to the results presented in previous sections regarding the Mach-number or the half-opening angle influence.

Figure 5.24(a) shows the maximal growth rates of four different setups, namely for the cones with half-opening angles of $\psi = 5°$ and $\psi = 7°$ for the M3- and M6-cases. The slopes between the growth rates of the two lowest rotation rates, at which the CE-Mode has been found to be unstable using educated guesses as initial values, are extended via linear extrapolation. This method shows that, for the 7°-M3-cone, the CE-Mode stabilises before a rotation rate of $\bar{\Omega} = 0.5$ is reached. For the other setups, the CE-Mode is still predicted to be unstable at this rotation rate, but the 5°-M3-cone's CE-Mode is in the process of stabilising. This method is expected to be inaccurate because each maximal growth-rate curve does not resemble a linear function. Instead, the slope is expected to increase further due to the modes shift towards more negative frequencies in the ω-n-space. Hence, this method's results can be interpreted as lower bounds. But in general, linear extrapolation has to be dealt with caution because the mode's behaviour in the parameter space can change drastically between the different external factors.
In the work of Song & Dong [39], the method of linear extrapolation was used once to determine the CE-Mode's critical rotation rate considering every location on the cone without the restriction of $x^* = 0.4\,\mathrm{m}$. For example, it was reported that the CE-Mode is unstable for $\bar{\Omega} = 0.5$ at a Reynolds number corresponding to a location further downstream than $x^* = 0.4\,\mathrm{m}$. Unfortunately, their result of $\bar{\Omega}_{\mathrm{crit},\omega=0}(x) = 0.4$ for the 7°-M3-cone could not be tested, as the neutral position at this rate of rotation would be beyond this work's restriction to cones of length $l^*_{\mathrm{cones}} \approx 0.6\,\mathrm{m}$. Hence, testing this hypothesis using the method presented in the following could be of interest for future work.

The method introduced in section 2.4 is used to determine the critical rotation rate at which the CE-Mode becomes stable, being restricted to $x^* = 0.4\,\mathrm{m}$. The transition from $\bar{\Omega} = 0.75$ to $\bar{\Omega} = 0.5$ is shown in Figure 5.24(b) for the in Figure 5.24(a) considered setups. It is to mention, that $\chi = 0.5$ does not represent a rotation

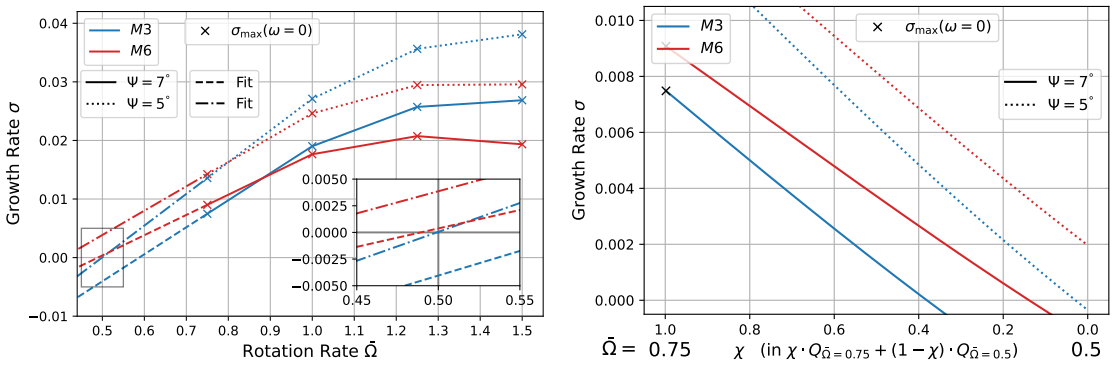

(a) (b)

Figure 5.24.: Methods to predict the critical rotation rate at which the CE-Mode destabilises for 5°- and 7°- M3- and M6-cases: (a) Linear extrapolation based on the growth-rate slope with respect to the rotation rate between $\bar{\Omega} = 1.0$ and $\bar{\Omega} = 0.75$. (b) Method presented in section 2.4.2: Manipulation of the NOLOT-input file to track the transition between $\bar{\Omega} = 0.75$ and $\bar{\Omega} = 0.5$.

rate of $\bar{\Omega} = 0.625$ but only a non-physical transition state, in which the physical quantities $Q_{\bar{\Omega}=0.75}$ are as dominant as those for a rotation rate of $\bar{\Omega} = 0.5$.
Using the parameters, at which the stationary CE-Mode has its maximal growth rates, the corresponding solution of the stability equation for $\bar{\Omega} = 0.5$ are calculated, showing that the respective waves become stable for all cases except the 5°-M6-cone. For the other setups, the calculated parameters are used as starting values for further analyses, with the results that the stationary CE-Mode is also unstable for the 7°-M6-cone in a different wavefront-count regime (although the maximum growth rate is negligibly small), and that both M3-cases have a small unstable domain in the parameter space for negative frequencies.
Thus, the second method is superior compared to the method using linear extrapolation because it directly calculates the mode's parameters for the considered rotation rate and therefore predicts the critical rotation rate with a higher accuracy. However, despite these problems in accuracy, the first method provides a general overview of the possible lower limit and also estimates the growth rates for rotation rates not considered in the basic-flow simulations.

This concludes the analysis of the Centrifugal-Instability. However, section 5.4 provides additional studies for every considered instability type and therefore also deals with the behaviour of the CE-Mode in parameter space in more detail.

5.4. Behaviour in Parameter Space and the Influence of the Individual Rotation Terms

In this section, additional analyses are presented to gain further insights into the modes' behaviour in parameter space and to better understand the destabilising mechanism which drives the modes to be unstable.
Hence, the Coriolis and centrifugal terms of the stability equations are of particular interest. It is shown which terms represent the driving force for each instability type. This is already briefly addressed for the 1st-Mode in Figures 5.5 but is summarised and generalised here.

5.4.1. Comparison of the Crossflow-Modes in Parameter Space

First, the parameter space is considered for the modes that destabilise with the onset of rotation, namely the CR1, -2 and -3-Mode as well as the CE-Mode. In section 5.2, it is argued that these modes occupy the same or nearby domains in the parameter space such that differentiation and isolation is difficult using NOLOT to solve the stability equations. The streamwise wavenumber α_r is not considered in sections 5.1 to 5.3 and is therefore examined here using the 7°-M3-cone with a rotation rate of $\bar{\Omega} = 0.75$ representatively.
Figure 5.25(a) plots the streamwise wavenumber α_r as a function of the wavefront count n for the respective stationary waves of the CE, CR2- and the CR1-Modes, while Figure 5.25(b) compares the corresponding growth rates using the same setup and colour scheme. First of all, the streamwise wavenumbers of the CR1-Mode with and without the use of rotation and metric terms in the stability analysis are in good agreement. The most significant difference lies in the growth rate's maximal value and its evolution, as it has been pointed out in section 5.2.2. The streamwise wavenumber curves are similar for small circumferential wavenumbers and differ only slightly with increasing wavefront counts. The CE-Mode's lower neutral wavefront count is found to be shifted towards larger n, whereas the CR-Modes are already unstable for $n < 10$. However, the CE-Mode is generally separated from the CR-Modes: Although the modes share a common frequency and wavefront count domain, the growth rates differ significantly, with the maximal rate for the CE-Mode being one and a half times that of the CR1-Mode without considering the additional terms in the stability equations. Furthermore, the curve for the streamwise wavenumber α_r

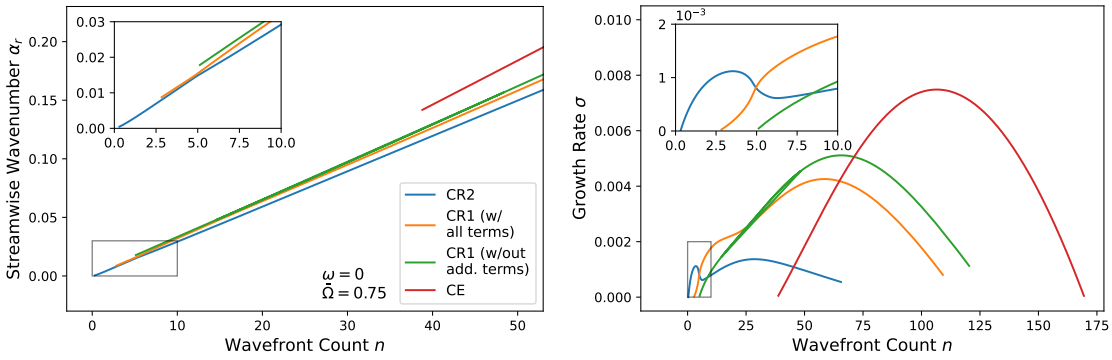

(a) (b)

Figure 5.25.: Parameter-space analysis of the stationary CR1- CR2- and CE-Modes with respect to the wavefront count n. (a) Streamwise wavenumber α_r and (b) growth rate σ as a function of n.

is separated, being located at higher values compared to the Crossflow-Modes. This has an effect on the NOLOT-computation. As already described, in order to detect a mode's trajectory in the ω-n-space, one quantity is held constant, while the other is varied, using the previous state as the initial values for the next. For a mode that is isolated in the parameter space as the CE-Mode, two characteristics define the computations. Firstly, the mode is difficult to find. The only strategy are educated guesses for the initial parameters which have been inspired by the results of Song & Dong [39]. However, if the mode is found, it is easy to follow its trajectory in the parameter space because the computations can not converge towards another mode. This changes, if the occupied domains of each mode are located closer to each other in the parameter space (α_r,α_i) as it is the case for the CR2- and the CR1-Mode. For these modes, there is a wavefront count region around $n \approx 5$, where the respective curves of both the streamwise wavenumber α_r and the growth rate σ intersect. In that domain, the NOLOT-computation can converge towards the other mode if the intersection is not skipped due to large increments. This is the reason why the CR2-Mode was found at all. For rotation rates $\bar{\Omega} < 0.3$, this intersection does not exist, so for Figure 5.19(a), the method presented in section 2.4 was used to calculate the CR2-Mode separately.

Next, Figure 5.26 includes the CR3-Mode by visualising the dependence of the modes' streamwise wavenumbers α_r (a) and growth rate σ (b) on the angular frequency ω for waves with $n = 24$. As in Figure 5.25, Figure 5.26 shows the detach-

ment of the CE-Mode from the other CR-Modes as well as the similar behaviour of the CR1-Mode for using or neglecting the rotation and metric terms in the stability analysis. Further, the α_r-curves of the CR1- and the CR2-Mode are nearly parallel with a constant offset, such that mode-switching is not possible for this wavefront count. This can be observed by comparing Figure 5.15 with Figure 5.18, in which the growth rates are determined for the global frequency-wavefront-count domain. For $n = 5$, however, the modes are closer together in the parameter space compared to $n = 45$, as Figure 5.18 depicts many mode-switches with decreasing frequency at low wavefront counts.
Figure 5.26 also visualises the switch from the CR1- to the CR3-Mode for $\omega = -0.02$. In the growth-rate curve, this can be seen as the already observed sudden increase after almost reaching this wave's neutral frequency for the CR1-Mode. But in the α_r-curve, a plateau connecting two straight lines denotes the switch, so the switch happens continuously.

This analysis could be much more detailed, as the real part α_r of the streamwise wavenumber could be analysed not only for single trajectories, but in the entire unstable parameter domain. It could be useful to understand the destabilising mechanisms behind the newly found modes. However, it exceeds the scope of this work and has to be revisited in future studies.

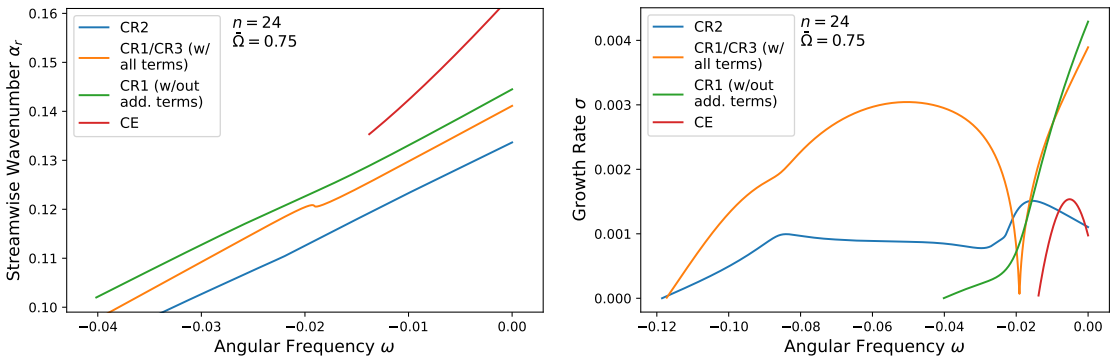

(a) (b)

Figure 5.26.: Parameter-space analysis of the CR1- CR3- and CE-Modes with respect to the angular frequency ω at $n = 24$. (a) Streamwise wavenumber α_r and (b) growth rate σ as a function of ω.

5.4.2. Influence of Coriolis and Centrifugal Terms

Finally, this section focuses specifically on the impact of the rotation terms.
As presented in section 2.2, the rotation terms are a correction of the momentum equations in the Navier-Stokes equations for a rotating coordinate system and can be divided into the Coriolis and the centrifugal terms. In section 5.1, this division is considered for the 1st-Mode, which is destabilised by the Coriolis terms and stabilised by the centrifugal terms (see Figure 5.6). In this section, this dependency is considered for each mode using the method presented in section 2.4: A factor ζ is introduced to continuously reduce the respective influence of the terms on the stability analysis, with $\zeta = 1$ being completely included and $\zeta = 0$ being completely excluded from the stability equations.
The results for each mode are summarised in Figure 5.27 using a representative choice of the parameters n and ω: As initial values for each computation, one of the parameters n or ω is set and based on this choice, the maximal growth rate of the specific setup determines the other parameter; for example, for the 1st-Mode, this is the wavenumber count at which the growth-rate curve is maximal for $\omega = 0.1$. Note that the position of the maximal value can shift with the decreasing factor ζ, but it can still be used as an indicator whether the mode is expected to be stable or unstable after excluding the respective terms.
In general, the 1st- and the 2nd-Mode are less dependent on the rotation terms than the modes that only destabilise when the cone is rotating. On the other hand, the CE- and the CR-Modes stabilise with the exclusion of the rotation terms. Furthermore, the Coriolis terms constitute the destabilising mechanism for each mode, while the centrifugal terms stabilise each mode, except for the right maximum of the CR2-Mode (see below). As a consequence of both observations, the Coriolis terms can be interpreted to be dominant in the rotation terms compared to the centrifugal terms for each CR- and the CE-Mode.
This also gives the answer to the unexpected half-opening angle dependence of the CE-Mode (cf. Figure 5.23(b)). As the local radius increases, the centrifugal terms may become more important, but the change in the velocity field and the corresponding decrease in the rotation rate outweigh, so the decreasing Coriolis terms stabilise the mode.
Moreover, the different behaviour of the CR2a- and the CR2b-Modes supports the division of the CR2-Mode into two different modes that overlap in the parameter space, as assumed in section 5.2.3. The similarities between the CR1- and the

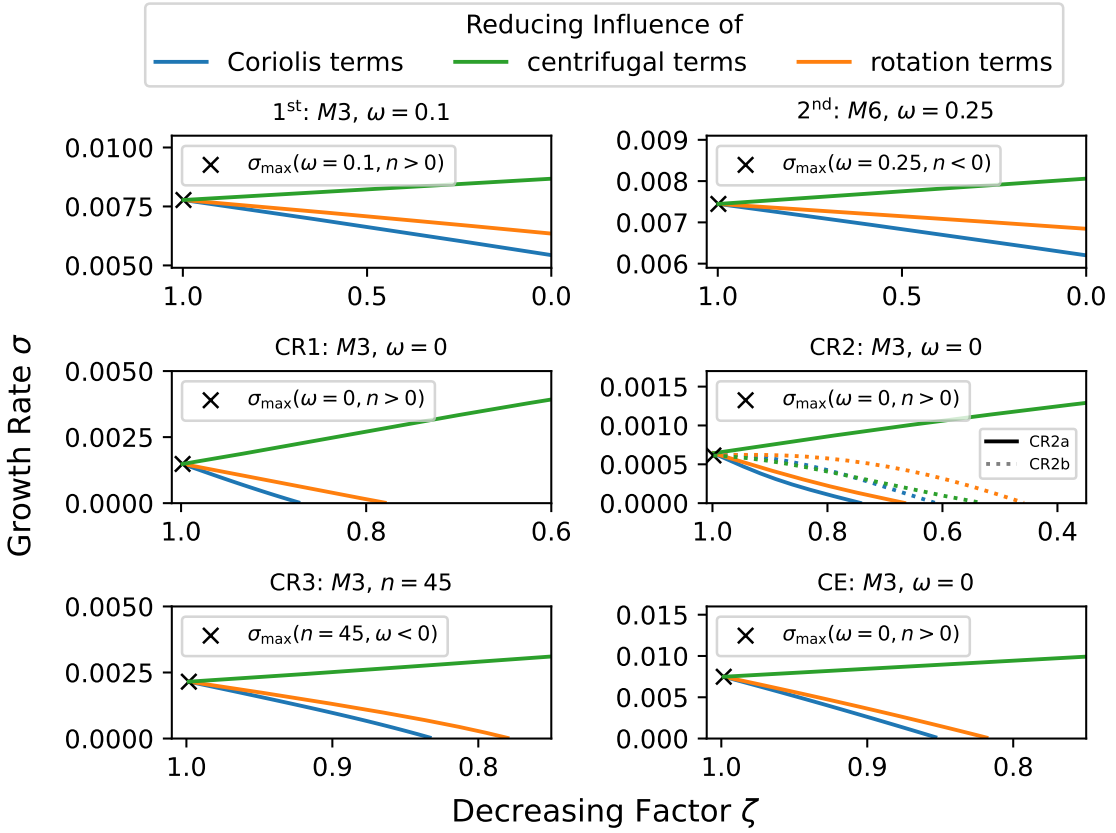

Figure 5.27.: Analysis of the effects of Coriolis, centrifugal and both the rotation terms on the modes investigated in this work. The influence of the terms on the stability equation is reduced as described in section 2.4.2.

CR3-Mode also fit the description of the modes behaving similarly in the parameter space.

This analysis could be extended to a larger variety of parameters to confirm the observed trends, but this would also exceed this work's scope. Nevertheless, it can generally be concluded that the Coriolis terms destabilise every mode considered in this work. The Coriolis terms are also the dominant destabilising mechanism for every mode except for the CR2b-Mode.

5.5. Results of the Stability Analysis and the Parameter Study

This section gives a detailed summary of the results in this chapter. For each statement, the reference to the corresponding figure is given.

1st-Mode

This work confirms the symmetrical character of the unstable parameter domain 1st-Mode in the frequency-wavefront-count domain for the non-rotating cone (cf. Figure 5.2), as reported in several studies [2, 5, 39]. With rotation, the symmetry breaks and the unstable parameter domain in the ω-n-space shifts towards positive circumferential wavenumbers (cf. Figures 5.4). This symmetry-breaking is also visible in individual growth-rate curves (cf. Figure 5.5), as the mode destabilises in the positive wavefront-count domain and stabilises for negative n. The unstable domain of the 1st-Mode also extends towards negative frequencies for positive circumferential wavenumbers. This region belongs to the Crossflow-Instability. The rotation terms in the stability equations, resulting from the coordinate transformation into the rotational coordinate system of the cone, represent a destabilising mechanism for the 1st-Mode, whereas the metric terms (divided into scale factors and terms describing the divergence and curvature of wave fronts and rays, cf. section 2.2) stabilise the mode. Both effects nearly cancel out, when both term sets are included in the stability equations. In the rotation terms, the Coriolis terms are the dominant part, as the inclusion of the centrifugal terms stabilise the mode (cf. Figure 5.27). The increase of the half-opening angle has a destabilising effect on the 1st-Mode (cf. Figure 5.6) and the increase in speed of the oncoming flow destabilises the mode as expected (cf. [5, 29]). Moreover, as the half-opening angle increases, waves with higher wavefront counts destabilise due to the local radius and waves with higher frequencies stabilise (cf. Figure 5.11). Each statement holds for both the super- and hypersonic speed regime of the oncoming axial flow.

2nd-Mode

The 2nd-Mode only destabilises for the considered M6-case (cf. section 4.1.2). It is the dominant disturbance for this speed regime of the oncoming flow (cf. Figure

5.7) and its unstable domain is symmetric in the frequency-wavefront-count domain for the non-rotational case. Higher frequencies compared to the 1st-Mode are unstable and the 2nd-Mode most unstable waves are two-dimensional. These results are consistent with the reports of previous studies ([2, 5, 30]). Also in accordance with previous studies ([5, 38]) is that the 2nd-Mode is characterised by a near-wall local maximum in the amplitude function (especially for $|\hat{T}|$, cf. Figure 5.8).
With rotation, the mode destabilises and the unstable region in the ω-n-space shifts towards higher frequencies and negative wavefront counts (cf. Figure 5.9). Hence, waves travelling against the rotation direction are stronger amplified compared to the non-rotational case. Again, the metric terms stabilise the mode as well as the centrifugal terms, while the Coriolis terms destabilise the 2nd-Mode. As the effect of the Coriolis terms predominates the effect of the centrifugal terms, the rotation terms also destabilise the 2nd-Mode, but the effects of rotation and metric terms nearly balance each other out, when both sets of terms are included in the stability equations (cf. Figures 5.10(a) and 5.27). A half-opening angle increase destabilises the 2nd-Mode (cf. Figure 5.10(b)). Furthermore, the mode's unstable domain in the frequency-wavefront-count domain shifts towards higher frequencies, so the 1st- and 2nd-Mode's unstable domains disconnect (cf. Figure 5.11).

Crossflow-Instability

With rotation, four additional modes were detected to be unstable. Three of these unstable modes are referred to as Crossflow-Modes and the other as Centrifugal-Instability.

The CR1-Mode refers to the extension of the 1st-Mode to negative frequencies when the cone rotates. This behaviour has been reported in previous studies for the cone [39] and for the flat plate [28]. A new argument is added to the discussion that this mode should be referred to as a Crossflow-Mode, as the amplitude functions change with the frequency decrease, thus revealing a separating characteristic between the 1st- and the CR1-Mode (cf. Figure 5.12). Without rotation and metric terms in the stability equations, the mode's unstable domain in the frequency-wavefront-count space is similar to the results of Song & Dong [39], but perfect agreement is not achieved, most likely due to the differences in the basic flow (cf. Figures 5.15 and 4.9). With increasing rotation intensity, the CR1-Mode destabilises and the most unstable region shifts towards more negative frequencies and higher circumferential

wavenumbers (cf. Figure 5.16). The inclusion of rotation terms destabilise and the inclusion of metric terms stabilise the CR1-Mode. When both term sets are included, the effects partly balance out, as the growth-rate curves for computations with both terms sets are generally lower than for computations without. Further, the growth-rate curves are no longer parabolic-like, as a plateau/local maximum forms for lower wavefront counts (cf. Figure 5.16). As for the 1st- and 2nd-Mode, the Coriolis terms destabilise and the centrifugal terms stabilise the CR1-Mode. Half-opening angle increase and speed increase of the oncoming flow from $M_\infty = 3.214$ to $M_\infty = 6.1$ both destabilise the CR1-Mode further (cf. Figure 5.17). Each statement applies for the M3- and M6-cases respectively.

With the inclusion of rotation and metric terms, the CR2-Mode becomes unstable and is studied in this work because the amplitude functions are physically valid (cf. Figure 5.13). This mode is divided into the CR2a-Mode for low wavefront counts and the CR2b-Mode for high wavefront counts (cf. Figure 5.18). For low rotation rates, the CR2a-Mode is dominant, which changes with increase of $\bar{\Omega}$ (cf. Figure 5.19(a)). However, the location of the most unstable domain in the frequency-wavefront-count domain remains constant at $\omega = 0$. Furthermore, the upper neutral wavefront count decreases with increasing rotation intensity and as the half-opening angle increases, both the CR2a- and the CR2b-Mode's maximum growth rates decrease and the upper neutral wavefront count increases (cf. Figure 5.19(a)). In the M6-case, the CR2-Mode is detectable, but not separable from the CR1-Mode using NOLOT to solve the stability equations. This is a general problem when studying the CR2-Mode, as the mode shares a common unstable frequency-wavefront-count domain with the CR1-Mode and both modes growth-rate curves intersect at low wavenumbers (cf. Figure 5.25). For both the CR2a- and the CR2b-Modes, the Coriolis terms have a destabilising effect. However, the influence of the centrifugal terms is different, being stabilising for the CR2a-Mode and destabilising for the CR2b-Mode.

With the inclusion of rotation and metric terms, the CR3-Mode becomes unstable and extends the unstable domain in the frequency-wavefront-count domain. Unfortunately, the problem of too small increments in the NOLOT-computations limited the study of the CR3-Mode to single growth rate curves (cf. sections 5.2.3 and 5.2.4). The study shows, that the CR3-Mode destabilises as the rotation rate, the half-opening angle and the speed of the oncoming flow increases (cf. Figure 5.20 and

5.21). The Coriolis terms denote a destabilising mechanism, whereas the centrifugal terms act stabilising (cf. Figure 5.27). Each statement applies to both the M3- and the M6-case.

Centrifugal-Instability

With the onset of rotation and the inclusion of metric and rotation terms in the stability equations, the Centrifugal-Instability (CE-Mode) becomes unstable. With increase of rotation, the CE-Mode's unstable domain in the frequency-wavefront-count space shifts towards higher - and at higher rotation rates positive - frequencies, contrary to the other investigated modes (cf. Figure 5.22). The CE-Mode is generally more unstable than the CR-Modes (cf. Figure 5.25(b)) and further destabilises with increasing rotation rate and increasing speed of the oncoming flow (cf. Figure 5.23). However, the half-opening angle increase stabilises the mode. The critical rotation rate, at which the stationary CE-Mode was found to become unstable at the cone's position $x^* = 0.4\,\mathrm{m}$, is $\bar{\Omega} = 0.5$ for the 7°-cone for both the M3- and M6-case (cf. Figure 5.24). Contrary to the name, the centrifugal terms have a stabilising effect on the CE-Mode and the Coriolis terms destabilise the mode (cf. Figure 5.27).

6. Summary and Outlook

In this work, local (parallel) linear stability analyses have been performed for the laminar boundary layers on rotating cones with supersonic ($M_\infty = 3.214$) and hypersonic ($M_\infty = 6.1$) oncoming axial flow. The half-opening angle was varied as well as the rotation rate and the influence of the rotation and metric terms in the stability equation was investigated for four different instability types, namely the 1^{st}-Mode, the 2^{nd}-Mode, the Crossflow-Instability and the Centrifugal-Instability. This chapter summarises the results presented in chapters 3 and 5 for the code validation and the stability analysis. Further, an outlook is given, on what future studies could focus on.

6.1. Results of the Code Validation

The NOLOT-extension code for rotational coordinate systems presented in the work of Dechamps & Hein [8] was validated using the self-similarity approach to describe the boundary layer of a rotating cone in incompressible, isothermal and still fluid. Comparisons to the work of Dechamps & Hein [8] for the stationary Crossflow-Instability in the boundary layer of the 90°-cone/disk showed that scale factors have falsely been included in the Coriolis and centrifugal terms of the NOLOT-extension. However, this does not affect the results of Dechamps & Hein [8] due to their choice for the reference length in the NOLOT-input file. The NOLOT-extension code was corrected and validated for different half-opening angles. Good agreement is reached with the work of Segalini & Camarri [36] for the 60°-cone (cf. 3.3) and the trend for the neutral local Reynolds numbers of the stationary Crossflow-Instability with decreasing half-opening angle is similar to the work of Fildes et al. [12]. The results also show that compressibility stabilises the stationary Crossflow-Instability as well as the exclusion of streamwise derivatives and the wall-normal velocity component in the basic flow (corresponds to parallel stability analysis).

6.2. Results of the Stability Analysis

The investigation of the non-rotational setup is in accordance with the results of previous works. Both, the unstable parameter domains of the 1st- and the 2nd-Modes are symmetric in the frequency-wavefront-count space. The maximum growth rate of the 1st-Mode is given for non-zero wavefront counts and the mode stabilises with the switch from super- to hypersonic oncoming flow velocity. The 2nd-Mode is generally more unstable than the 1st-Mode and is most unstable for $n = 0$.

The rotation of the cone has a general destabilising effect on the 1st- and 2nd-Mode, as the maximal growth rate increases with the increase of the rotation intensity. The 1st-Mode destabilises for waves travelling with and stabilises for waves travelling against the cone's rotation, which is in accordance with the results of Song & Dong [39]. Contrary, the 2nd-Mode stabilises for waves travelling with and destabilises for waves travelling against the cone's rotation. As the unstable domain of the 2nd-Mode shifts towards negative wavefront counts, the mode also shifts towards positive frequencies. To the best of the author's knowledge, both results for the 2nd-Mode have not been considered and reported in previous works.
The rotation of the cone also causes a cross-flow velocity component in the basic flow, which leads to the destabilisation of the Crossflow-Instability (CR1-Mode) and therefore to the destabilisation of waves with negative frequencies. The CR1-Mode further destabilises with increasing rotation intensity, as the maximum growth rate increases and the range of unstable wavefront counts and frequencies increases. With inclusion of rotation terms in the stability equation, the Centrifugal-Instability (CE-Mode) destabilises and with the inclusion of both the metric and rotation terms, two additional modes have been found to destabilise, namely the CR2- and the CR3-Modes. The CE-Mode and both the CR2- and the CR3-Modes also destabilise further with the increase of rotation intensity. Moreover, the unstable domain of the CE-Mode shifts towards positive frequencies and lower wavefront counts. The CR2- and the CR3-Mode are interpreted as Crossflow-Modes, although it is questioned, if they represent physical instabilities (see section 6.3), and destabilise with increase of the rotation intensity.

With the increase of the oncoming flow velocity from $M_\infty = 3.214$ to $M_\infty = 6.1$ each considered mode also destabilises further, except for the 1st-Mode. The 1st-Mode stabilises instead, similar to the non-rotational case. The destabilisation with the oncoming flow velocity of the other modes shows in the broader spectrum of unstable

frequencies and wavefront counts as well as the increased maximum growth rate. The same holds for the modes, that destabilise with the increase of the half-opening angle, namely the 1st-, 2nd-, CR1 and CR3-Modes. Contrary, the Centrifugal-Instability and the CR2-Mode stabilise with the increase of the half-opening angle.

Rotation terms were found to destabilise every considered mode. The effect dominates for the modes that only destabilise with the rotation of the cone. Contrary, the metric terms stabilise every considered mode. For the 1st- and the 2nd-Mode, both effects nearly balance each other out, so the corresponding growth rates of calculations with and without the metric and rotation terms included in the stability equations are similar. The stabilising effect of the metric terms on the CR1-Mode is slightly stronger than the destabilising effect of the rotation terms. For the other considered mode, the rotation terms affect the modes more compared to the metric terms.
Also, the individual effect of the Coriolis and the centrifugal terms were considered. The Coriolis terms are the destabilising mechanism for every considered mode, whereas the centrifugal mode stabilises every mode except for the CR2b-Mode.

6.3. Outlook

Investigation of Additional Parameters

Many parameters are held constant in this study, which could be of interest in future work.
For example, more half-opening angles could be considered to examine, whether the trends observed with increasing ψ transfer to even broader cones.
Furthermore, the free-stream speed could be increased, as this work only considers the 1st- and 2nd-Mode. For example, Chen [5] investigated the non-rotating cone with an oncoming flow of $M_\infty = 15$, in which the 3rd-Mode also destabilises. Hence, it would be interesting to investigate, if the 3rd-Mode behaves differently compared to the modes considered in this work. Additionally, more rotation rates could be considered. Especially for lower rotation rates, it would be interesting to investigate the destabilisation process of the Crossflow- and Centrifugal-Mode in the parameter space.
The temperature could also be varied, as the free-stream temperature and the wall temperature are set constant at $T_\infty = 48.28\,\mathrm{K}$ and $T_W = 300\,\mathrm{K}$ to represent ex-

perimental conditions. However, the 2nd-Mode highly depends on the near-wall temperature distribution, which motivates to introduce small changes in the wall's temperature or to consider a non-isothermal wall to examine the 2nd-Mode's instability characteristics in parameter space. Further, a variation of the wall temperature would investigate how the cooling or heating effects of the wall on the boundary layer influence the instabilities of interest, as this work only considered a heating wall in the supersonic and a cooling wall in the hypersonic setup.
Moreover, different nose radii could be considered. As this work and the results in Song & Dong [39] already provide a comparison between $r_n = 0.1\,\text{mm}$ and $r_n = 0.01\,\text{mm}$, additional nose radii could provide a more detailed overview about the effects of the nose. In particular, the difference between sharp and broad cones could be of interest.
Finally, other positions on the cone could be studied in more detail. The positions at which the instabilities destabilise could be examined (cf. critical rotation rate for CE-Mode in section 5.3.2), as well as the resulting influence of the instabilities on the final transition. The e^N-method could be applied (cf. section 2.4.1) to investigate the accumulated growth of the respective disturbances along the cone.

Additional Analysis of the Considered Setups

In general, the study already provided in chapter 5 could go into much more detail. The energy balance of each disturbance could be of interest in future work. Therefore, the disturbance's total energy is decomposed into its production, dissipation and flux terms, which give rise to the driving mechanism of the instability [43]. The work of Song & Dong [39] already includes such an investigation for the Centrifugal-Instability. This approach could be applied for every instability considered in this work. This would provide not only a deeper understanding of the disturbances' growth mechanism but also shed light on the effects of varying the half-opening angle and the velocity of the oncoming flow. The energy-balance analysis would also discuss the physical validation of the CR2- and the CR3-Modes.

As mentioned above, different modes were not separable in the parameter space. This holds for the 1st- and CR1-Modes, the CR1- and CR2-Modes (for higher rotation rates and low wavefront counts) and the CR2- and CR3-Modes. Although, this study provides a method to visualise the mode switch using amplitude functions to characterise the modes, only certain parameters could be considered. Hence, the

processes for each mode switch could be considered for the entire parameter space. However, a so-called eigenvalue solver, which is introduced in the next section, would vastly improve the accuracy and computation time of this investigation.

The newly discovered modes are of particular interest for future work. Note that this does not only include the CR2- and CR3-Modes, but also refers to the increase of the growth rate for negative wavefront counts in Figure 5.5, where the 1^{st}-Mode is inter alia investigated for the exclusion of metric and centrifugal terms. However, the following discussion focuses on the CR2- and CR3-Mode only.
Although this work provides an overview of the CR2- and CR3-Mode's characteristics and how they behave for the different influencing factors (see Figure 5.1), it is not understood, where these modes originate from and whether they describe physical instabilities; especially since both modes are only unstable with the inclusion of rotation and metric terms in the stability equations. Note that the Centrifugal-Instability is also unstable only with inclusion of the rotation terms, however the investigation of the CE-Mode did not cause any trouble compared to the CR2- and CR3-Mode. Examining both newly found modes led to the increment problem. For example, the β-increment to track the modes' behaviour with the wavefront count had to be chosen so small, that the computational cost was too high to compute the neutral wavefront count of the stationary CR2-Mode for higher rotation rates.
In order to fully understand the origins of the CR2- and the CR3-Modes and to evaluate whether the modes describe physical instabilities, the usage of an eigenvalue solver as presented in the work of Theiß [43] would be beneficial. The stability equations (cf. Equation 2.16) can be transformed into an eigenvalue problem and solving this eigenvalue problem would provide the full eigenvalue spectrum [43]. Thus, it could be tested whether or not the CR2- and the CR3-Mode are part of the eigenvalue spectrum. If they are not, the next step would be to investigate, why the computation with the NOLOT-extension code produces these modes.

A. Navier-Stokes Equations (Ch. 2) - Additional Derivation

The dimensional Navier-Stokes equations to describe compressible Newtonian fluids in Cartesian coordinate systems are given by [9]

$$0 = \partial_t^* \rho^* + \partial_{X^i}^* \left(\rho^* U_i^*\right) , \tag{A.1.1}$$

$$\rho^* \mathrm{D}_t^* U_i^* = -\partial_{X_i}^* p^* + \partial_{X^j}^* \tau_{ij}^* , \tag{A.1.2}$$

$$\rho^* \mathrm{D}_t^* h_{st}^* = \partial_t^* p^* + \partial_{X^j}^* \left(U^{*i} \tau_{ij}^*\right) - \partial_{X^i}^* \dot{q}_i , \tag{A.1.3}$$

$$p^* = R_M^* \rho^* T^* . \tag{A.1.4}$$

For the description of the notation, see chapter 2. The unknown quantities in Equations A.1.1-A.1.4 are

$$\begin{aligned}
\text{the material derivative } & D_t^* \xi^* = \partial_t^* \xi^* + U^{*j} \partial_{X_j}^* \xi^* , \\
\text{the viscous stress tensor } & \tau_{ij}^* = \lambda^* \partial_{X^k}^* U_k^* \delta_{ij} + \mu^* \left(\partial_{X^j}^* U_i^* + \partial_{X^i}^* U_j^*\right) , \\
\text{the specific total enthalpy } & h_{st}^* = e^* + \left(\mathbf{U}^*\right)^2 /2 + p^*/\rho^* , \\
\text{the specific internal energy } & e^* = T^* c_V^* \\
\text{and the heat flux } & \dot{q}_i^* = -\kappa^* \partial_{X_i}^* T^* .
\end{aligned}$$

As the energy equation in Equation 2.2.3 is given in terms of the temperature, this section presents the calculation from Equation A.1.3 to the dimensional form of Equation 2.2.3 in the Cartesian coordinate system. This also gives insight into the co- and contravariant notation.
The total energy can be re-expressed in terms of the temperature, such that the specific total enthalpy takes the form

$$h_{st}^* = e^* + \left(\mathbf{U}^*\right)^2 /2 + p^*/\rho^* = \left(c_V^* + R_M^*\right) T^* + \left(\mathbf{U}^*\right)^2 /2 = c_p^* T^* + \left(\mathbf{U}^*\right)^2 /2 .$$

Further, the kinetic energy must be re-written, as it can be expressed as a product of the velocity and the velocity's material derivative. Inserting the right hand side of the momentum equation gives

$$(U^*)^2/2 = \mathbf{U}^* \frac{\mathrm{D}\mathbf{U}^*}{\mathrm{D}t^*} \equiv U^{*i}\left(\partial_t^* U_i^* + U^{*j}\partial_{X_j}^* U_i^*\right) \overset{\text{Mom.Eq.}}{=} \rho^{-1} U^{*i}\left(-\partial_{X_i}^* p^* + \partial_{X^j}^* \tau_{ij}\right) .$$

Note that the co-/contravariant notation is introduced. If the re-written specific total enthalpy is introduced into Equation A.1.3, the energy equation is given by

$$\begin{aligned} & \rho^* c_p^* \mathrm{D}_t^* T^* + U^{*i}\partial_{X_i}^* p^* + U^{*i}\partial_{X^j}^* \tau_{ij}^* = \partial_t^* p^* + \partial_{X^j}^*\left(U^{*i}\tau_{ij}^* - \dot{q}_j^*\right) \\ \Leftrightarrow \quad & \rho^* c_p^* \mathrm{D}_t^* T^* - \mathrm{D}_t^* p^* = -\partial_{X^i}^* \dot{q}_i^* + \partial_{X^j}^*\left(U^{*i}\tau_{ij}^*\right) - U^{*i}\partial_{X^j}^* \tau_{ij}^* \\ \Leftrightarrow \quad & \rho^* c_p^* \mathrm{D}_t^* T^* - \mathrm{D}_t^* p^* = \partial_{X^i}^*\left(\kappa^* \partial_{X_i}^* T^*\right) + \left(\partial_{X^j}^* U^{*i}\right)\tau_{ij}^* , \end{aligned}$$

which represents the dimensional form of Equation 2.2.3 in Cartesian coordinate systems.

Note that any fluid- and thermodynamical quantity is non-dimensionalised with a respective reference value. This leads to the non-dimensionalisation of the state equation to be given by

$$\begin{aligned} & p^* = R_M^* \rho^* T^* \Leftrightarrow p_{ref}^* p = \rho_{ref}^* T_{ref}^* R_M^* \quad \text{with} \quad p_{ref}^* = \rho_{ref}^* u_{ref}^{*2} \\ \Rightarrow \quad & \frac{u_{ref}^{*2}}{R_M^* T_{ref}^*}\frac{p}{\rho} = T \quad \Leftrightarrow \quad \gamma M^2 p = \rho T , \end{aligned}$$

which represents the non-dimensional state equation of Equation 2.2.4 with the definition of the Mach number as in Equation 2.3.

B. Self-Similarity Approach (Ch. 3) - Detailed Derivation

This derivation is based on the work of Camarri & Segalini [36]. The dimensional Navier-Stokes equations to describe the rotating cone in incompressible and isothermal fluid is given in terms of the cone's rotational curvilinear coordinate system in the work of Hussain [20]. The non-dimensionalisation is performed using

$$
\begin{aligned}
&(x^*, z^*, h_\theta^*) = l_{ref}^* \, (x, z, h_\theta) \qquad (u^*, v^*, w^*) = u_{ref}^* \, (u, v, w) \; , \\
&p^* = \rho^* u_{ref}^{*2} p \, , \quad \mathrm{Re} = \frac{l_{ref}^* u_{ref}^*}{\nu^*} \, .
\end{aligned}
$$

The resulting non-dimensional Navier-Stokes equations are given by

$$
\begin{aligned}
&\frac{\partial u}{\partial x} + \frac{u \sin(\psi)}{h_\theta} + \frac{\partial w}{\partial z} + \frac{w \cos(\psi)}{h_\theta} = 0 \, , \\
&u\frac{\partial u}{\partial x} + w\frac{\partial u}{\partial z} - \frac{v^2 \sin(\psi)}{h_\theta} - \frac{l_{ref}^*}{u_{ref}^*} 2\Omega^* v \sin(\psi) - \frac{l_{ref}^{*2}}{u_{ref}^{*2}} \Omega^{*2} h_\theta \sin(\psi) \\
&\qquad = -\frac{\partial p}{\partial x} + \frac{1}{\mathrm{Re}} \left(\Delta^2 u - \frac{(u \sin(\psi) + w \cos(\psi)) \sin(\psi)}{h_\theta^2} \right) \, , \\
&u\frac{\partial v}{\partial x} + w\frac{\partial v}{\partial z} + \frac{(u \sin(\psi) + w \cos(\psi)) \, v}{h_\theta} - \frac{l_{ref}^*}{u_{ref}^*} 2\Omega^* (u \sin(\psi) + w \cos(\psi)) \\
&\qquad = \frac{1}{\mathrm{Re}} \left(\Delta^2 v - \frac{v}{h_\theta^2} \right) \, , \\
&u\frac{\partial w}{\partial x} + w\frac{\partial w}{\partial z} - \frac{v^2 \cos(\psi)}{h_\theta} - \frac{l_{ref}^*}{u_{ref}^*} 2\Omega^* v \cos(\psi) - \frac{l_{ref}^{*2}}{u_{ref}^{*2}} \Omega^{*2} h_\theta \cos(\psi) \\
&\qquad = -\frac{\partial p}{\partial z} + \frac{1}{\mathrm{Re}} \left(\Delta^2 w - \frac{(u \sin(\psi) + w \cos(\psi)) \cos(\psi)}{h_\theta^2} \right) \, , \\
&\text{with} \quad \Delta^2 = \frac{\partial^2}{\partial x^2} + \frac{\partial^2}{\partial z^2} + \frac{\sin(\psi)}{h_\theta} \frac{\partial}{\partial x} + \frac{\cos(\psi)}{h_\theta} \frac{\partial}{\partial z} \, .
\end{aligned}
\tag{B.1}
$$

For the description of the notation, see section 2.1. In order to derive the boundary-layer equations in first order, streamwise and wall-normal length scales are introduced as

$$\delta^{*2} = \nu^* / \left(\Omega^* \sin\left(\psi\right)\right)^{-1} , \quad L^* = x_s^* \quad \text{and} \quad \epsilon = \delta^* / L^* .$$

In the boundary-layer equation, δ^* non-dimensionalises the wall-normal coordinate z^* and L^* the streamwise coordinate x^*. For the specific choice of the reference length l_{ref}^*, this work distinguishes between two versions (V1 and V2):

$$\begin{aligned}
\text{V1}: \quad & l_{ref}^* = \delta^* : \quad x = \frac{1}{\epsilon} x_L , \quad z = z_\delta , \\
& h_\theta = \frac{x_L}{\epsilon} \sin\left(\psi\right) + z_\delta \cos\left(\psi\right) , \quad h_\theta^{-1} \approx \epsilon \frac{1}{x_L \sin\left(\psi\right)} , \\
\text{V2}: \quad & l_{ref}^* = L^* = x_s^* : \quad x = x_L , \quad z = \epsilon z_\delta , \\
& h_\theta = x_L \sin\left(\psi\right) + \epsilon z_\delta \cos\left(\psi\right) , \quad h_\theta^{-1} \approx \frac{1}{x_L \sin\left(\psi\right)} .
\end{aligned}$$

Here, the lowest order of h_θ^{-1} is already presented. Note that for higher orders, additional terms are included in the approximation of the scale factor. The self-similarity approach for the velocity components and the pressure is given by

$$(u, v) = x_L (U_0, V_0) , \; w = \epsilon W_0 , \; p = \epsilon \cot\left(\psi\right) .$$

Note that this ansatz also considers the simplification for still fluid. Finally, the reference velocity must be specified and takes the value of the wall's speed at the position x_s^*

$$u_{ref}^* = x_s^* \sin\left(\psi\right) \Omega^* .$$

Thus, the Reynolds number takes the form $\mathrm{Re} = \epsilon^{-1}$ in Version 1 and $\mathrm{Re} = \epsilon^{-2}$ in Version 2.

Inserting all these definitions into the dimensional Navier-Stokes equations in Equation B.1 and neglecting non-linear terms with respect to ϵ leaves the self-similarity approximation of the rotating cone's boundary layer in still, incompressible and isothermal fluid as given in Equation 3.3. Note that the second order of ϵ has been considered in the work of Segalini & Camarri [36]; however, the corrections are given in a non-rotational coordinate system.

C. Self-Similarity Approach (Ch. 3) - Additional Visualisations

This section validates that pressure derivatives in wall-normal direction can be neglected in the self-similar approximated boundary layer's basic flow of the rotating cone in still, incompressible and isothermal fluid. Therefore, Figure C.1 visualises neutral curves of the stationary Crossflow-Instability for a cone with $\psi = 70°$. Figure C.1(a) shows the neutral curves in the α_r-Re$_l$-space and Figure C.1(b) the neutral curves in the n-Re$_l$-space. The red curves represent linear stability analysis results without pressure derivatives in the basic flow, whereas the circles are results with pressure derivatives included. Perfect agreement is reached between the respective curves, which exemplary shows that pressure derivatives can be neglected.

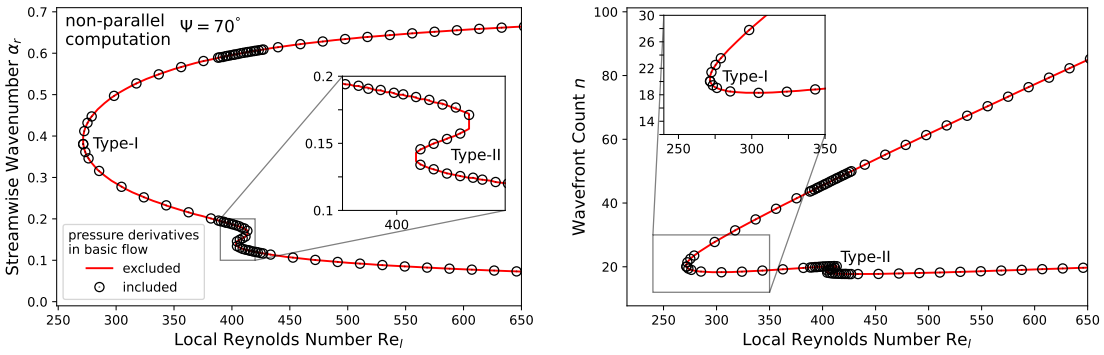

(a) (b)

Figure C.1.: Neutral curves of the stationary Crossflow-Instability for a 70°-cone in the α_r-Re$_l$-space (a) and the n-Re$_l$-space (b).

D. Rotation Rates of Rotating Cones in Super-/Hypersonic Flow (Ch. 4) - Additional Information

This section provides additional information on the simulation strategy for the basic flow of rotating cones in super- and hypersonic axial oncoming flow.

Figure D.1 validates that the reference values of the non-rotational case can also be used as reference values with the onset and increase of rotation. The relative change of the Blasius length δ and the boundary-layer edge velocity u_e with the rotational intensity increase are visualised for the 7°-M3- and M6-case, as the respective non-rotational case is used for non-dimensionalisation. The change of the velocity is less than 0.5% and the change of the Blasius length less than 4%. Hence, the non-rotational case is used to non-dimensionalise the rotational setups as well.

Tables D.1 and D.2 list the dimensional rotation rates for each setup.

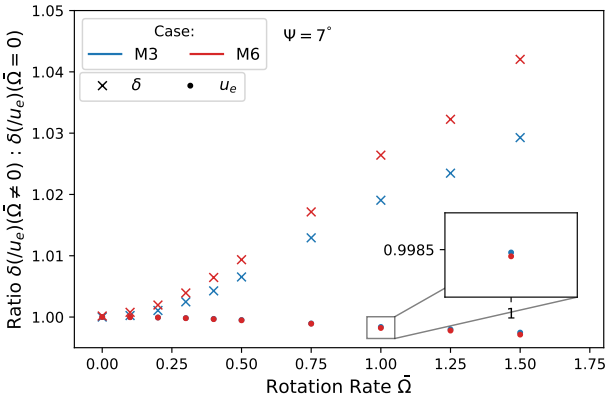

Figure D.1.: Relative change of the Blasius length δ and the boundary-layer edge velocity u_e with the rotational intensity increase for the 7°-M3- and M6-cases.

Table D.1.: Dimensional rotation rates for each considered half-opening angle of the M3-case.

	Case	M3			
	ψ	5°	7°	10°	15°
Dim. Rot. Rate $\lvert\Omega^*\rvert$ in [°/s]	$\bar{\Omega} = 0$	0	0	0	0
	0.1	72556.2	51451.6	35560.7	23114.1
	0.2	145112.5	102903.3	71121.4	46228.2
	0.3	217668.7	154354.9	106682.0	69342.4
	0.4	290225.0	205806.5	142242.7	92456.5
	0.5	362781.2	257258.1	177803.4	115570.6
	0.75	544171.8	385887.2	266705.1	173355.9
	1.0	725562.5	514516.3	355606.8	231141.2
	1.25	906953.1	643145.4	444508.4	288926.5
	1.5	1088343.7	771774.4	533410.1	346711.8

Table D.2.: Dimensional rotation rates for each considered half-opening angle of the M6-case.

	Case	M6			
	ψ	5°	7°	10°	15°
Dim. Rot. Rate $\lvert\Omega^*\rvert$ in [°/s]	$\bar{\Omega} = 0$	0	0	0	0
	0.1	138262.7	98321.6	68250.9	44667.3
	0.2	276525.5	196643.1	136501.8	89334.5
	0.3	414788.2	294964.7	204752.7	134001.8
	0.4	553051.0	393286.3	273003.7	178669.1
	0.5	691313.7	491607.8	341254.6	223336.3
	0.75	1036970.6	737411.7	511881.9	335004.5
	1.0	1382627.5	983215.6	682509.1	446672.6
	1.25	1728284.3	1229019.6	853136.4	558340.8
	1.5	2073941.2	1474823.5	1023763.7	670009.0

E. Basic Flow of Rotating Cones in Super-/Hypersonic Flow (Ch. 4) - Additional Boundary-Layer Profiles

This section presents the boundary-layer profiles (in the captions shortened as BLP) of each considered setup at the position $x^* = 0.4\,\mathrm{m}$: Both the M3- and the M6-cases are visualised for every half-opening angle $\psi = 5°, 7°, 10°, 15°$ and for every rotation rate $\bar{\Omega} = 0 - 0.9$.

The profiles are given in the following order:

	M-case	ψ	Figure
1.	3	7°	E.1
2.	6	7°	E.2
3.	3	5°	E.3
4.	6	5°	E.4
5.	3	10°	E.5
6.	6	10°	E.6
7.	3	15°	E.7
8.	6	15°	E.8

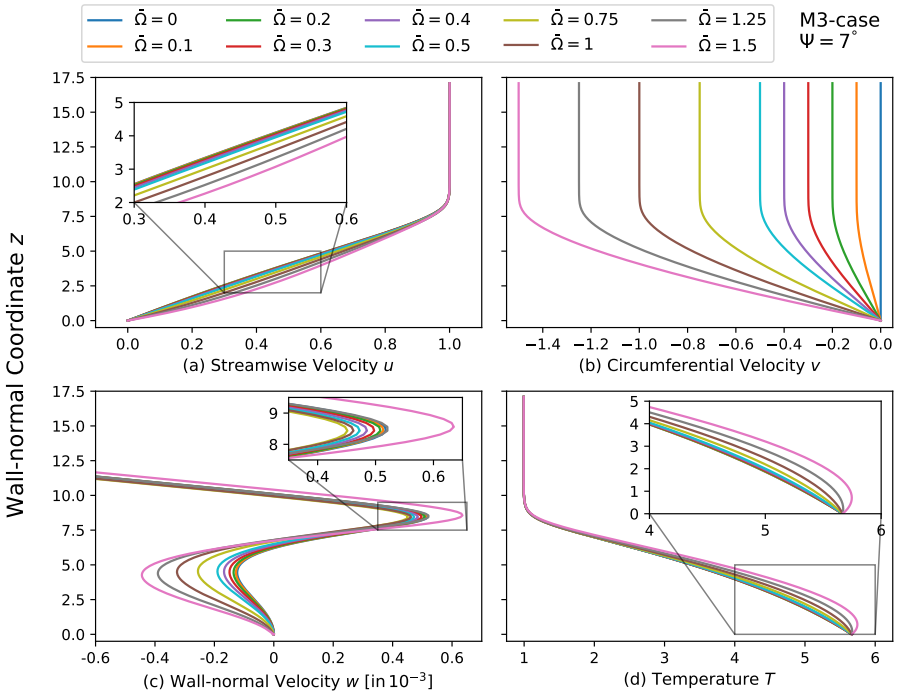

Figure E.1.: BLP u (a), v (b), w (c) and T (d) for the 7°-M3-case.

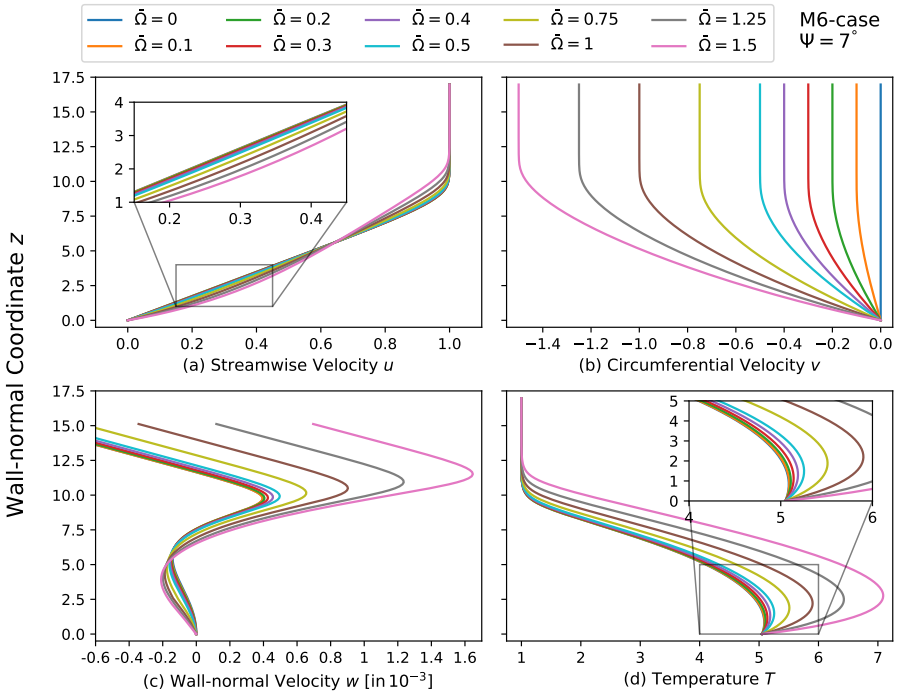

Figure E.2.: BLP u (a), v (b), w (c) and T (d) for the 7°-M6-case.

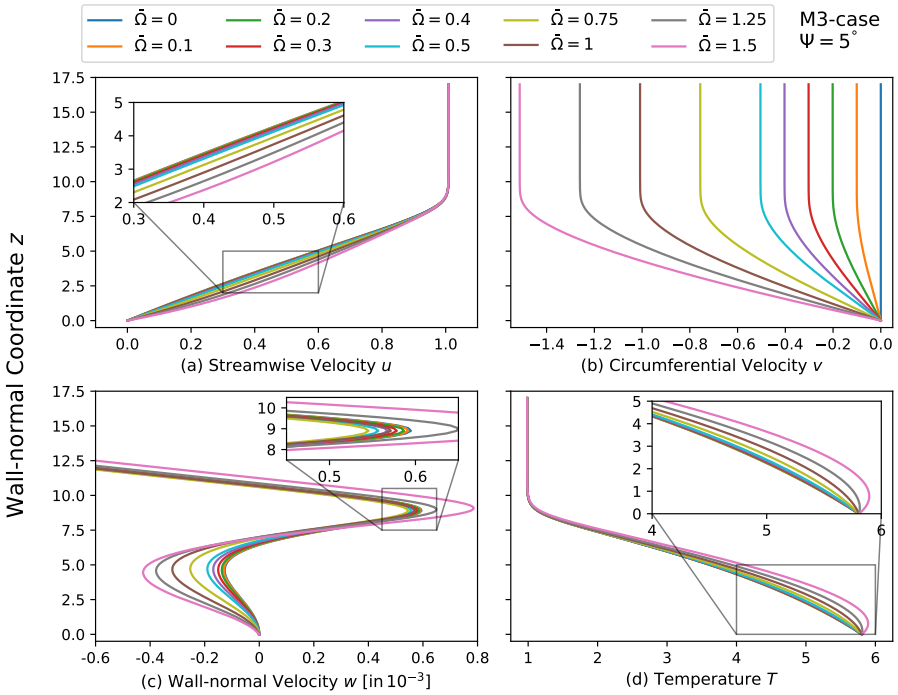

Figure E.3.: BLP u (a), v (b), w (c) and T (d) for the 5°-M3-case.

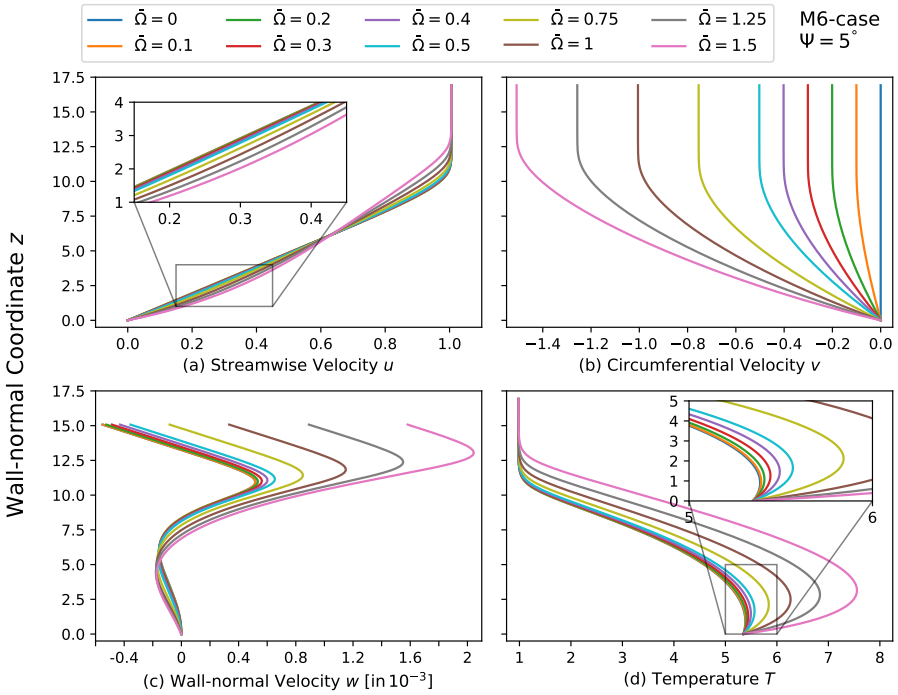

Figure E.4.: BLP u (a), v (b), w (c) and T (d) for the 5°-M6-case.

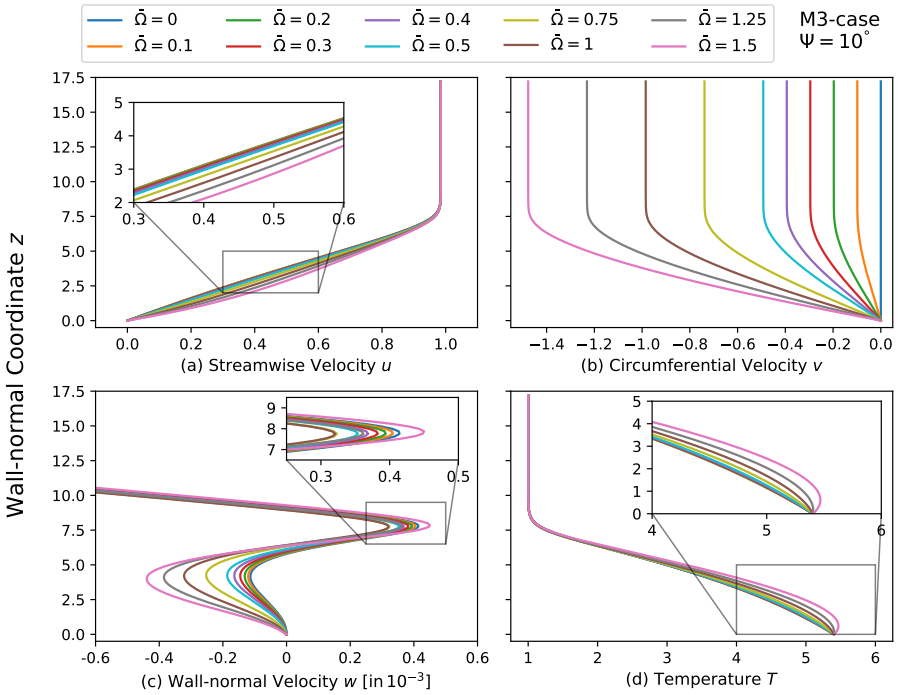

Figure E.5.: BLP u (a), v (b), w (c) and T (d) for the 10°-M3-case.

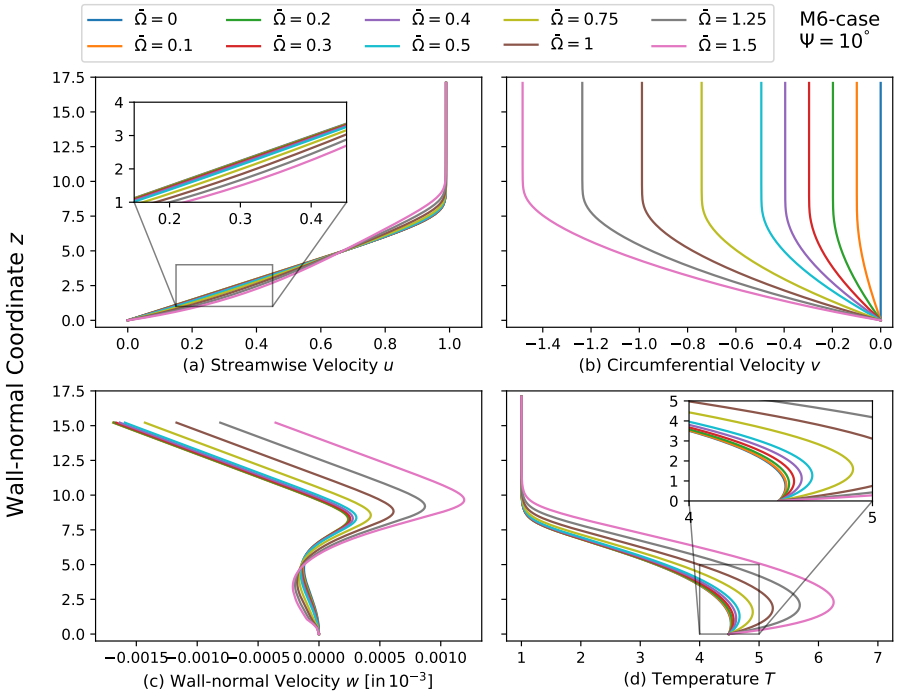

Figure E.6.: BLP u (a), v (b), w (c) and T (d) for the 10°-M6-case.

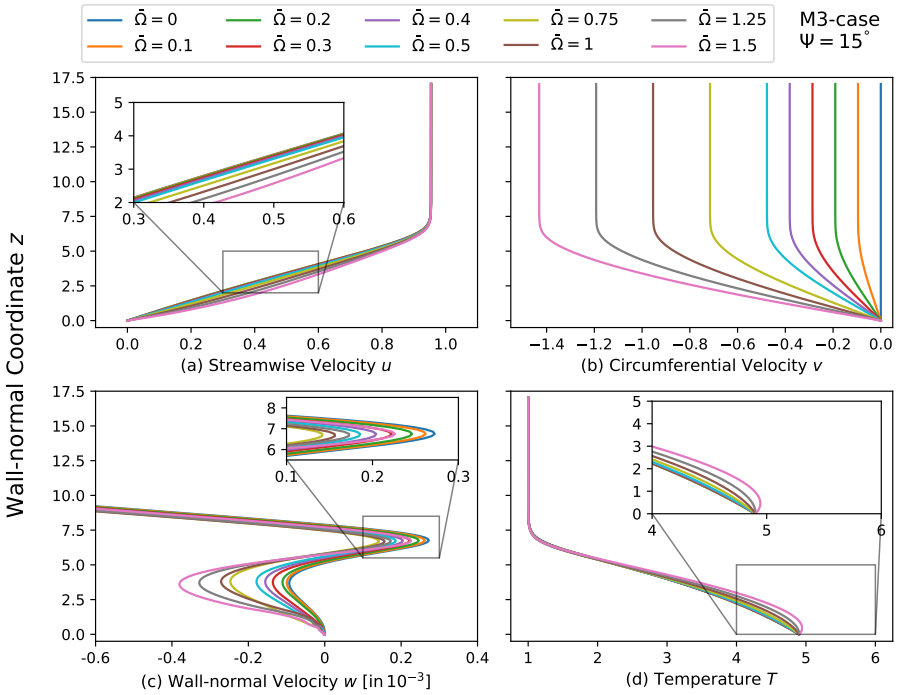

Figure E.7.: BLP u (a), v (b), w (c) and T (d) for the 15°-M3-case.

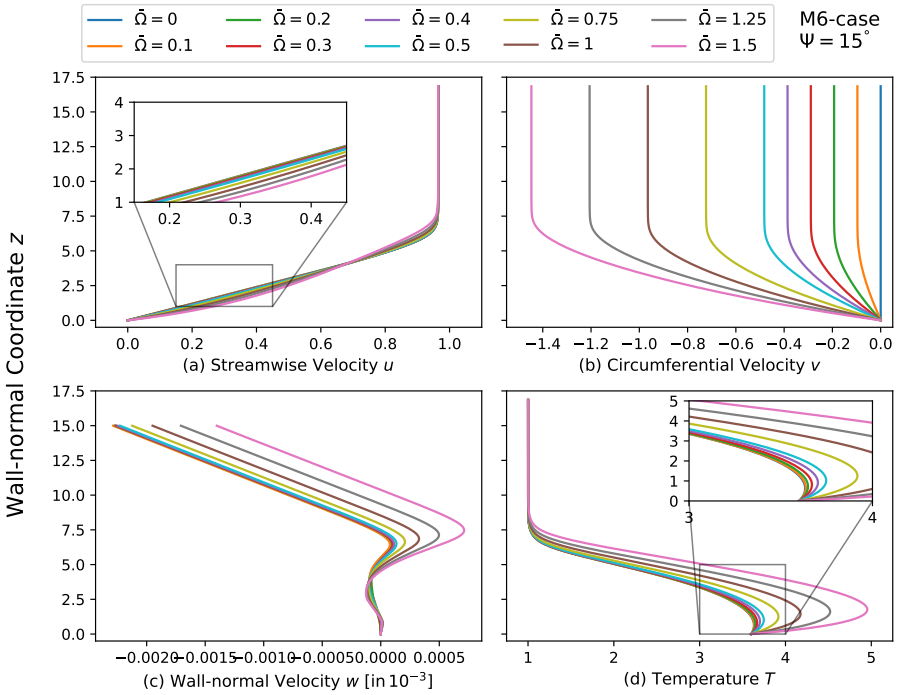

Figure E.8.: BLP u (a), v (b), w (c) and T (d) for the 15°-M6-case.

F. Stability Analysis Results (Ch. 5) - Additional Visualisations

This section presents additional visualisations for the stability analysis results presented in chapter 5.

1st-Mode

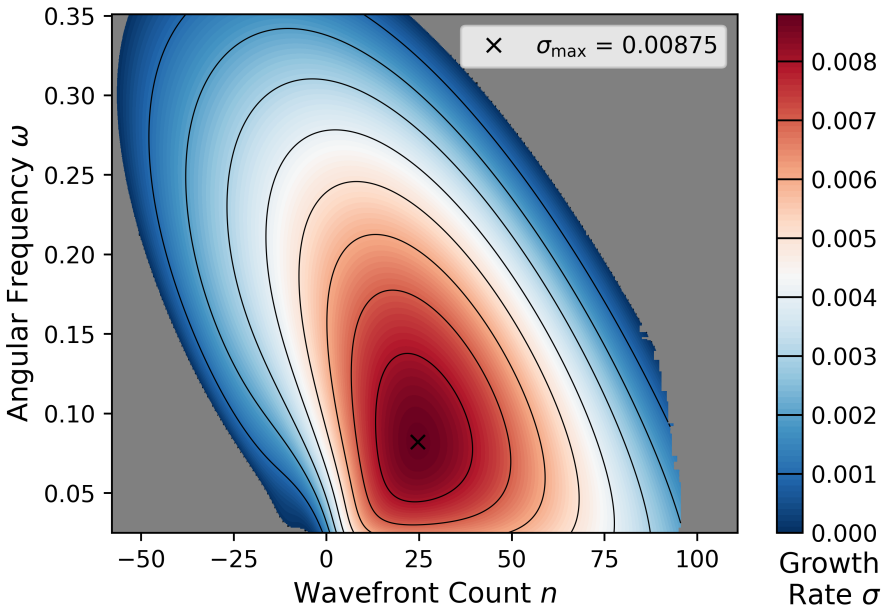

Figure F.1.: Contour lines of the growth rates σ of the 1st-Mode in the ω-n-space for the 7°-M3-case with $\bar{\Omega} = 0.75$. In the grey-coloured domain, the mode is stable ($\sigma < 0$). The neutral curve ($\sigma = 0$) is not included due to resolution problems for low frequencies.

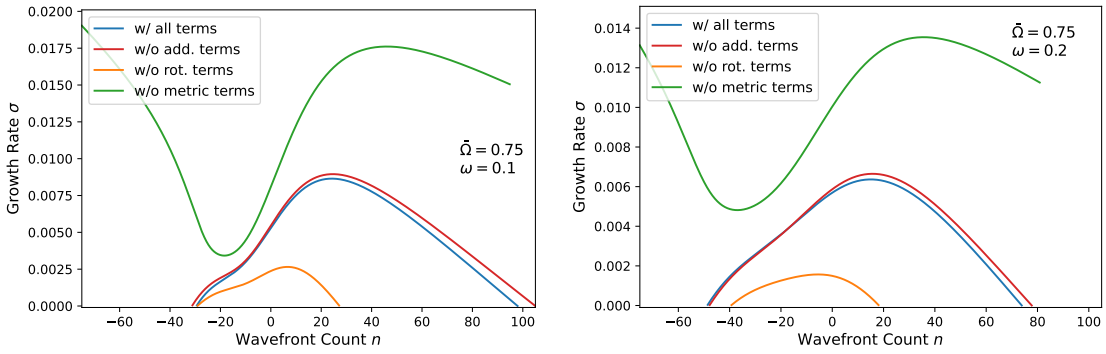

(a) (b)

Figure F.2.: Growth-rate curves plotted as a function of the wavefront count n at $\omega = 0.1$ (a) and $\omega = 0.2$ (b), varying the inclusion of metric and rotation terms in the stability equation (7°-M3-case, $\bar{\Omega} = 0.75$).

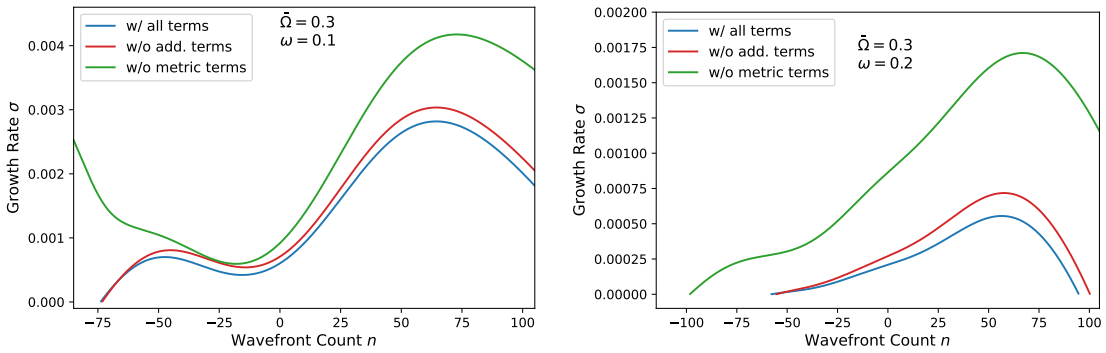

(a) (b)

Figure F.3.: Growth-rate curves plotted as a function of the wavefront count n at $\omega = 0.1$ (a) and $\omega = 0.2$ (b), varying the inclusion of metric and rotation terms in the stability equation. The 1st-Mode is stable without rotation terms in the stability equations (7°-M6-case, $\bar{\Omega} = 0.3$).

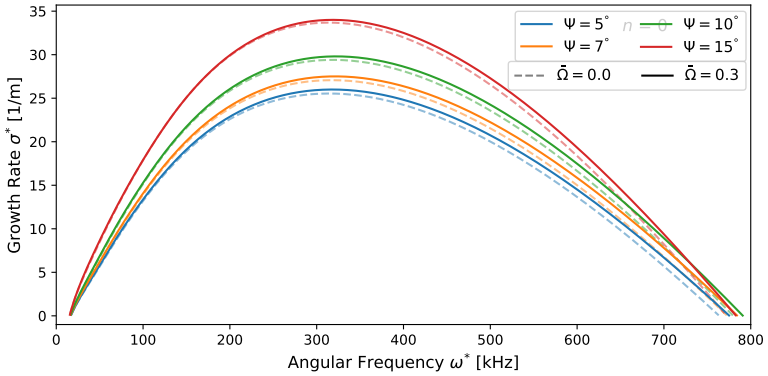

Figure F.4.: Growth-rate curves plotted as a function of the angular frequency ω^* for different half-opening angles and rotation rates (7°-M3-case, $n = 0$).

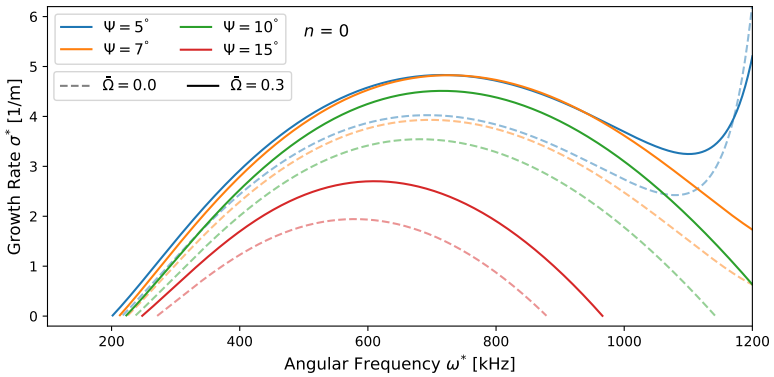

Figure F.5.: Growth-rate curves plotted as a function of the angular frequency ω^* for different half-opening angles and rotation rates (7°-M6-case, $n = 0$).

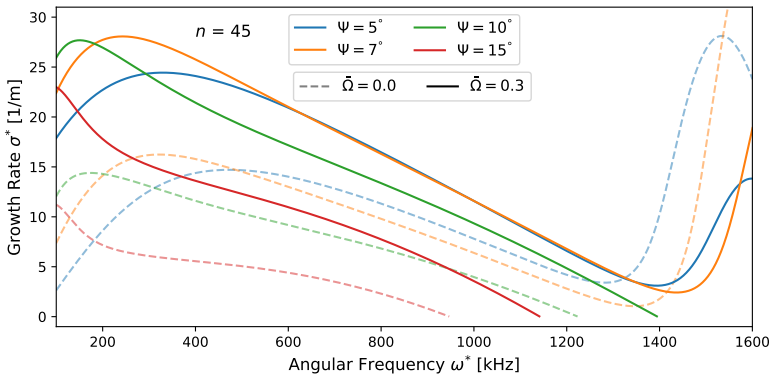

Figure F.6.: Growth-rate curves plotted as a function of the angular frequency ω^* for different half-opening angles and rotation rates (7°-M6-case, $n = 45$).

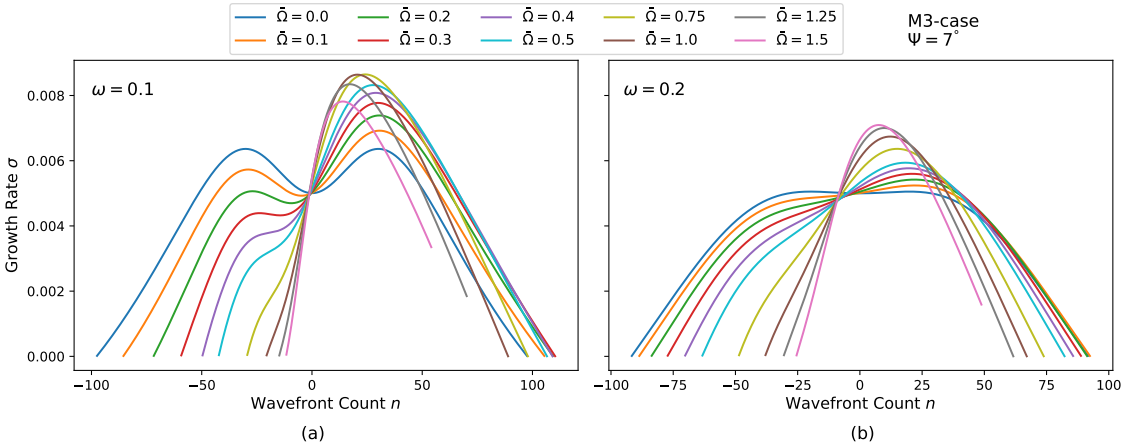

Figure F.7.: Growth-rate curves plotted as a function of the wavefront count n for different rotation rates at $\omega = 0.1$ (a) and $\omega = 0.2$ (b) (7°-M3-case, $n = 0$).

CR1-Mode

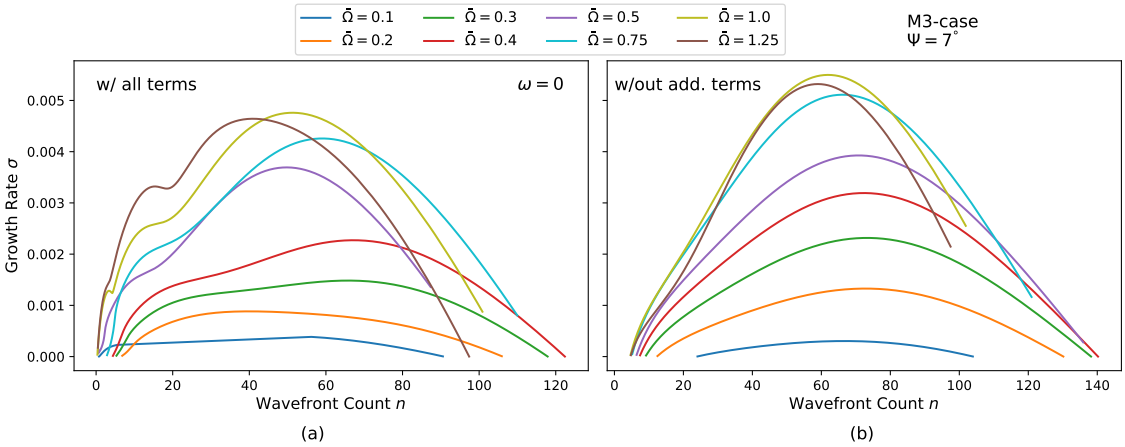

Figure F.8.: CR1-Mode's growth-rate curves plotted as a function of the wavefront count n for different rotation rates at $\omega = 0$ using default-settings in (a) and without additional terms in (b) (7°-M3-case, $n = 0$).

2nd-Mode

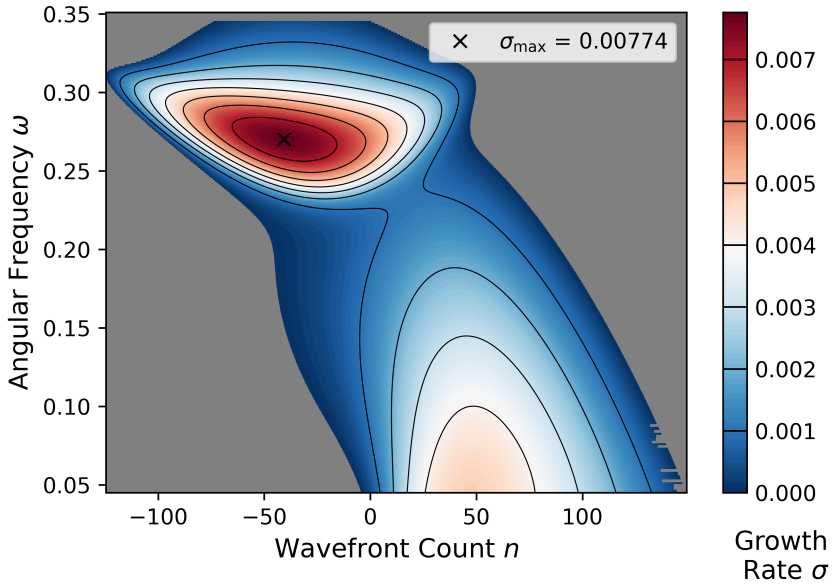

Figure F.9.: Contour lines of the growth rates σ of the 2nd-Mode in the ω-n-space for the 7°-M3-case with $\bar{\Omega} = 0.75$. In the grey-coloured domain, the mode is stable ($\sigma < 0$). The neutral curve ($\sigma = 0$) is not included due to resolution problems for low frequencies.

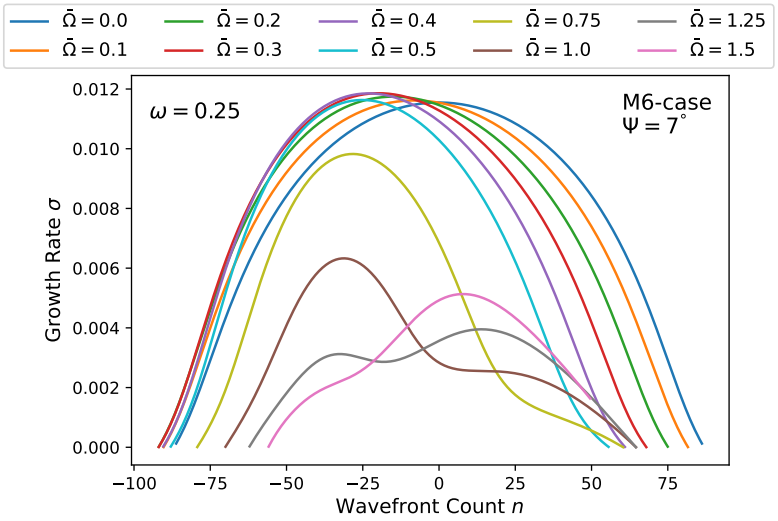

Figure F.10.: 2nd-Mode's growth-rate curves plotted as a function of the wavefront count n for different rotation rates at $\omega = 0.1$ (a) and $\omega = 0.2$ (b). The 1st-Mode's becomes dominant at this angular frequency with increasing rotation rate (7°-M3-case, $n = 0$).

Centrifugal-Instability

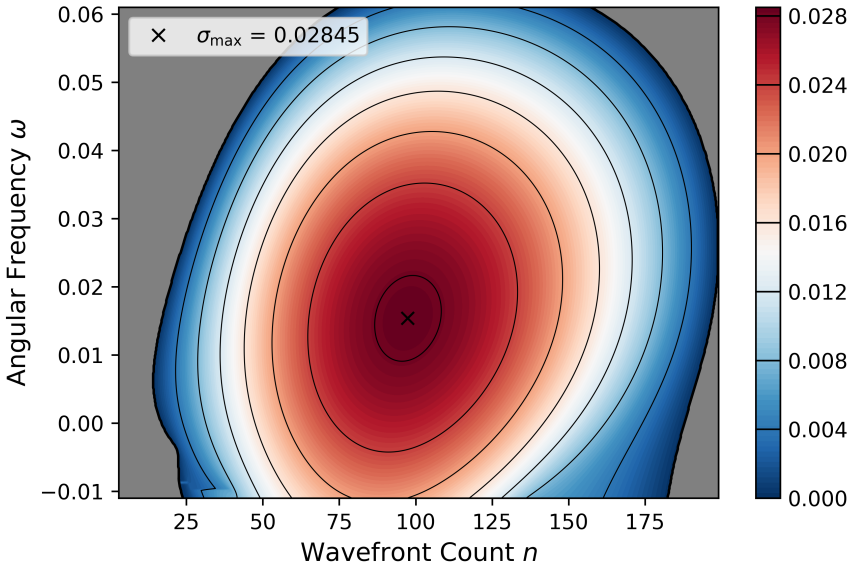

Figure F.11.: Contour lines of the growth rates σ of the CE-Mode in the ω-n-space for the 7°-M3-case at $\bar{\Omega} = 1.25$. The mode is stable in the grey-coloured domain.

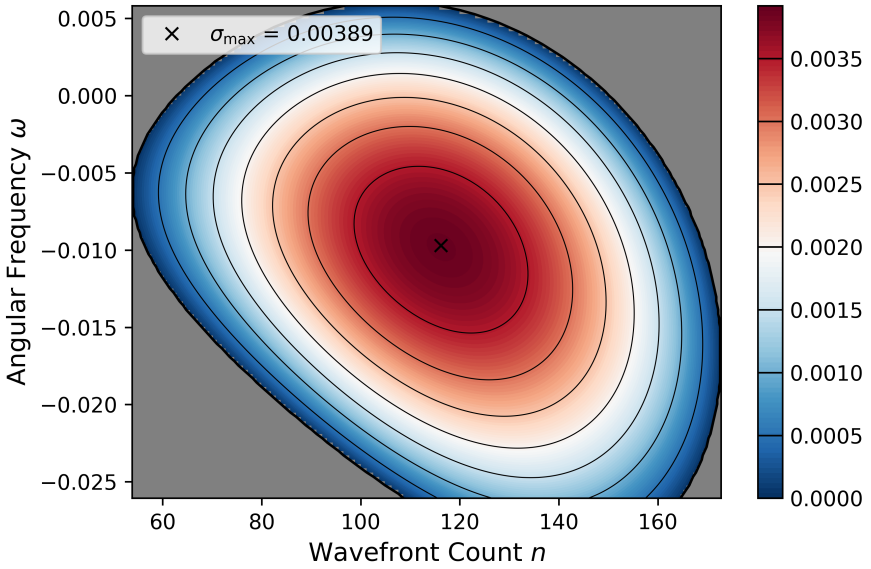

Figure F.12.: Contour lines of the growth rates σ of the CE-Mode in the ω-n-space for the 10°-M3-case at $\bar{\Omega} = 0.75$. The mode is stable in the grey-coloured domain.

Bibliography

[1] Aris, R. (1990). *Vectors, Tensors and the Basic Equations of Fluid Mechanics.* Dover Books on Mathematics. Dover Publications.

[2] P. Balakumar and H. L. Reed (1991). "Stability of three-dimensional supersonic boundary layers". In: *Physics of Fluids: Fluid Dynamics* 3.4, pp. 617–632.

[3] O. Brodersen et al. (1996). "The Parametric Grid Generation System MegaCads." In: *Proc. 5th International Conference on Numerical Grid Generation in Computational Field Simulations, 1.-5.4.1996, MS.* In Soni, B. K., Thompson, J. F., Häuser, J. and Eiseman, P. R., editors. NSF Engineering Research Center, Mississippi State University, pp. 353–362.

[4] A. Busemann (1929). "Drücke auf kegelförmige Spitzen bei Bewegung mit Überschallgeschwindigkeit". In: *ZAMM - Journal of Applied Mathematics and Mechanics/Zeitschrift für Angewandte Mathematik und Mechanik* 9.6, pp. 496–498.

[5] X. Chen, D. Xu and S. Fu (2021). "Oblique-mode breakdown in hypersonic and high-enthalpy boundary layers over a blunt cone". In: *Advances in Aerodynamics* 3, p. 24.

[6] R. Courant, K. Friedrichs and H. Lewy (1928). "Über die partiellen Differenzengleichungen der mathematischen Physik". In: *Mathematische Annalen* 100, pp. 32–74.

[7] M. A. Day (1990). "The No-Slip Condition of Fluid Dynamics". In: *Erkenntnis (1975-)* 33.3, pp. 285–296.

[8] X. Dechamps and S. Hein (2018). "Extension of the PSE Code NOLOT for Transition Analysis in Rotating Reference Frames". In: *New Results in Numerical and Experimental Fluid Mechanics XI*. Ed. by A. Dillmann et al. Cham: Springer International Publishing, pp. 179–188.

[9] J. Délery (2010). *Handbook of Compressible Aerodynamics*. Wiley.

[10] Deutsches Zentrum für Luft- und Raumfahrt e.V. (2019). *Technical Documentation of the DLR TAU-Code Release 2019.1.0*.

[11] J. H. Ferziger, M. Perić and R. L. Street (2020). *Numerische Strömungsmechanik*. 2nd. Springer Verlag Berlin, Heidelberg.

[12] M. Fildes et al. (2020). "Analysis of boundary layer flow over a broad rotating cone in still fluid with non-stationary modes". In: *Physics of Fluids* 32.12, p. 124118.

[13] C. A. J. Fletcher (2020). *Computational Techniques for Fluid Dynamics*. 2nd. Springer Berlin/Heidelberg.

[14] S. J. Garrett, Z. Hussain and S. O. Stephen (2009). "The cross-flow instability of the boundary layer on a rotating cone". In: *Journal of Fluid Mechanics* 622, pp. 209–232.

[15] S. J. Garrett, Z. Hussain and S. O. Stephen (2010). "Boundary-Layer Transition on Broad Cones rotating in an Imposed Axial Flow". In: *AIAA Journal* 48.6, pp. 1184–1194.

[16] G. Gasperas (1987). *The stability of the compressible boundary layer on a sharp cone at zero angle of attack*. 25th AIAA Aerospace Sciences Meeting. AIAA Paper 1987-0494.

[17] N. Gregory, J. T. Stuart and W. S. Walker (1955). "On the Stability of Three-Dimensional Boundary Layers with Application to the Flow Due to a Rotating Disk". In: *Philosophical Transactions of the Royal Society of London, Series A, Mathematical and Physical Sciences* 248.943, pp. 155–199.

[18] G. L. Grozdovskii (1959). "Supersonic axisymmetric conical flows with conical shocks adjacent to uniform parallel flows". In: *Journal of Applied Mathematics and Mechanics* 23.2, pp. 532–538.

[19] S. Hein et al. (1995). *Linear Nonlocal Instability Analysis - the Linear NOLOT Code*. DLR-IB 223-94 A56.

[20] Z. Hussain (2010). *Stability and transition of three-dimensional rotating boundary layers*. PhD thesis, University of Birmingham.

[21] Z. Hussain and S. J. Garrett (2021). "On the stability of boundary-layer flow over a rotating cone using new solution methods". In: *Journal of Physics: Conference Series* 1909.1, p. 012041.

[22] Z. Hussain, S. J. Garrett and S. O. Stephen (2014). "The centrifugal instability of the boundary-layer flow over slender rotating cones". In: *Journal of Fluid Mechanics* 755, pp. 274–293.

[23] Z. Hussain et al. (2016). "The centrifugal instability of the boundary-layer flow over a slender rotating cone in an enforced axial free stream". In: *Journal of Fluid Mechanics* 788, pp. 70–94.

[24] R. W. Johnson (1998). *The Handbook of Fluid Dynamics*. Electrical engineering handbook series. Springer Berlin Heidelberg.

[25] K. Kato et al. (2022). "Instabilities and Transition on a Rotating Cone - Old Problems and New Challenges". In: *IUTAM Laminar-Turbulent Transition*. Ed. by Spencer Sherwin, Peter Schmid and Xuesong Wu. Cham: Springer International Publishing, pp. 203–213.

[26] J. M. Kendall (1975). "Wind Tunnel Experiments Relating to Supersonic and Hypersonic Boundary-Layer Transition". In: *AIAA Journal* 13.3, pp. 290–299.

[27] M.-S. Liou and C. J. Steffen (1993). "A New Flux Splitting Scheme". In: *Journal of Computational Physics* 107, pp. 23–39.

[28] Z. Liu (2022). "Cross-flow linear instability in compressible boundary layers over a flat plate". In: *Physics of Fluids* 34.9, p. 094110.

[29] L. Mack (1984). "Boundary-layer linear stability theory". In: *AGARD Report* 709.3, pp. 1–3.

[30] L. Mack (1987). *Stability of axisymmetric boundary layers on sharp cones at hypersonic Mach numbers*. 19th AIAA, Fluid Dynamics, Plasma Dynamics, and Lasers Conference. AIAA Paper 1987-1413.

[31] R. Oddo et al. (2021). "Effect of surface cooling on second-mode dominated hypersonic boundary layer transition". In: *Experiments in Fluids* 62.7, 144, p. 144.

[32] M. Otto (2011). *Rechenmethoden für Studierende der Physik im ersten Jahr*. Spektrum Akademischer Verlag GmbH.

[33] C. D. Pruett et al. (1995). "Spatial direct numerical simulation of high-speed boundary-layer flows part I: Algorithmic considerations and validation". In: *Theoretical and Computational Fluid Dynamics* 7.1, pp. 49–76.

[34] H. L. Reed, W. S. Saric and D. Arnal (1996). "Linear Stability Theory Applied to Boundary Layers". In: *Annual Review of Fluid Mechanics* 28.1, pp. 389–428.

[35] H. Schlichting and K. Gersten (2017). *Boundary-Layer Theory*. 9th. Springer-Verlag Berlin Heidelberg.

[36] A. Segalini and S. Camarri (2019). "Flow induced by a rotating cone: Base flow and convective stability analysis". In: *Physical Review Fluids* 4 (8), p. 084801.

[37] P. Seltner et al. (2021). "Aerodynamics of inclined cylindrical bodies free-flying in a hypersonic flowfield". In: *Experiments in Fluids* 62.

[38] J. Sivasubramanian and H. F. Fasel (2015). "Direct numerical simulation of transition in a sharp cone boundary layer at Mach 6: fundamental breakdown". In: *Journal of Fluid Mechanics* 768, pp. 175–218.

[39] R. Song and M. Dong (2023). "Linear instability of a supersonic boundary layer over a rotating cone". In: *Journal of Fluid Mechanics* 955, A31.

[40] K. Stetson and Roger K. (1992). *On hypersonic boundary-layer stability*. 30th Aerospace Sciences Meeting and Exhibit. AIAA Paper 1992-0737.

[41] W. Sutherland (1893). "LII. The viscosity of gases and molecular force". In: *The London, Edinburgh, and Dublin Philosophical Magazine and Journal of Science* 36.223, pp. 507–531.

[42] S. S. Tambe (2022). *Boundary-layer instability on rotating cones: An experiment-based exploration*. PhD thesis, Delft University of Technology.

[43] A. Theiß (2021). *Transition Mechanisms on Blunt Re-Entry Capsules With and Without Roughness*. PhD thesis, Technische Universität Braunschweig.

[44] P. D. Towers and S. J. Garrett (2014). "Similarity solutions of compressible flow over a rotating cone with surface suction". In: *Thermal Science* 20, pp. 32–32.

[45] N. Uygun and M. Türkyilmazoğlu (2004). "Basic compressible flow over a rotating disk". In: *Hacettepe Journal of Mathematics and Statistics* 33.

[46] J. van Ingen (1956). *A suggested semi-empirical method for the calculation of the boundary layer transition region*. Institutional Repository, Delft University of Technology.

[47] Y. Wada and M.-S. Liou (1994). *A flux splitting scheme with high-resolution and robustness for discontinuities*. 32nd Aerospace Sciences Meeting and Exhibit. AIAA Paper 1994-0083.

Acknowledgements

Ich habe nun eine sehr lange Zeit an der Master-Arbeit gearbeitet; auch wenn man zugeben muss, dass der Großteil der Arbeit in den letzten Monaten entstanden ist. Trotzdem ist in dieser gesamten Zeit einiges passiert. Allein an der Anzahl der Arbeitsplätze kann man dies erkennen: Von den drei verschiedenen Büros am DLR, über Büros von KommilitonInnen, bis hin zu sämtlichen Bibliotheken und Abeitsräumen, die in der Universität existieren, und noch vielen weiteren Orten.
Es war nicht immer einfach, sich trotz einiger Rückschläge zu motivieren, aber ich bin im Nachhinein doch sehr froh, dass ich es immer wieder geschafft habe. An dieser Stelle sei auch gesagt, dass ich am Ende echt glücklich über das daraus entstandene Resultat bin.

Zu guter Letzt habe ich noch einigen Menschen zu danken.
An erster Stelle stehen da natürlich meine Eltern, die mich durch das gesamte Studium hinweg immer unterstützt haben.
Außerdem möchte ich mich bei Alex bedanken, der immer erreichbar war, um mir bei Problemen zu helfen, und, genauso wie Stefan, zu jeder Zeit ansprechbar war.
Und dann gibt es noch viele weitere Einzelpersonen, denen ich danken wollen würde. Diese kann ich aber nicht alle auflisten, da ich niemanden vergessen möchte.
Deshalb sage ich einfach: Danke an alle, die das hier gerade lesen und sich angesprochen fühlen!

Erklärung Ich versichere hiermit, dass ich die vorliegende Arbeit ohne fremde Hilfe selbstständig verfasst und nur die von mir angegebenen Quellen und Hilfsmittel verwendet habe. Wörtlich oder sinngemäß aus anderen Werken entnommene Stellen habe ich unter Angabe der Quellen kenntlich gemacht. Die Richtlinien zur Sicherung der guten wissenschaftlichen Praxis an der Universität Göttingen wurden von mir beachtet. Eine gegebenenfalls eingereichte digitale Version stimmt mit der schriftlichen Fassung überein. Mir ist bewusst, dass bei Verstoß gegen diese Grundsätze die Prüfung mit nicht bestanden bewertet wird.

Göttingen, den January 24, 2024